DETECTION AND LOCALIZATION OF DAMAGE IN FIBER REINFORCED POLYMER BARS USING ACOUSTIC EMISSION DETECTION, MICRO COMPUTED TOMOGRAPHY, AND SCANNING ELECTRON MICROSCOPY TECHNIQUES

by

MAHA GHAIB

A thesis Submitted to the Faculty of Graduate Studies of

The University of Manitoba

In partial fulfillment of the requirements for the degree of

Doctor of Philosophy

Department of Civil Engineering

University of Manitoba

Winnipeg

August 2018

ABSTRACT

Fiber reinforced polymer (FRP) rebars have been used for reinforcing concrete structures for the last quarter of the century. The advantages of using FRP are: high strength to weight ratio, corrosion resistance, durability, and high tensile strength. It would be beneficial to have non-destructive testing (NDT) methods that have the potential to detect damage at loads well below failure. This is particularly important for FRP rebars as they do not exhibit any external signs of damage until brittle failure. However, internal damage in FRP rebars increases with increasing tensile loads. Acoustic emission (AE) signal has proved to be a useful tool for monitoring damage in FRP materials. However, FRP rebars have received little attention. In this work damage progression in different types of FRP rebars subjected to tension was studied using AE, SEM and μCT. One possible mechanism for damage progression is the growth of voids entrapped in FRP rebars during their manufacture. These voids are a weakened region within the bars. When the bar is subjected to stress these regions can grow in size. In this work the growth of the voids within the bar is interpreted as the progression of damage. Internal voids and their growth were observed using micro computed tomography (μCT) and scanning electron microscopy (SEM) and compared to AE results. Strong correlation was observed between the void volume growth determined using μCT analysis and cumulative energy of AE.

This work also demonstrated improved methods used to locate the source of AE signals that occurred in FRP rebars subjected to tension. An artificial neural network (ANN) was used to reduce the uncertainty in determining the AE source location. The ANN had improved accuracy, compared to the conventional source location methods by factor of 1.6

and 3 for GFRP and CFRP samples respectively. The source location results obtained with the ANN were also compared to μCT void volume analysis along the length of the bars after tension testing.

CO-AUTHORSHIP

This thesis has been prepared in accordance with the regulation of integrated-article format stipulated by the Faculty of Graduate Studies at the University of Manitoba. Substantial parts of this thesis were submitted for publication to peer-reviewed technical journals as shown below:

1. **Ghaib, M.**, Shateri, M., Thomson, D., Svecova, D. (2018) "Study of FRP bars under tension using acoustic emission detection technique," *Journal of Civil Structural Health Monitoring,* 8(2), 285-300, DOI: 10.1007/s13349-018-0273-8, **[Chapter 4]**. I have preformed the FRP samples preparation for the tension test, cross and longitudinal sections preparation for SEM, the extraction of AE parameters in time domain, the classification of AE events using the k-means algorithm, STFT and the energy distribution, SEM observation, the first draft of the written article paper, and the responding to the reviewers' comments. RMS algorithm for detecting AE signals was written by MohammedHadi Shateri. The tension tests were done in collaboration with MohammedHadi Shateri and the lab technicians.

2. **Ghaib, M.**, Shateri, M., Thomson, D., Svecova, D. "Comparison between Microstructural Analysis of GFRP and CFRP Rebars using Micro Computed Tomography (µCT), Scanning Electron Microscope (SEM) and Acoustic Emission (AE) Techniques," *Submitted to the Composites Part A: Applied Science and Manufacturing Journal),* **[Chapter 5].** I have done the FRP samples preparation for the µCT and SEM investigations, SEM imaging and analysis, µCT imaging and analysis, FFT of the AE signals and their cumulative energy, and the first draft of the article.

3. **Ghaib, M.**, Shateri, M., Thomson, D., Svecova, D. **"**Enhanced source location in pultruded GFRP and CFRP reinforcing bars using a Neural networks (ANN) and micro computed tomography (µCT) scan," *Submitted to the Structural Health Monitoring Journal,* **[Chapter 6].** I have initiated the use of ANN, as I found it a useful tool for analysis of the testing. I have completed the calculation of velocity, AE linear source location using the conventional method, AE source location using ANN method, µCT imaging and analysis, and the first draft of the written article paper. PLBs tests were done in collaboration with MohammedHadi Shateri. Threshold-based algorithm for detecting AE signals was written by MohammedHadi Shateri.

Dedication

To the memory of my dad Mr. Abdul Ameer,

Acknowledgements

All praise and gratitude be to Allah for giving me unlimited support and guidance in the right direction throughout my life.

First, I would like to express my sincere appreciation and gratitude to both my research advisors Dr. Dagmar Svecova, and Dr. Douglas Thomson for their guidance, deep insight, and moral support throughout the project. Working under their supervisions has been a great pleasure and a unique learning experience. I would also like to thank Dr. Neil Hoult, Dr. Sherif sherif, and Dr. Young-Jin Cha for agreeing to be part of my dissertation committee and supporting me with their valuable notes.

My special thanks go to Dr. Ahmad Shalaby, Dr. Basheer Algohi, and Mr. Mohammadhadi Shateri for lending a helping hand.

I would like to acknowledge the assistance provided by the McQuade Heavy Structures Laboratory staff, Dr. Chad Klowak, Mr. Brendan Pachal, and Mr. Grant Whiteside, in testing the samples.

I would also like to extend thanks to Dr. Ravinder Sindhu and Dr. Michael Jackson for helping me with SEM and μCT scanning during this project.

I greatly appreciate the financial support provided by NSERC, University of Manitoba, and SIMTReC.

Finally, my most profound feelings of gratitude are devoted to the person I love most in my life, my mother Suham. She helped and supported me without expecting anything in return. I cannot say enough for what she has done to make my life enjoyable. I am immensely grateful to my husband Maher, my lovely son Mohammed, my lovely daughters

Sura and Alaa, my sister and best friend Liqaa, and my siblings who encourage and give me the strength to go through every challenge in my life.

TABLE OF CONTENTS

LIST OF TABLES

LIST OF FIGURES

LIST OF ABBREVIATIONS

AE – Acoustic emission

AF – Average frequency

ANN – Artificial neural network

Aramid IM – Aramid intermediate modulus

CFRP – Carbon fiber reinforced polymer

Carbon HS – Carbon high strength

Carbon HM – Carbon high modulus

dB_{AE} – Decibel measurement of voltage for acoustic emission

FFT – Fast Fourier transform

GFRP – Glass fiber reinforced polymer

µCT – Micro computed tomography

µs/V – Micro second / voltage

NDT – Non-destructive testing

PLB – Pencil lead break

RA – Rise time divided by amplitude

RMS – Root mean square

ROI – Region of interest

SEM – Scanning electron microscopy

SHM – Structural health monitoring

STFT – Short time Fourier transform

S glass – Strength glass

WT – Wavelet transform

Δ_t – The difference in time

CHAPTER 1

INTRODUCTION

1.1 Background

Corrosion of steel reinforcement is one of the crucial factors which leads to the deterioration of concrete structures. It also reduces the the capacity of structures and service life. This is especially true for structures which have been exposed to severe environmental effects.

Carbon-fiber reinforced polymer (CFRP) and glass-fiber reinforced polymer (GFRP) have been used widely in concrete structures for the last quarter century, either to rehabilitate damaged reinforced and prestressed concrete elements or to erect new ones (ElBatanouny et al. 2014; Mirmiran and Philip 2000) As of 2016, 65 bridges have been built using FRP bars in the USA, and 202 bridges have been built using FRP bars in Canada including bridge decks, parapets, barriers, and sidewalks (Busel 2016).

The advantages of using FRP over the steel reinforcement are (ACI Committee 440 2006):

- High strength to weight ratio: the density of FRP composites is about one-sixth to one-fourth of the steel reinforcement
- High tensile strength: the ultimate strength of FRP bars is about triple of the yielding stress of the conventional steel
- Corrosion resistance
- Electrical insulator

- Nonmagnatic properties
- Durability
- Design flexibility as it can be shaped and sized to meet the requirements
- Colour matching

However, FRP composites have a brittle behaviour and demonstrate a linear stress – strain curve, and have relatively low modulus of elasticity. The modulus of elasticity is in the range of 110 – 140 MPa for CFRP and 45 – 65 GPa for GFRP bars, while the modulus of elasticity of steel is 200 GPa as shown in Figure 1.1. Since FRP materials are relatively new in civil engineering applications and frequently subjected to environmental changes condition, it would be beneficial to use non-destructive testing (NDT) methods that have the potential to detect damage at loads well below failure. This is particularly important for FRP bars as they do not exhibit any external signs of damage until their brittle failure.

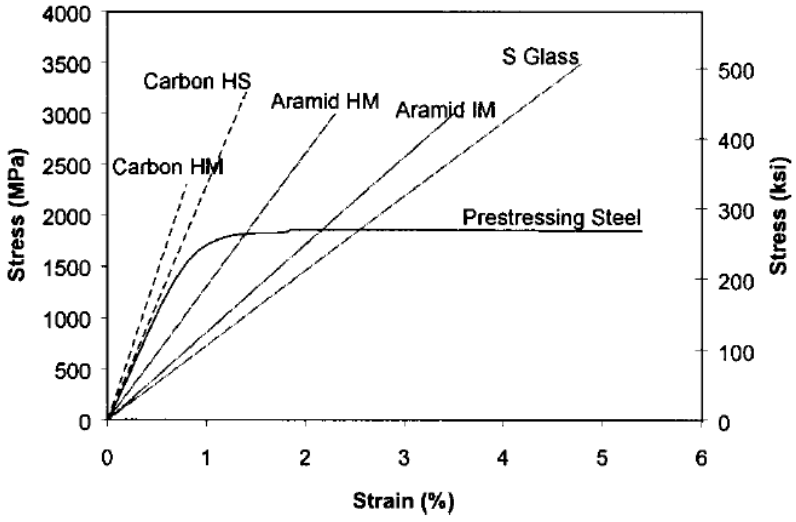

Figure 1.1 Tensile stress strain relationship for FRP rebars compared with steel rebar (Liang et al. 2004, With permission from ASCE)

Several NDT methods have been used to test FRP composites; some of them are applicable for laboratory testing but are impractical for field testing. Some methods need time and are labour-intensive which affects the economic situation of the project, especially for large structures. Most of structural health monitoring techniques are difficult to perform in an in-service structure because of the system size and weight which is used for a such technique. One of the promising structural monitoring techniques that has been used for monitoring the FRP composites during operation is the Acoustic Emission (AE) technique (Prosser 2002). It has been used to inspect structures such as pipes, vessels, storage tanks, concrete, rock, wood, buildings, bridges, railway structures and nuclear power plants (Ohtsu 2008). This research provides a comprehensive study of FRP rebars behaviour under tension using AE technique as a rational first step toward the goal of monitoring in situ damage progression in FRP reinforced concrete.

AE signals are transient elastic waves generated by a sudden release of energy from localized sources within a material (ASTM E1316 2006). These waves are detected by special sensitive sensors installed on the surface of a material such as concrete or FRP composite. Then the information is stored in a data acquisition system and analyzed by using AE parameters. The most sophisticated AE system is able to detect very early age damage under a lower load, even below 10% of the ultimate strength (Ohtsu 2008).

The first AE standard was established in 1982 by the Committee on Acoustic Emission from Reinforced Plastics (CARP) to assess the integrity of FRP tanks and pressure vessels (CARP 1999). After that, additional sections have been added to the standard in order to

use an AE method as a predominant test for highway tankers, man-lifts, and cooling tower fan blades (Ativitavas et al. 2004). The committee has included updated AE research in every field. In addition, the Non-destructive Testing Method Handbook, Vol. 5 included methods on AE application (Miller and McIntire 1987).

These waves could be due to changes of the properties of materials caused by a damage mechanism such as dislocation, micro-cracking, or plastic deformation. In FRP materials, acoustic emission could be due to fiber breakage, matrix cracking (both micro and macro), delamination, debonding, fiber cracking, or fiber pullout (Ziehl 2000).

An advantage of the AE technique is that it has the ability to monitor a region or volume of a structure in one test by attaching an array of AE sensors. This is possible because the method does not require a priori knowledge of the location of the defect. Therefore, it is an attractive method for monitoring materials in larger structures.

1.2 Problem Definition

Several studies have been conducted using AE signals to correlate their amplitude and frequency to damage occurrence in FRP composites such as laminates (Barré and Benzeggagh 1994), sheets (Cole et al. 2006) and stay cables (Rizzo and Lanza di Scalea 2001). The range in frequencies and amplitudes varies depending on the type of signal. It was found that certain amplitudes and frequencies are predominant for matrix cracking, while others correspond to fiber pullout or fiber breakage. Research has been conducted

using aramid FRP (AFRP) and hybrid FRP (HFRP) bars subjected to tension and monitored by AE technique (Chen et al. 1993; Liang et al. 2004) respectively. AFRP and HFRP consist of different percentages of fibers and different kinds of resins. To the best of our knowledge, up to date, CFRP and GFRP bars, which have different properties than AFRP or HFRP, have not been investigated using AE technique.

The literature shows that when FRP composites are subjected to excessive tensile or fatigue loading, these composites will develop internal damage such as matrix cracking, fiber breakage and fiber debonding (Dry 1996; Pang and Bond 2005). Results of these studies give various range of amplitude and frequency for different materials and configurations.

FRP rebars have a linear-elastic (brittle) behaviour that does not provide any warning before failure. Safety concerns have arisen due to the rupture of the prestressed FRP tendons during and after the application of the prestressing in the precast concrete plants. In addition, trapped voids can be developed in FRP rebars along the length of fibers during their manufacturing process. These voids provide possibility of development of weak regions in the bars subjected to stress and lead to changes in the tensile properties of the rebars (Balaguru et al. 2008). Hence there is a need to better understand the progression of damage with tensile loading in FRP reinforcing rebars.

AE signals originates from the rapid release of strain energy due to the damage. This energy propagates as elastic waves and the location of the damage can be determined from the arrival time of the AE waves (Prosser 2002). However, the determination of the arrival

time is complicated by the presence of multiple modes that the AE waves can travel in (Prosser 2002). The challenge of this study is to use a method to reduce the uncertainty in determining AE source location in FRP rebars subjected to tension.

1.3 Scope of Work

The principal objective of this research is to understand the AE signal emitted from FRP rebars subjected to static load until failure. In the current study, AE was studied to investigate the fracture of different diameters of CFRP and GFRP bars during tensile loading. A burst AE signal was generated every time material components undergo cracking or fracture. FRP specimens were tested under increasing tensile loads accompanied by monitoring the AE signals. The response of AE signals was analyzed to identify their sources, using conventional signal analyses in time domain. Amplitude distribution over time, cumulative ratio of the amplitude distribution corresponding to the percentage of the ultimate load, RA (rise time divided by amplitude) and AF (number of counts divided by duration) as a function of time, cumulative counts, and amplitude versus duration, were plotted for this purpose.

Scanning electron microscopy (SEM) and micro computed tomography (μCT) were used to provide information on progression of microstructural damage for comparison with the observed AE signals. The AE from FRP reinforcing rebars was monitored as the rebars were subjected to tensile loading at different percentages of the ultimate load. The internal micro-structure of the loaded rebars was investigated using micro computed tomography

(μCT) and scanning electron microscopy (SEM) imaging. The characteristics of the AE signals were correlated with the μCT and SEM analyses.

In addition, an analysis was performed to locate the source of the AE events in glass fiber-reinforced polymer (GFRP) and carbon fiber-reinforced polymer (CFRP) bars. An artificial neural network (ANN) method was used to estimate the location of the AE signals. The ANN was trained using AE signals generated from pencil lead break (PLB) tests and then the location accuracy was tested also using PLBs. The resulting ANN function was saved for later use to determine the source location in a real time tensile loading test on two different FRP bars. The ANN reduced the uncertainty in determining the AE source location in FRP rebar. μCT damage location analysis was compared in this study to the source location results obtained using the ANN method.

1.4 Research Objectives

The objective of this research is to provide a thorough understanding of the performance of FRP rebars subjected to an increasing and sustained tension load and to study the damage propagation until failure. The performance of these bars was investigated analytically and experimentally.

The main objectives of the research are:

- Studying the behaviour of pultruded FRP rebars using AE signals.
- Relate the results of AE analysis to type of damage in FRP bars using scanning electron microscope (SEM) technique, and hence aid in identifying the origin of these AE signals.

- Compare results obtained from acoustic emission (AE) testing and micro structure analysis obtained by micro computed tomography (μCT) and scanning electron microscopy (SEM) after being subjected to different levels of tensile loading.
- Enhance the accuracy of damage location in FRP rebars using the ANN method. AE signals generated from pencil lead break (PLB) test were used first. The resulted function was saved for later to determine the source location in a real time tensile loading test and to enhance the noise discrimination.

1.5 Research Methodology

CFRP and GFRP bars were subjected to a tensile load and monitored using AE. AE signal analysis was used to detect, locate, and distinguish AE signals coming from the test samples and ones that come from zones outside of the test samples.

The research was carried out in two phases. In the first phase, various types of CFRP and GFRP rebars were tested under an increasing or sustained tension load. The dimensions of the rebar specimens were prepared according to Annex B of the CSA S806-12 (2012) standard. Two resonant transducers were used to pick up the AE data. AE from these FRP rebars was monitored as the rebars were subjected to tensile loading at different percentage of the ultimate load. After loading, the internal micro-structure of the rebars was investigated using μCT and SEM images. For μCT analysis, three dimensional (3D) and two dimensional (2D) μCT reconstructed images were used to study and quantify the void volume and its distribution. In this work the void volume was used as a measure of damage.

In the second phase, analytical work was done using MATLAB. The AE signals were analyzed using the RMS AE hit detection algorithm, and then parameters were extracted in time and time – frequency domain. The signal processing techniques extracted the amplitude, cumulative events, duration, energy, rise time, number of counts, cumulative counts, average frequency, and frequency peaks of the acoustic signals. Short time Fourier transform (STFT) was performed for calculating FFT and energy. Spectrograms using MATLAB were used to obtain the frequency bands that are predominant for both CFRP and GFRP bars at each load level during the test.

Different stages of internal damage of the specimens were identified and related to micro – crack propagation and to the failure of FRP bars. Furthermore, the analysis of recorded AE data was developed to attain accurate damage location and logical signal discrimination using ANN in MATLAB.

1.6 Anticipated Research Contributions to the State of the Knowledge

The major contribution of the research can be briefly described in the following:

- The AE in FRP bars under tension testing was studied. The AE signals were classified and correlated with different damage mechanisms in FRP bars using SEM and μCT.
- The AE activity was observed to increase with load level until failure.

- In FRP rebar the volume of voids in as manufactured and after tension testing were studied and quantified using μCT and SEM imaging. In addition, the cumulative energy of FFT acoustic emission signals were correlated with the percentage volume of the voids in μCT. The void volume was found to increase with load until failure and was correlated with AE signal cumulative energy.
- The ANN method was used to improve the accuracy of determining AE source location in FRP rebar. The trained ANN was saved and used for a later tensile loading test on the same rebars. An additional contribution of this study is a comparison between the density of location of AE signals determined by the ANN method with damage density measured with μCT analysis along the same FRP rebars.

In conclusion, this work can help with the development of data analysis method using signal processing to study the characteristic of AE signals from the recorded data in order to monitor the internal changes in FRP bars, distinguish between possible types of damage, and locate the AE sources. The acoustic emission characteristics presented in this work show strong correlations with ultimate load, and may prove useful for damage prediction. In addition, the AE characteristics may be useful in setting a data base for monitoring FRP rebars.

The analysis of FRP rebars by μCT method may be useful for estimating quality and consistency of pultruded FRP rebars, which is important for a manufacturer in tracking changes in the quality due to entrapped air during manufucturing processes and due to some

microcracks that occurred during the thermal stresses. The μCT method looks promising in determining the structural integrity of the FRP rebars as a result of tensile loading that may play a significant role in determining the long-term durability of the rebars.

CHAPTER 2

LITERATURE REVIEW

2.1 Introduction

The following chapter provides a general information about FRP rebars and a summary of literature review on testing FRP composites using the AE technique. In particular, FRP as a material and its fabrication are briefly described first. Then, the structural health monitoring techniques are presented. After that, AE principles and parameters are defined, and the definition of AE parameters that help with interpretation of the AE data are mentioned for a completence. The past research on FRP composites using AE technique, SEM, and μCT scan are described.

2.2 FRP Composites for Civil Structure

The use of FRP in civil engineering structures started in the 1980s. Many structures have used these rebars for either retrofit, reinforcement, or prestressing (Bakht and Mufti 2015).

FRP rebar is a composite material manufactured from high-strength fibers embedded in a matrix to bind and protect the fibres. The main types of fibers are aramid, carbon, and glass, and the most common types of matrices are epoxy and ester (Balaguru et al. 2008). The fibers carry the load and the matrix protects the fibres from corrosion and transfers load between fibers. The most common method used to fabricate FRP rebars is pultrusion.

It is an automated process that produces products with a constant cross section. The reinforcing fibers are pulled from the creels, collected into a bundle in the guide plate, and then impregnated in a resin bath. Then the bundle is directed to the performer to get rid of the excessive resin and to mold it into shape. Then the product is directed to the heated die to form the final cross section and cure the resin. At the final stage, the cured product is passed through a cut-off saw to be cut into the required length (Kopeliovich 2012). Figure 2.1 illustrates the pultrusion process.

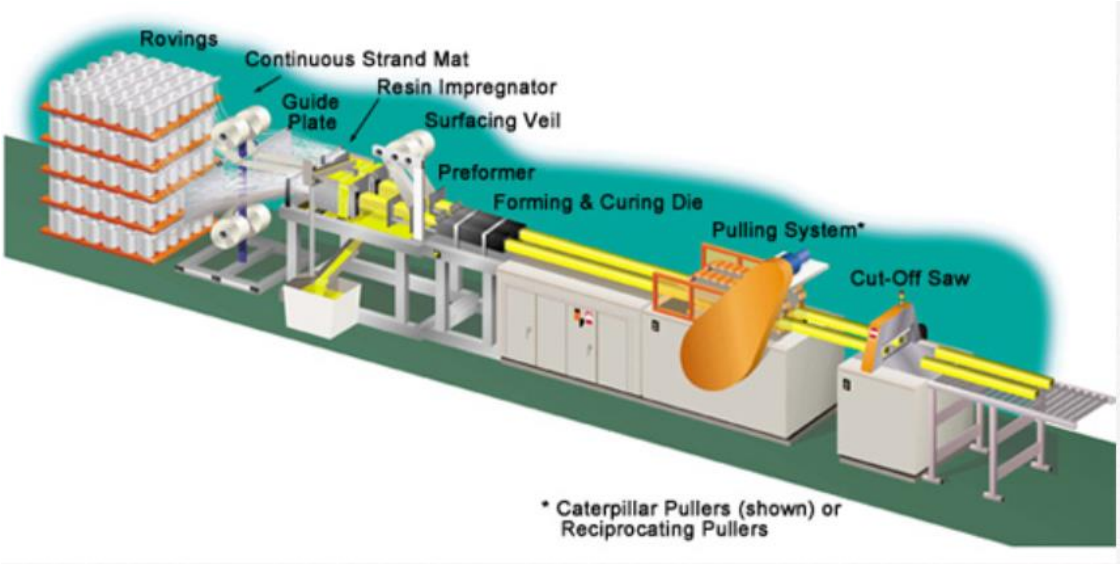

Figure 2.1 Schematic of pultrusion manufacturing process of FRP rebars (used with permission) (“Strongwell: The pultrussion process” 2018)

2.3 Structural Health Monitoring

Structural health monitoring (SHM) is defined as a system of sensors, attached to a structure that is used to understand the performance of a structure under its service conditions. The integral components of the SHM system are: measurements and sensing; structural identification; damage identification; and decision making (Ettouney and Alampall 2011).

Several techniques are available for SHM. Some of them are classified as a global method and other as a local method. Visual inspection is a simple global monitoring method that is achieved by training personnel to inspect a structure for any sign of defect and report the extent of the problem and suggest an appropriate solution (Holford et al. 2001). A tap test is another simple method that involves tapping the surface of a structure by a hammer and listening to its response to determine the area that has a defect (Chang and Liu 2003). Both the visual inspection method and the tap method require personnel with prior experience using these methods, while the results are also subjective.

There are some non-destructive monitoring techniques that are classified as local monitoring methods. Some of them use mechanical waves such as ultrasonic (includes pulse echo and through transmission methods), thermography, Acousto-ultrasonic, and acoustic emission methods. Others use electromagnetic waves such as radiographic and electromagnetic (such as Eddy Current, Remote Field, and Magnetic Flux Leakage electric) (Chang et al. 2003). Another local monitoring method is fiber optics that are used to sense

the strain and temperature of the civil structures such as bridges, pipes, buildings, dams, piles and tunnels (Deng and Cai 2007) . Another type of testing is called Shearography test that uses a laser to detect delamination in a structure (Gholizadeh 2016). As mentioned before, most of these techniques are not possible to perform in an operating structure because of the system size and weight which is used for a such technique. Accordingly, a real time structural health monitoring that is possible to perform through an in-service structure is demanded. AE on the other hand, is a suitable technique that can be used to monitor the FRP composites during their operation since it is able to achieve the goal of detecting and localizing an early defect.

2.4 Acoustic Emission Technique

Acoustic emission has been identified as a promising technique for a real time monitoring for its ability to detect a damage and the damage progress during the structures' service life (de Oliveira and Marques 2008). AE technique has been used to evaluate materials such as concrete, metal, and composites. When a material is subjected to load, strain energy is released in a location where a change in the microstructure occurred. This energy propagates as elastic waves that are called acoustic emission signals (AE). In FRP, these AE waves could be due to fiber breakage, debonding, matrix cracking, and fiber pull out (Ziehl 2000). Ziehl (2000) tested coupons that were cut from larger plates of glass vinyl ester and polyester with a variety of geometries, fibers oriented at 0^0, 45^0, and 90^0 to the applied load and woven roving specimens. The results showed that AE damage mechanisms are affected by the geometry of FRP specimens and the applied load. For

instance, damage mechanisms for specimens loaded perpendicular to the fiber direction were fiber matrix-debonding and matrix cracking. In comparison, damage mechanisms for specimens loaded parallel to the fiber direction were fiber-matrix debonding, fiber pullout, fiber breakage, and matrix cracking. For woven roving specimens, all those five types of damage mechanisms are possible. The results showed that the onset of the damage for more flexible resin such as 0^0, 45^0 and woven roving specimens started in a higher stress than 90 degree specimens (Ziehl 2000).

2.5 Acoustic Emission Principles

The general working principle of acoustic emission starts with force acting on a material and causing damage at a specific point. The damage produces elastic waves that propagate to the surface of the material and cause it to vibrate until these waves reach AE sensors. High sensitivity sensors contain a thin disk of piezoelectric crystal, which lies inside a protective housing and converts the detected waves (elastic displacement) into electrical signals of 1μv (Ohtsu 2008) and produces a change in voltage in response. AE signals produced are often very small to be detected; thus, a preamplifier and amplifier are used to amplify the signals for further processing with a gain given in decibels (dB). In concrete, signals are amplified with a gain range from 60 to 100 dB (Grosse and Ohtsu 2008). The transducer also contains filters that define the frequency range to be used and eliminate background noise such as mechanical rubbing and electromagnetic interference before the signals are passed to the data acquisition system. These signals are filtered by band-pass filter with a frequency ranging from 1 kHz to 2 MHz depending on the noise level and the

attenuation property of a material. Finally, these signals are sent to the data acquisition system to be stored for later analyses. Figure 2.2 illustrates the process of AE monitoring.

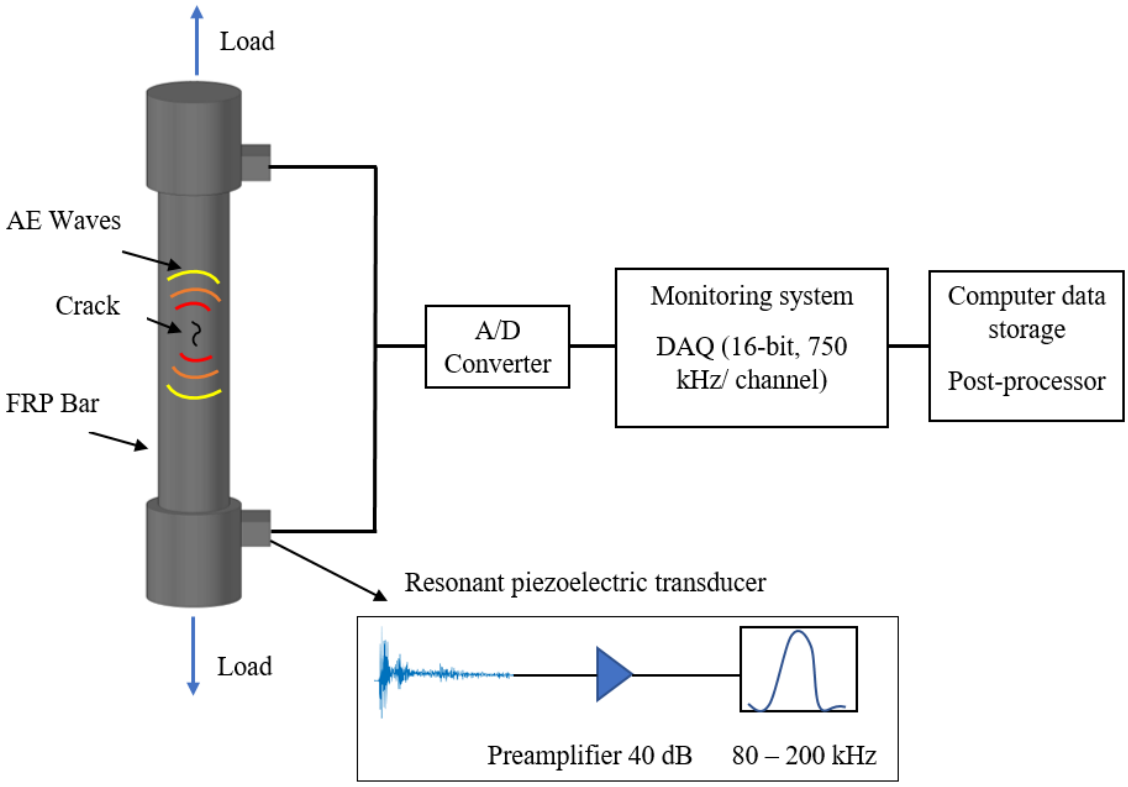

Figure 2.2 Schematic of the AE Monitoring Process

2.6 Acoustic Emission Advantages and Disadvantages

Studies of AE signals have been conducted for more than half a century. The studies were able to come up with several advantages and some disadvantages of this non-destructive monitoring technique.

The main advantages of using AE technique are:

- Ability to provide real time structural health monitoring without shutting down a structure, which increases its practical value.

- Highly sensitive that can detect the early cracks and flaws

- Applicability for local and global monitoring of active defects since the method does not require a priori knowledge of the location of the defect. The whole structure can be evaluated quickly and effectively in one test by attaching more sensors.

- Ability to detect the location of the damage and monitor its growth by using multiple channel sensors.

- Economic feasibility for extending the life of the structures without the need for intensive labor.

The main disadvantages:

- It needs specialist skills to interpret the information from the source and distinguish among different types of damage.

2.7 Basic Parameters of AE Signals

AE is a wave generated by a sudden release of energy. The strength of acoustic signals is determined by the damage growth, the distance between the damage source and the sensors,

the acoustic properties of the transferring material, the sensor type, and the wave path (ASM International Handbook Committee 1990). After amplification and digitizing, an AE signal is represented as a voltage vs. time plot. AE waves can be analyzed in three domains: time domain, frequency domain, and time-frequency domain. Basic parameters in time domain are shown in Figure 2.3.

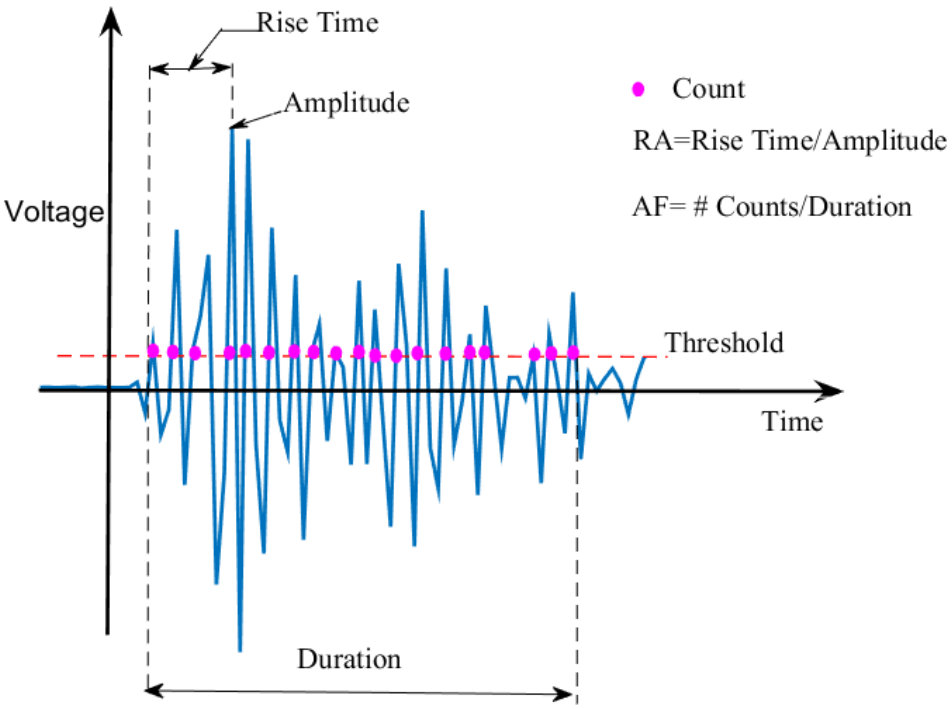

Figure 2.3 AE signal characteristics

These AE parameters are commonly used in AE processing technology (Miller and McIntire 1987). By applying these parameters, damage initiation and development can be monitored. The basic signal parameters are:

1. Amplitude: is the maximum voltage peak within the signal duration and is measured in decibels (dB). A decibel is defined as "the logarithmic ratio of signal peak amplitude to fixed reference amplitude" (ASTM F1430 2005). A decibel scale range is from 0 to 100 where 1μV at the sensor is referred to 0 dB.

$$Signal\ peak\ amplitude\ (dB) = 20\log_{10}\left({}^{V_1}/_{V_0}\right) - preamplifier\ gain\ in\ dB$$

…….. (2.1)

Where: V_0 = 1 μV at the sensor output (before amplification), and V_1 = peak voltage of the measured acoustic emission signal.

2. Threshold: is the level which determines the onset of the damage. If the absolute amplitude of the signal is below this level, that means the signal is produced by background noise. It would be filtered out. Threshold level may be user adjustable, fixed or automatic floating based on the background noise (ASTM F1430 2005).

3. Duration: is the time of a signal from the first point exceeding the threshold level to the last one. It measures the source magnitude, so it is important to characterize different types of sources. The unit of measurement is microsecond (millionth of a second) (ASTM F1430 2005). The Amplitude – duration relationship helps to identify signal's shape.

4. Counts: is the number of times which the AE signal crosses the threshold level. Typically, the counts that start from crossing threshold level to the peak amplitude are called "counts to peak" (ASTM F1430 2005).

5. Rise time: is the time measured from the first point of the signal exceeds the threshold level to the maximum peak amplitude. This parameter is important to measure the capacity of signals as it is related to the source – time function. The unit of measurement is also microsecond (ASTM F1430 2005).

6. Event: is the rise of an AE activity indicated by a damage onset in a material. A single event may contain few or hundreds of counts. It is used for interpreting the AE data (ASTM F1430 2005).

7. Energy, MARSE: is the measured area between the squared signal envelope and the threshold level within the duration of time. It is expressed in logarithmic form (dB) and measured in joules (ASTM E1316 2006).This parameter is preferred in quantifying the AE activity rather than the counts or hits as it is more sensitive to the amplitude and duration, and it is less dependent on the voltage threshold and operating frequency (Grosse and Ohtsu 2008).

$$E_n = \sum power\ signal = \sum x^2[n] \quad \ldots\ldots\ldots\ldots\ldots\ldots\ldots\ldots\ldots\ldots\ldots\ldots\ldots\ldots \quad (2.2)$$

8. Arrival time: is the first time that an AE signal exceeds the threshold level (ASTM F1430 2005).

9. Channel: is an AE sensor, and the other related instrumentation which detects, transmits, and measures the signal within it (ASTM E1316 2006).

10. Average Frequency: is the ratio between the AE counts and the duration; it is measured in kHz (ASTM E1316 2006).

$$A.F. = \frac{AE\ counts}{duration}\ (kHz) \qquad \ldots\ldots\ldots\ldots\ldots\ldots\ldots\ldots\ldots\ldots\ldots\ldots\ldots\ldots\ldots\ldots \qquad (2.3)$$

11. RA value: is the ratio between the rise time and the amplitude; it is recorded in μs/V. It is important to categorize the type of cracks.

12. Attenuation: is the loss of energy when a wave travels outward from the source due to some factors such as: dispersion, scattering, and conversion to other kinds of energy such as heat (Prosser 2002). This parameter depends on the distance between a source and sensors and the properties of the material to be tested (ASTM F1430 2005). Consequently, the signals can be recorded up to a specific distance and this will limit the distance of sensor placement. The number of sensors should be limited in monitoring large structures for economic reason. Hence, a careful selection of the sensors placement in a large structure where the defect is likely to take place is important. The attenuation is computed using:

$$A_f = A_0 e^{-\alpha d} \qquad \ldots\ldots\ldots\ldots\ldots\ldots\ldots\ldots\ldots\ldots\ldots\ldots\ldots\ldots\ldots\ldots \qquad (2.4)$$

Where: A_f is the amplitude at the sensing location, A_0 is the initial amplitude at the source location, α is the attenuation coefficient, and d is the travelling distance (Maillet et al. 2014).

AE signals could be released in two types of signals, burst (transient) and continuous signals as shown in Figure 2.4. The burst emission is a discrete signal which has high amplitude and energy. In other words, it has start and end points caused likely by crack propagation or fracture formation. The continuous signal is a sustained signal which has variation in amplitude in low energy with no ending point. Burst signals often refer to a fracture or crack propagation, while continuous signals refer to noise signals (GI-MR 2009). Table 2.1 summarizes the AE parameters and information about their source events.

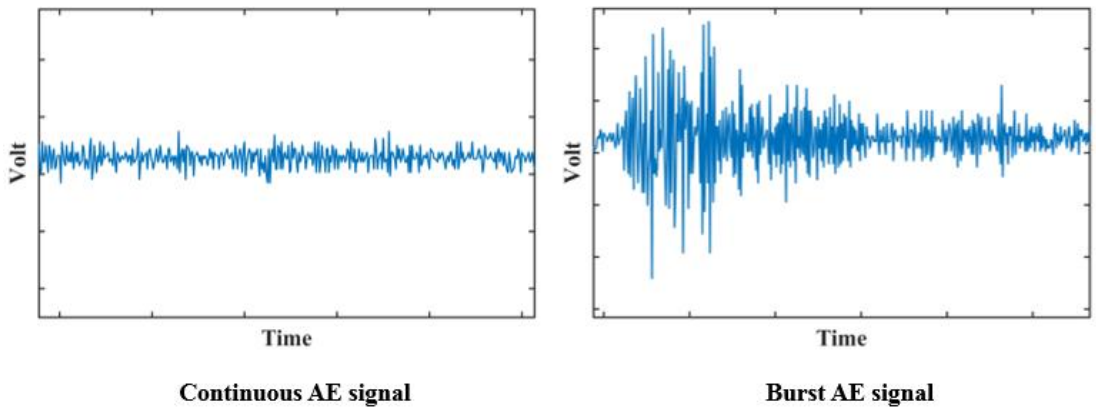

Figure 2.4 Examples of a continuous AE signal compared to a burst AE signal

Table 2.1 AE parameters and information provided about the source event (reproduced from Ozevin et al. 2004)

Domain	**Parameters**	**Information about the source event**
	Rate	Rate of damage occurring
	Peak amplitude	Intensity of source event, orientation
Time domain variables	Relative arrival times	Source location
	Duration or count	Energy of source event
	Waveform	Structure of source event
	Energy	Energy of source event – damage type
Frequency domain variables	Frequency spectrum	Nature of source event
Time – frequency domain variables	Spectrogram	Energy distribution of source event through time
	The time variation of each frequency component	The intensities of source frequency components

2.8 Derived Parameters of AE signals

2.8.1. Kaiser Effect & Felicity Effect

Kaiser effect is “the absence of detectable acoustic emission at a fixed sensitivity level, until previously applied stress levels are exceeded” (ASTM E1316 2006). Felicity effect is “the presence of detectable acoustic emission at a fixed predetermined sensitivity level at stress levels below those previously applied” (ASTM E1316 2006). Figure 2.5 describes the Kaiser and Felicity Effects.

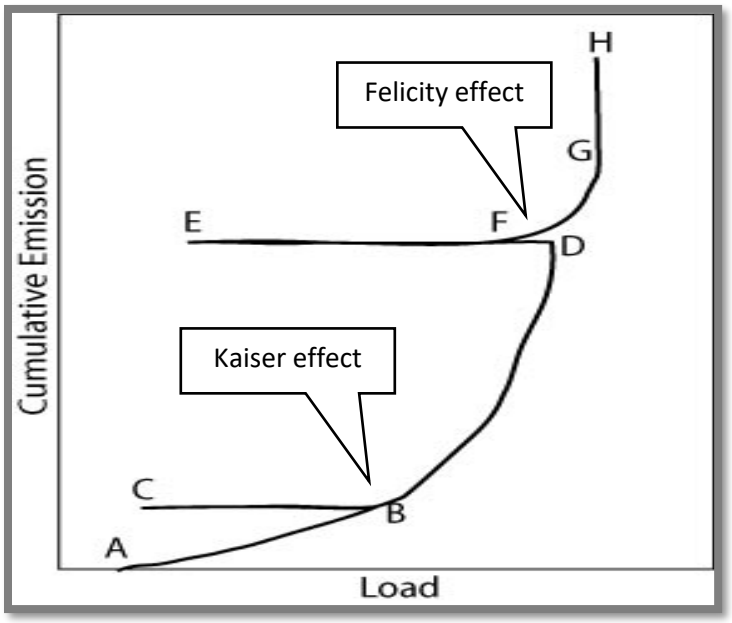

Figure 2.5 Kaiser and Felicity Effects (Reproduced with permission from the NDT Resource Center and Center for NDE, Iowa State University) (NDT 2014)

The Kaiser effect is described in (BCB) when a specimen is unloaded (from B to C) then reloaded (from C to D) and no emissions are produced during unloading or reloading until the previous load is exceeded (from B to D). The Kaiser effect is a good indication for structural integrity (Ohtsu 2008). The Felicity effect is described in (DEF) when a specimen is unloaded (from D to E) then reloaded (from E to G), and AE are produced at F within reloading before the previous load is reached at D. The Felicity effect is an indication of significant damage when it is less than one (Ohtsu 2008).

$$Felicity\ ratio = \frac{stress\ at\ onset\ of\ AE}{previous\ maximum\ stress} \quad \ldots\ldots\ldots\ldots\ldots\ldots \quad (2.5)$$

The Felicity effect has been investigated in several studies. One study was carried out in 1996 where corroded concrete specimens with 1 mm and 4 mm wide cracks were subjected to four – point bending, and monitored by the AE technique (Murakami and Yuyama 1996). The results indicated that the felicity ratio reduces as cracks increase (Murakami and Yuyama 1996).

2.8.2. Calm Ratio & Load Ratio

Calm ratio is the ratio between the number of cumulative AE activities within the unloading process and the total AE activities within the last maximum loading (Ohtsu et al. 2002).

Load ratio is the ratio between the load level at the time AE hit is detected within the loading cycle and the preceding load level (Ohtsu et al. 2002). The calmand load ratio

parameters were derived by Ohtsu et al. (2002) in a study that tested reinforced concrete beams under cyclic loading with the intention of evaluating damage progression. The result of this study became part of the Japanese code for non-destructive testing NDT (Ohtsu et al. 2007). The calculations of these ratios were schemed and divided into four regions; each region represented a damage level as shown in Figure 2.6)

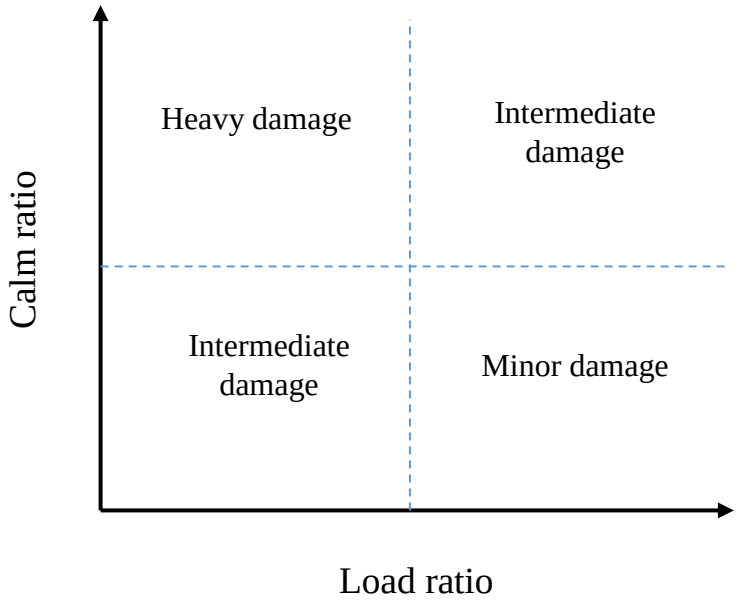

Figure 2.6 Damage evaluation in term of calm ratio vs load ratio (reproduced from Ohtsu et al. 2007)

2.8.3. Historic Index & Severity

Historic index (H(I)) is an analytical method of tracing the abrupt change (knee) of the slope of the cumulative AE signal strength against time. It is calculated as a ratio of the

average signal strength of the last few events to the average signal strength of all events up to that point (CARP 1999):

$$H(I) = \frac{N}{N-K}\left[\frac{\sum_{t=k+1}^{N} S_{oi}}{\sum_{i=1}^{N} S_{oi}}\right] \quad \ldots\ldots\ldots\ldots\ldots\ldots\ldots\ldots\ldots\ldots\ldots\ldots\ldots\ldots\ldots\ldots \quad (2.6)$$

Where: *N* is the number of hits up to the point. S_{oi} is the signal strength of a particular hit. *K* is the empirically derived constant based on a type of material and number of events.

The severity (Sr) is calculated as the average signal strength of (j) events having the maximum value of signal strength (CARP 1999):

$$S_r = \frac{1}{J}\left[\sum_{m=1}^{J} S_{om}\right] \quad \ldots\ldots\ldots\ldots\ldots\ldots\ldots\ldots\ldots\ldots\ldots\ldots\ldots\ldots\ldots\ldots \quad (2.7)$$

Where: S_{om} is the signal strength of the m^{th} event where the ordering of m is based on signal strength magnitude, m=1 when the event having the largest signal strength. *J* is the empirically derived constant based on a type of material and number of events. The *K* & *J* values for FRP materials are defined in Table 2.2.

Table 2.2 *K & J* values for FRP (CARP 1999)

Number of Hits	*K*	*J*
< 20	Not Applicable	Not Applicable
20-100	0	20
101-500	0.8 *N*	20
> 500	*N* -100	20

The *K & J* values for concrete are defined in Table 2.3 below.

Table 2.3 *K & J* values for concrete (Golaski et al. 2002)

Number of Hits	*K*	*J*
≤ 50	0	0
51-200	*N*-30	50
201-500	0.85 *N*	50
> 500	*N*-75	50

Hence, the historic index and the severity are important parameters for intensity analysis which helps to identify the onset of a significant damage and its propagation. The intensity of an acoustic emission source can be determined by plotting severity vs historic index in a log-log chart as shown in Figure 2.7. The zones A to E are explained in Table 2.4.

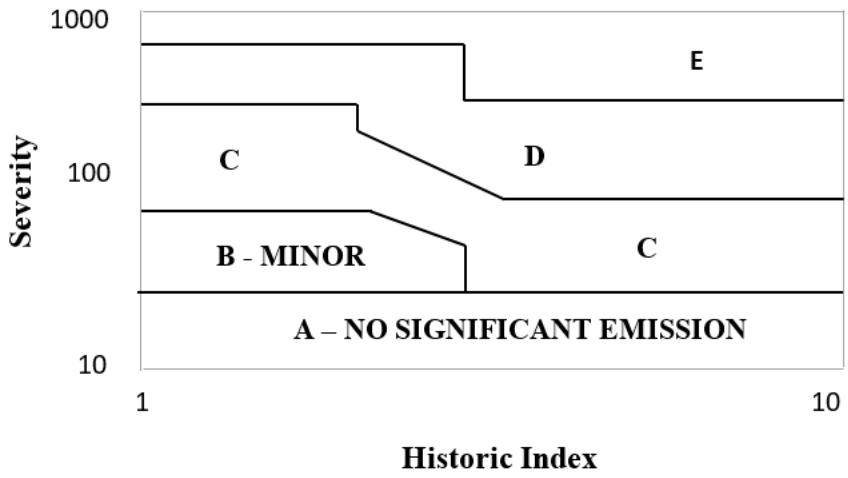

Figure 2.7 Intensity analysis zones for FRP vessel (reproduced from Gostautas et al. 2005)

The resultant plot can be divided into these zones based on structural damage level. The values of maximum damage are plotted on the top right-hand corner while the minor damages on the bottom left-hand corner (Gostautas et al. 2005). The zones intensity is shown in Table 2.4.

Table 2.4 Zone intensity and their recommended action (reproduced from Gostautas et al. 2005)

Zone Intensity	Recommended action
A – No significant emission	Insignificant acoustic emission. No follow-up recommended
B – Minor	Note for reference in further tests. Typically, minor surface defects such as corrosion, pitting, gouges, or cracked attachment welds
C	Defect requiring follow-up evaluation. Evaluation may be based on further data analysis, or complementary non-destructive examination
D	Significant defect requiring follow-up inspection
E	Major defect requiring immediate shut–down and follow–up inspection

2.9 AE Analysis in Frequency Domain and Time – Frequency Domain

Signal processing techniques have been developed making waveform-based AE analysis more applicable. AE signal processing methods include time series analysis, Fourier transform (FT), Short timed Fourier transform (STFT, also known as Gabor or windowed Fourier transform), and Wavelet transform (WT).

Several studies have proved that frequency analysis is an effective method to distinguish signals from different damage mechanisms in FRP composites (Bohse 2000; de Groot et al. 1995; Gutkin et al. 2011; Kamala et al. 2001; Ramirez-Jimenez et al. 2004; Russell and Henneke 1977) Summary of their results are found in Table 2.5. The studies were performed on laminates, plates or sheets. Other techniques were used in some of these studies to confirm the findings such as the optical microscope and the television camera in (Russell and Henneke 1977); the light microscopy in (Bohse 2000); the SEM micrograph in (Ramirez-Jimenez et al. 2004); and the ultrasonic scanning in (Gutkin et al. 2011).

Table 2.5 Summary of Frequency Analyses

Study	Year	Material type	Test Type	Analysis Technique	Findings / limitations
Russell & Henneke,	1977	Graphite Epoxy Laminates	Tensile	Spectrum Analysis	50-150 kHz Matrix Cracking 140-180 kHz Fiber Failure
Suzikie et al. (from De Groot et al 1995)	1988	Glass Polyester Composites	Tensile	Frequency Analysis	(30–150) kHz Matrix Cracking 30-100 kHz Delamination (180–290) kHz Fiber Debonding and pull-out 230-450 kHz Debonding (300–400) kHz Fiber Failure
De Groot et al.	1995	Unidirectional Carbon Fiber / Epoxy Composites (Plates)	Tensile	Frequency Analysis	(90-180) kHz Matrix Cracking (180-240) kHz Fiber Pull-out (240-310) kHz Debonding > 300 kHz Fiber Failure
Bohse	2000	Single Carbon Fiber/Epoxy Laminate Single Glass Fiber/Epoxy Laminate	Tensile	Frequency Analysis	70% of the signal power< 350 kHz Matrix Cracking 70% of the signal power> 350 kHz Fiber Failure In between Debonding
Kamala et al.	2001	Carbon Fiber Reinforced Composites (Laminates)	Tensile Fatigue	Time-Frequency Analysis (DWT)	120 kHz Matrix Cracking 250 kHz Debonding 300 kHz Fiber Failure

Table 2.5 Cont'd Summary of Frequency Analyses

Ramirez-Jimenez et al	2004	Glass Polypropylene Sheets	Tensile	Frequency Analysis	100 kHz Debonding 200-300 kHz Pull Out 420-500 kHz fiber Failure
Gutkin et al.	2011	Carbon Fiber Reinforced Laminates	Tensile	Frequency Analysis (Pattern Recognition)	(0–50) kHz Matrix Cracking
			Compact tension		(50–150) kHz Delamination
			Compact compression		(200–300) kHz Debonding
			Double Cantilever Beam		(400–500) kHz Fiber Failure
			Four-point End		(500–600) kHz Fiber Pull-out
			Notched Flexure		

Fast Fourier transform (FFT) is generally used to recognize the signal frequency content, but it is unable to record information about the time of frequency occurrence. Since AE waveforms are presented in both time and frequency domains and provide a valuable data, joint time – frequency technique is important. The WT and STFT analyses are powerful time – frequency technique that can provide pertinent information from the AE signals to determine damage types in the composites (Hamstad et al. 2002; Kaphle and Tan 2011). The STFT calculates the Fourier transform by dividing the signal into stationary parts; a short window function is used to extract the parts from the original signal, and then the window is relocated in a new location for the next resolution. The result obtained from the new location of the window is the time – frequency localization, and that has a constant localization resolution due to the limited length of the window. Information about the energy and frequency content at a specific time can be obtained using this method. The WT uses a scaled window in variable sizes. Long-time interval windows are used in cases where accurate low frequency is required, while the short-time interval ones are used in cases where high frequency is preferable (Mathworks 2009). Mathematical derivation of the STFT and WT, their reconstruction methods, and their stability are discussed in detail by (Daubechies 1990). Information about the energy and frequency content at a specific time can be obtained using this method.

Although wavelet transforms can be performed for both continuous and discrete data, the discrete type (DWT) is fundamental in distinguishing between AE signals. It allows decomposing the signal into continuous frequency bands depending on different levels of decomposition (Mallat 2009). Thus, it is possible to represent different damage

mechanisms in different frequency bands by using DWT. The principal of the DWT is that the original signal passes through two complementary filters, low and high pass filters, and two signals are obtained, correlating with the approximation and detail coefficients of the first level. For the next resolution, the two filters are applied to the resulting approximation coefficients and so on. The approximations are high scale and low frequency, while the details are low scale and high frequency components. The sum of the signals obtained at each level reset the original AE signal. The DWT has two disadvantages. First, the analysis depends on the time, so a small shift in the time results in entirely different coefficients. Second, it is very sensitive to noise because of its ability in detecting sharp changes (Unnþórsson 2008).

Kaphle et al. (2012) simulated AE signals on a long steel beam by breaking pencil leads at specific locations on the specimen. The STFT and WT were performed on the initial signal that had duration of 1000 μs and was recorded by three sensors located at different corners of the plate. The results showed that the frequencies lie on a narrow band around 150 kHz. The results concluded that the WT method was unnecessary to be used since similar patterns of the frequency bands were found for both methods (Kaphle et al. 2012b).

Kaphle et al. (2012) calculated the energy distribution in the AE signals by using an STFT matrix. The coefficients of this matrix are $C(\omega_i, \tau_j)$, where ω_i represents FFT in rows and τ_j represents time in columns. The normalised energy ratio as a function of frequency ($E_{(\omega)}$) can be calculated as follows:

$$E_{(\omega)} = \frac{\sum_{j=1}^{N} C^2(\omega_i,\tau_j)}{\sum_{i=1}^{M}\sum_{j=1}^{N} C^2(\omega_i,\tau_j)} \quad \ldots\ldots\ldots\ldots\ldots\ldots\ldots\ldots\ldots\ldots\ldots\ldots\ldots\ldots\ldots\ldots \quad (2.8)$$

Where *N* is the numbers of columns that represent the time, and *M* is the number of rows that represent the frequency. Studying energy distribution in the time – frequency domain is expected to provide important information about the nature of the damage source. Energy distribution does not vary with the change of the distance between the sensor and the source, i.e. it is not affected by the signal attenuation (Kaphle et al. 2012b). Energy distribution as a function of frequency was performed to find the frequency bands that are predominant in specific signals.

2.10 Acoustic Emission Transducers

There are various types of acoustic emission transducers used in different structures and materials. The most significant factor for the AE to be successful is the choice of a correct transducer in terms of sensitivity and frequency response. Generally, the AE transducers are piezoelectric (PZT) devices. The frequency response is affected by the size and the type of the transducer (ASTM E1316 2006). In order to insure an effective transition of the AE signals from the test specimens to the transducers, a suitable coupling is required. The AE transducers are attached to the surface of the structure using magnetic holders or glues. The frequency range of the transducers varies from (20 kHz – 2.2 MHz) depending on the sensor type and the material under testing (Vallen 2002). In FRP composites, sensors with range of 100 kHz – 200 kHz are applicable (CARP 1999). Figure (2.8) below shows the commercial types of the transducers.

Figure 2.8 Vallen System Sensor Collection. (Used with permission of Vallen System)

Two types of piezoelectric transducers are used in FRP monitoring, resonant and broadband (wideband) transducers. The resonant transducers have varying frequencies appropriate for concrete: (R6I) resonant with sensitivity equal to (40-100) kHz and R15I resonant with sensitivity equal to (80-200) kHz. The resonant sensors are less expensive and more sensitive at their resonance frequency (Vallen 2002). Accordingly, this type is used near the damage source to minimize amplitude attenuation and in other cases that other AE features rather than frequency content are required. Other AE features such as energy, amplitude, and arrival time should be recorded with the same type of sensors. The broadband sensors are preferred for practical structural monitoring in case background noise is the problem such as friction and impact which results from the surrounding environment and in case the frequency or model analyzing is required (Vallen 2002). It is important to know that one type of damage mechanism can produce different signals from

different locations, and different types of damage mechanisms can produce different signals from the same location. Thus, it is crucial to choose an appropriate type of sensor and frequency filter to identify the source mechanism and its propagation.

2.11 Fields of application of AE technique

The AE technique has been used efficiently for characterization of such materials as concrete, composites, metals, and rocks. It is also used for the design optimization, in-process monitoring, acceptance tests, and in-service condition / SHM in structures (Czichos 2013). It is applicable for three major fields: structural testing and surveillance, process monitoring and control, and materials characterisation (Scruby 1987).

2.11.1 Application of AE to FRP

A significant number of studies have focused on studying the AE signals characteristics of FRP composites under different loading tests in order to predict their failure mechanisms. First study in this field had been conducted by Fuwa et al. (1975), by testing cyclically-loaded carbon fiber plastic (CFRP) laminate samples at high stress levels in both ordinary tensile testing and acoustic emission method. The results showed that the damage mechanisms for both methods are the same, and that CFRP do not have a significant damage with fatigue loading. Furthermore, the results indicated that the AE behaviour is time-dependent deformation of the resin matrix that allows forces in the fiber to redistribute gradually. In addition to that, the results indicated that AE count rate decreases with time

during cyclic loading and stress relaxation until the sample becomes silent prior to failure (Fuwa et al. 1975).

Valentin et al. (1983) applied the AE on two types of carbon – fiber reinforced epoxy composite, unidirectional and crossplied (0^o, 90^o) specimens. The specimens were loaded under tensile test to failure in two directions, perpendicular and parallel to the fiber orientation. The results showed that the cumulative amplitude distribution for the unidirectional specimen was linear, while for the cross plied specimen it was bilinear. Also, the results showed that high amplitude signals were released from matrix cracking parallel to the fiber, while matrix cracking perpendicular to the fiber was negligible. In addition, low amplitude signals were released from fiber breakage (Valentin et al. 1983). On the other hand, Komai et al. (1991) provided a range of AE amplitude for CFRP Composite sheets suggesting that: signal with amplitude less than 60 dB was from interfacial debonding, signal with amplitude less than 70 dB was from matrix cracking, and signal with amplitude less than 75 dB was from fiber breakage (Komai et al. 1991).

Ely and Hill (1992) conducted research investigating damage characterization on graphite/epoxy composite samples subjected to tensile tests. By using the AE parameters – counts, duration, and risetime, the results allow the identification of various damage mechanisms. With event duration ranges: 0-40 μsec and peak amplitude at 40 dB matrix cracking was detected, 41-72 μsec and peak amplitude at 58dB fiber breakages was detected, 73-126 μsec with peak amplitude at 63dB fiber pullout was detected, and duration of more than127 μsecs with peak amplitude at 69dB were longitudinal splitting (Ely and

Hill 1992). The results also showed in a later study that fiber breakage and longitudinal splitting occur at the same location in a unidirectional graphite/epoxy specimen, the stronger signals with high amplitude and long duration resulted from the fiber breakage and the weaker ones with low amplitude and short duration resulted from the longitudinal splitting (Ely and Hill 1995).

Iwamoto et al. (1999) applied both parametric and frequency analysis on unidirectional CFRP composites to determine a bridging fiber failure. They realized that bridging fiber failure releases high energy that has frequency between 600 – 700 kHz. The results were confirmed by a power spectrum analysis with a slight difference in determining the location and size of the frequency intervals that were detected (Iwamoto et al. 1999).

Kamala et al. (2001) applied the DWT analysis on CFRP composite under uniaxial fatigue loading. They decomposed the AE signal into different levels, and they concluded that 95% of the AE signal lies at frequency bands of 120, 250, and 310 kHz (Kamala et al. 2001).

Research on glass fiber reinforced composites have been done for damage identification since 1979. Crump (1981) tested many GFRP specimens and analyzed the AE signals to determine that the AE activity increases with the increase of glass percentage in specimens, concluding that fiber breakage was their primary mode of failure (Crump 1981). This study was one of the most significant studies which lead to establishthe Committee on Acoustic Emission from Reinforced Plastics (CARP) code for recommended practice of monitoring FRP pressure vessels and tanks using the AE technique. Suzikie et al. (1998) studied the

AE features, amplitude distribution, and they proposed four ranges corresponding to the acoustic frequency released by different types of damage in glass/polyester composite: 30–150 kHz correlated to matrix cracking, 180–290 kHz correlated to fiber debonding and pull-out, and 300–400 kHz correlated to fiber breaking (Suziki et al. 1988).

Barre and Benzaggagh (1994) conducted research to investigate the damage initiation and progression in short glass fiber reinforced polypropylene under three test types: tensile, tensile fatigue, and crack propagation tests. The study proposed the use of AE in terms of amplitude distribution and the SEM techniques. Four different material compositions were tested in this study. All the materials contained 40% (by weight) of short glass fibers and 60% polypropylene, but had different fiber lengths and production processes. The results allow the identification of damage mechanisms depending on the parameters of the material compositions with ranges of the AE amplitudes: 44-55 dB was correlated to matrix cracking, 60-65 dB was correlated to interface fracture, 65-85 dB was correlated to fiber pull-out phenomena, and 85-95 dB was correlated to fiber fracture (Barré and Benzeggagh 1994).

Bhat et al. (1994) discussed the experimental investigations carried out on twenty-five specimens made from four layered unidirectional glass fibers–epoxy composite specimens subjected to constant fatigue load cycles in a direction parallel to the fibers orientation. The acquired AE data was analyzed using pattern recognition techniques. Stepwise analysis was developed to estimate the parametric distributions. First, the correlation between the rates of AE activities are defined by shifting the peak amplitude from stage to stage.

Second, the classification of the data is employed using pattern recognition techniques for four basic AE parameters: ring down count, event duration, peak amplitude, and rise time. The results indicated three separate damage mechanisms before failure: matrix cracking, interface debonding, and gross fiber failure. Events that arose in the primary stage of fatigue life were correlated to matrix cracking, events that arose in (20% - 70%) of fatigue life were correlated to interface debonding, and events that arose in the last (10%) of fatigue life were correlated to fiber fracture. Furthermore, the cumulative damage was estimated to predict the residual life. The results showed that there was a short time of high AE events followed by a silent period before the failure (Bhat et al. 1994).

Rizzo and Scalea (2001) tested real size carbon fiber reinforced polymer stay cables under large scale laboratory tests, and compared them with the AE responses. The results showed a qualitative correlation between signal amplitude, signal frequency and the type of damage. They performed additional study to identify the signal attenuation and dispersion phenomena, and they reported that they are very important in large structures (Rizzo and Lanza di Scalea 2001).

Ativitavas et al. (2004) developed a low amplitude filtering technique in order to distinguish between different failure mechanisms in fiber reinforced polymer structures. The results showed that the high amplitude of AE hits related to the fiber breakage was separated from others, and the reason was that the fiber breakage demand higher energy than the matrix cracking because the fibers have high strength. The cumulative signal hits

of the filtered signals were correlated to the cumulative signal hits of the fiber breakage (Ativitavas et al. 2004).

Li et al. (2011) performed fatigue tests on GFRP and CFRP cables based on the AE technique and fatigue test. Fractal theory approach was used for the AE analysis. Each test cable was made up of seven GFRP or CFRP strands with the same length and diameter. The time-history and frequency responses of the AE signals were investigated, and the results demonstrated that a fractal dimension-based damage index can quantify damage propagation and provide advanced warning of the FRP cable failure (Li et al. 2011).

Stevenson et al. (2014) tested different types of pultruded CFRP and GFRP rebars, manufactured using continuous fibers, under ramping load. The histogram of the counts in every ten second interval, and the cumulative of these counts were plotted. The results showed that the count rate increases with increasing load, with a maximum peak count rate occurring near failure as shown in Figure 2.9. Also, the results showed that GFRP generated AE events at an earlier stage than the CFRP (Stevenson et al. 2014).

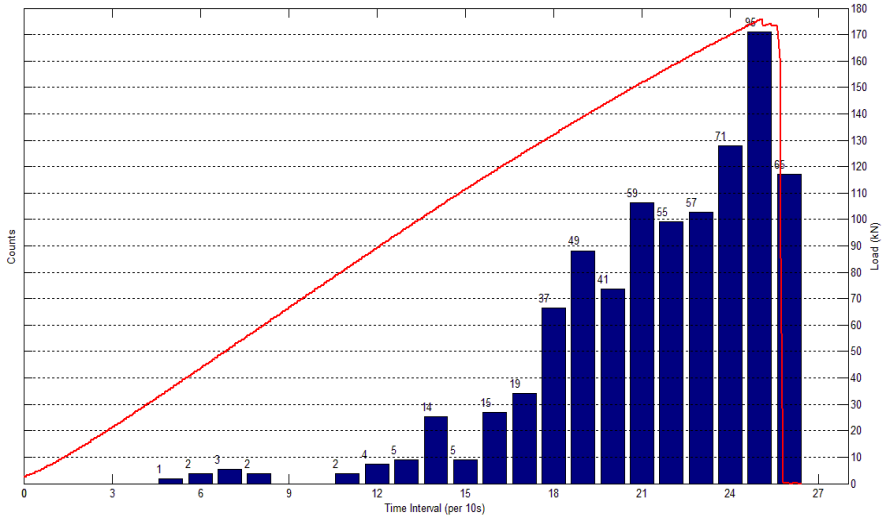

(a)

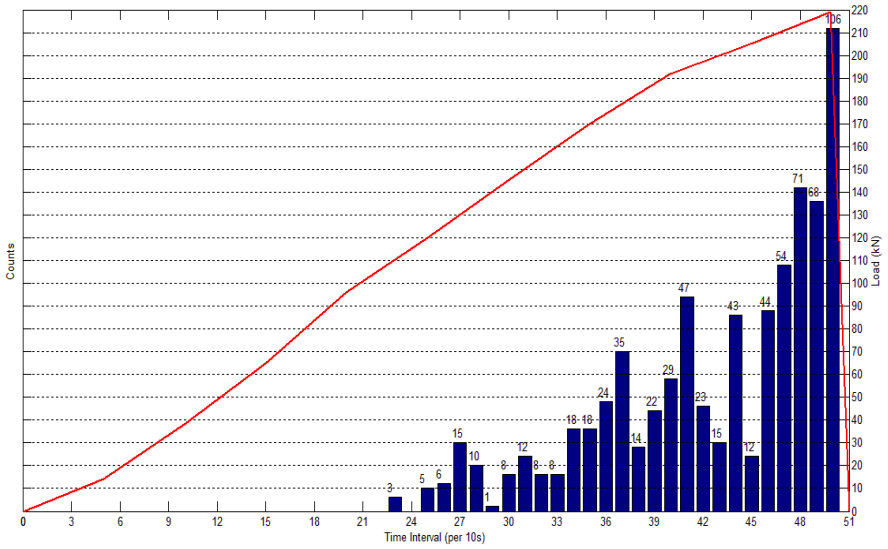

(b)

Figure 2.9 Counts histogram and load increase with time for a) CFRP, b) GFRP (Stevenson et al. 2014)

2.11.2 Application of AE for SHM

Research has proved the suitability of the AE technique in studying the integrity of bridge structures, as it provides continuous in-service monitoring. Many studies were carried out on the use of AE technique detecting the early damage and assessing the health of bridge structures made of different materials (Colombo et al. 2005; Shigeishi et al. 2001; Yoon et al. 2000; Yuyama et al. 2007) applied the AE technique on concrete bridge materials. (Gong et al. 1992; Holford et al. 2001; Sison et al. 1998; Yu et al. 2011, 2013) applied the AE technique on steel bridges, while (Melbourne and Tomor 2006; De Santis and Tomor 2013) applied the AE technique on masonry bridge.

Gostautas et al. (2005) tested glass fiber reinforced composite bridge deck specimens, in both original and repaired conditions, subjected to static load to study their performance and characterize their damage mechanisms. They applied intensity analysis and used Felicity ratio to check the Kaiser effect and the Felicity effect. The results showed that the main kinds of damage mechanisms were matrix cracking, fiber breakage, and fiber delamination. The results also showed that the Felicity ratio is similar to the load ratio, but it is defined as the load ratio where the AE events are observed in the reloading cycle to the previous maximum load level. The Felicity ratio was reported as an important parameter identifying the onset of damage (Gostautas et al. 2005).

Cole et al. (2006) performed cyclic fatigue loading test on a fiber reinforced polymer honeycomb (FRPH) beam strip, of 9760 mm in length $\times$ 305 mm in width $\times$ 910 mm in

height, that was cut from a bridge structure located in Troupsburg, New York. FRPH system consists of thin honeycomb core sheets covered by several layers of chopped E-glass fibers at the top and the bottom as facesheets. Load, displacement, and strain measurements were recorded every 25,000 cycles up to 2 million cycles. By relating emission that occurs during fatigue loading to the onset of significant damage, the AE technique was used as an additional method comparing load, strain, and displacement. The specimen was designed to fail in the compression zone first. A pattern recognition was employed (loading, unloading, and reloading) to check the felicity effect, which is the significant evidence of fiber reinforced polymer damage. The results showed that the first presence of the felicity effect was at a level higher than the fatigue level, 10 – 44 kN which represent 6 % of the failure load, meaning the fatigue load had not damaged the specimen (Cole et al. 2006). FRPH structures do not have a significant damage during in service loading. In addition to that, the AE data tracked the damage propagation during the static loading that other conventional methods such as strain gauge could not. The AE data indicated the onset of damage was under the loading point interiorly, then, propagated to the surface preceding the failure.

2.12 Localization Technique

There are two methods which depend on the arrival time to determine the source location: time of arrival and zonal method. Time of arrival is a common method of comparing the arrival times of a signal at different sensors in an array. The sensors could be located in linear, triangular, or rectangular arrays depending on the geometry of a material to be

tested. The minimum number of sensors should be two for linear, three for planar, and four for volumetric location. The linear source location is appropriate for a structure that has one long dimension compared to the width or the thickness such as pipes, bars, or truss members, whereas the two-dimensional source location is desired for a plane surface or a curved surface. The second method is called "zonal method". In this method, the first sensor that detects a hit or records a highest output in an array is used as a primary zone to locate the source of the damage and for the next step; an improvement can be achieved by using two highest output sensors. The zonal method is less accurate in identifying the source location than the time of arrival method, but it is more applicable for a large structure with a limited number of sensors or when the material attenuation is too high (Fowler 1988). Source location technique is useful in evaluating a large structure by using appropriate number of sensors, calculating the attenuation, and knowing the different wave modes that travel at different velocities (Surgeon and Wevers 1999).

There has been previous research on various materials using various algorithms to estimate the location of the AE. The AE can be used to locate damage in composite materials (Romhány et al. 2017). The source location in reinforced concrete slabs retrofitted with CFRP strips has been studied using the linear algorithm (Degala et al. 2009). In the case of CFRP strips, the AE signals were found at a region where the debonding initiated between the CFRP strips and the concrete at the anchorage of the strips. In another study, CFRP sheets were used to flexuraly retrofit concrete beams subjected to three-point bending (Yun et al. 2010). Two-dimensional AE source location was used to monitor the onset, growth and location of cracks in the beam. The two-dimensional algorithm successfully located

the damage at the centre of beams, where the CFRP sheet was intentionally not bonded to the concrete surface (Yun et al. 2010). In another study, damage localization has been investigated in fiber reinforced mortar subjected to tension and monitored using the AE technique and digital image correlation using an automated image processing procedures (Rouchier et al. 2013). A camera was set to monitor the notched area in the sample that the microcracks supposed to start in. Most AE signals were recorded in high strain areas, along the crack area.

Estimated velocities have been shown to be dependant on measurement parameters. A study has been conducted to compare the time of arrival and estimated wave velocity at different AE threshold levels in reinforced concrete beams using PLB tests out of the plane and in the plane of the sensors (Md Nor et al. 2013). They concluded that the estimated wave velocity is threshold and distance dependent; the estimated wave velocity decreases as threshold level and distance between sensors increase.

A study on the effect of wave mode on the accuracy of source location determination using AE generated by PLB on a steel plate was performed (Kaphle et al. 2012a). The STFT and WT were used to identify wave modes and determine which type of these wave modes gives more accurate localization of AE sources. This study concluded that using a threshold based method to determine arrival time is a reliable method if the extensional wave mode is used. However, the study concluded that by setting a low threshold to identify the extensional mode in actual application noise may reduce the reliability of the approach (Kaphle et al. 2012a).

A probabilistic framework has also been used to locate AE signals generated from PLBs on an aluminum plate-like structures (Dehghan Niri and Salamone 2012). Continuous wavelet transform was performed to determine the arrival time of the lamb waves. Four piezoelectric sensors were used to capture the AE signals in two different configurations. The difference of using this approach over the conventional two dimensions source location was the considering of uncertainties in the arrival time and wave velocity. The variance in arrival time was used as an uncertainty in arrival time, and the variance in the frequency domain was used as an uncertainty in the group wave velocity. In the next step, extended Kalman filter was used to iteratively predict the location of AE signals and the wave velocity. The results indicated that the proposed two dimensional algorithm can be used in a real time application (Dehghan Niri and Salamone 2012).

Piezoelectric rosette sensors have also been used to improve source location in plates and panels (Matt and Di Scalea 2007). The rosette transducer consists of a rectangular macro-fiber composite which has an ability to extract the flexural wave mode using rosette principles by determining the wave strain principal angle. Source location was determined using PLBs on an aluminum plate, an anisotropic CFRP laminate, and a complex CFRP-honeycomb sandwich panel (Matt and Di Scalea 2007).

Smart aggregates transducers (SAs) have also been used to improve source location in a plain concrete beam subjected to three-point-bending test (Li et al. 2016). The low cost new transducer is embedded in a concrete structure to reduce the errors coming from the AE signals attenuation. SAs can be used as a sensor producing voltage under stress, or can

be used as an actuator producing a stress wave when applying an electric field. The frequency response of the SAs sensor was compared to the frequency respond of the traditional surface mounted AE sensors. The results indicated similar characteristics for both types of sensors. The SAs sensor can be pre-embedded in a large concrete structure (Li et al. 2016).

The accuracy of AE source location generated from a fatigue crack growth in an aerospace aluminium sample has been improved by developing three new methods in determining the time of arrival of an AE signal (Bai et al. 2017). Cross-correlation was used to determine the linear correlation between two signals generated at two sensors. The time of arrival of the signal is determined as a significant change occurred in the cross-correlation series of the time varying correlation function in time domain or continuous wavelet transform (CWT) coefficients in time frequency domain. The third new method was the CWT-based binary map that produce a grey-scale image by normalising the power spectrum and then represent the first non-zero pixel as the arrival time of the signal. The results were compared to the conventional fixed threshold and Akaike Information Criterion (AIC) methods. AIC is a statistical method that find a transition point between noise and coherent signal which was developed by Akaike (Akaike 1974). The results proved that the binary map technique produced the lowest error when it compared to the fixed threshold and AIC methods (Bai et al. 2017).

An improved method of automatic delta T mapping (DTM) technique was used to locate damage in a plate steel and an aerospace aluminium plate samples (Al-Jumaili et al. 2016).

In DTM method, two algorithms were used to improve the accuracy of AE source location. A clustering algorithm was used to determine the highly correlated events, and a minimum difference algorithm was used to locate the AE events. The results showed that the automatic DTM method improved the accuracy, reduced the time of operating, prevented the human errors, and removed the need of expertise to operate the test (Al-Jumaili et al. 2016).

With regards to source location in FRP bars, Chen et al. (1993) estimated an AE source location in aramid FRP plastics subjected to tensile loading. AFRP consists of 65% of aramid fibers and 35% of vinylester resin. The following equation was used in calculating the linear source location:

$$Location = \frac{T_{max} - \Delta T}{2} \times \frac{gauge\ length}{T_{max}} \qquad \ldots\ldots\ldots\ldots\ldots\ldots\ldots\ldots\ldots\ldots \quad (2.9)$$

Where: T_{max} is the maximum time of the travelling wave between the two sensors for AE waves that generated during a preliminary experiment in the elastic stage; ΔT is the difference in time for an AE wave generated from a tension test and captured by the two sensors. The random distribution of damage throughout the length of the failed samples was observed visually and verified using a threshold based linear source location (Chen et al. 1993).

Liang et al. (2004) calculated damage location of a pseudo ductile hybrid, glass and carbon, fiber reinforced polymer rods subjected to tensile loading by using piezoelectric and fiber

optic acoustic emission sensors. Equation 2.9 was used to calculate the linear source location. Results showed that the maximum error between both techniques occurred in the middle section of the bar as shown in Figure 2.10 (Liang et al. 2004).

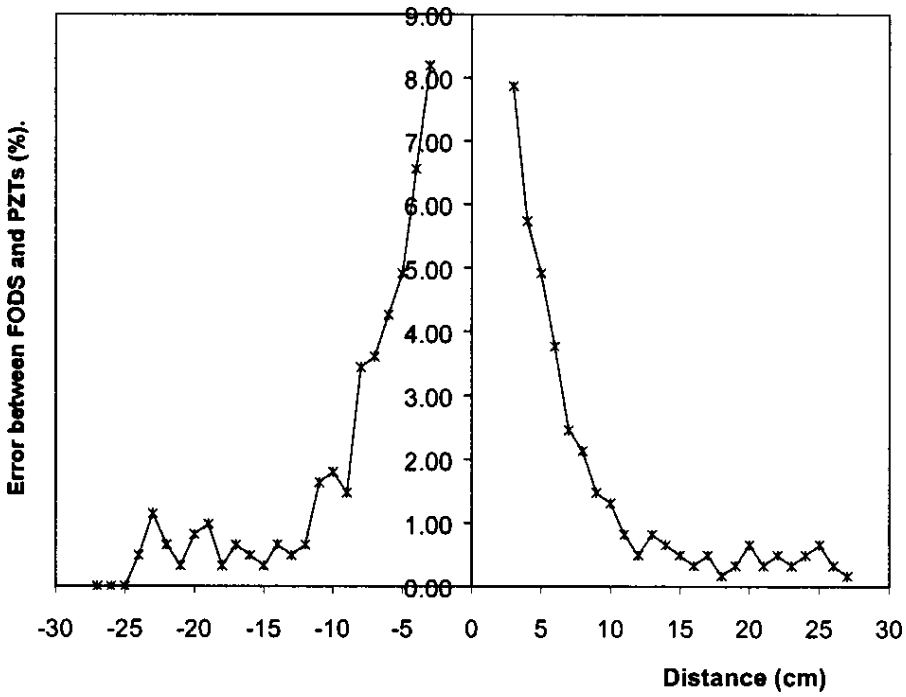

Figure 2. 10 Comparison of the AE source location calculated using the AE signals obtained from fiber optic and piezoelectric sensors (Liang et al. 2004, With permission from ASCE)

In the same study, the spectral energy was calculated for individual AE events at different stages of the loading using fast Fourier transform in time domain analysis in order to distinguish between the fracture of carbon and glass fibers. A damage at the elastic stage was associated to the carbon fiber fracture, while a damage at the ultimate stage during the post-yield phase was associated to the glass fiber fracture. The peak frequency for both fibers was located in a range of 100 – 120 kHz; however, AE signals generated from carbon

fracture have more low frequencies and high amplitude than AE signals generated from the splitting of glass fiber. The results showed that spectral energies of the elastic stage are larger than the spectral energies of the ultimate stage. The cumulative spectral energy plot showed a bilinear relationship that distinguish between the elastic and ultimate stages as shown in Figure 2.11 (Liang et al. 2004).

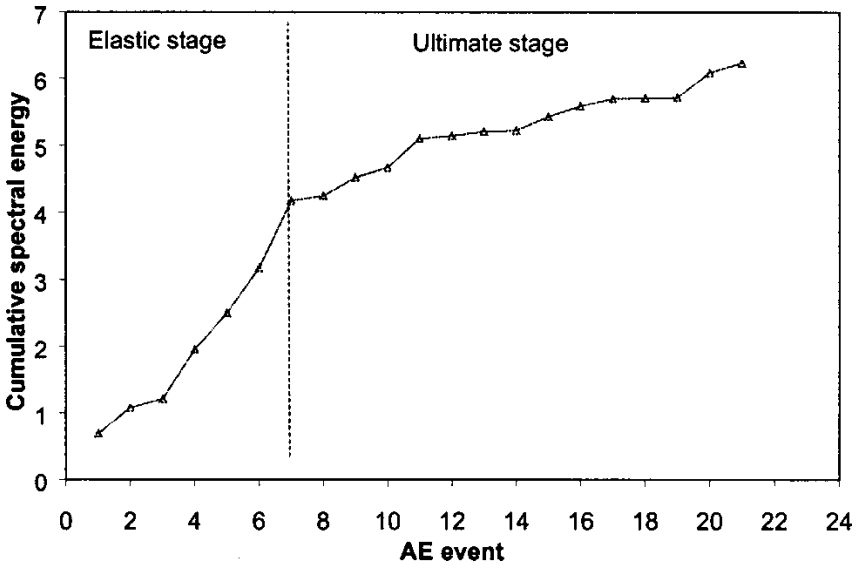

Figure 2.11 Cumulative spectral energy versus AE events (Liang et al. 2004, With permission from ASCE)

Liang et al. (2011) employed the AE technique for investigating the pseduoductility and assessment of damage in post tensioned beams with hybrid carbon glass fiber reinforced polymer HFRP tendons. The tendons were monitored during the post tensioning process, and later during four-point bending testing of the beams. Time of arrival method in time domain was used to locate the fiber splintering along the tendon length at different stages of the loading. The results showed that most of the damage occurred in the middle third

part of the specimen. In addition, spectral energy method was applied using frequency analysis of the AE signal in order to distinguish between the frequency peaks, which were generated from concrete cracking and HFRP splintering. Frequencies that ranged between 92 and 98 kHz which represent concrete cracking was filtered. Also, the results were valuated with the load deflection response of the HFRP beam as shown in Figure 2.12. The figure and test indicate that the fiber damage of the HFRP tendon started at around 75 % of the ultimate load following a significant splintering of the glass fibers in the tendon. Cumulative spectral energy for both carbon and glass fiber were successfully determine the pseudo yield point of the post tensioned beam. The cumulative spectral energy demonstrated a bilinear behaviour confirming that the slope changed at the yielding point (Liang et al. 2011).

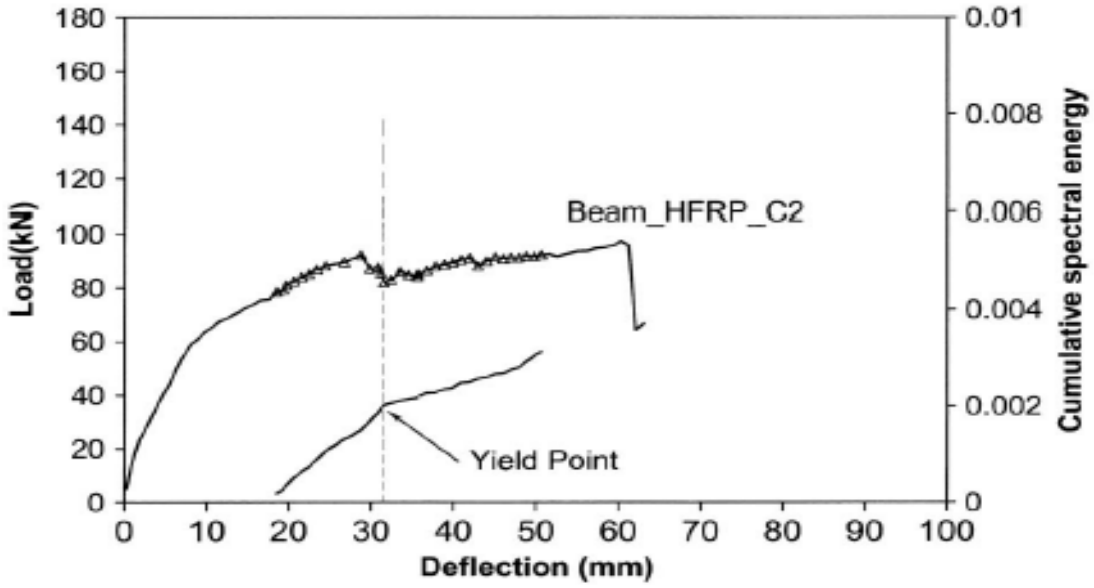

Figure 2.12 Correlation of AE with the load deflection curve and cumulative spectral energy (Liang et al. 2011, With permission from ASCE)

Li et al. (2017) studied the interfacial debonding behaviour between a CFRP bar and concrete samples subjected to pullout tests and monitored using AE technique. Some AE parameters were used to study the response of AE such as cumulative events, amplitude, and peak frequency. The evolution of debonding was correlated successfully with the changes of AE parameters. The results were confirmed using finite element method to analyze the interfacial debonding performance of the CFRP pullout sample (Li et al. 2017)

Artificial neural networks (ANN) have been used to improve AE source location. The ANN method is suited for multidimensional non-linear problems and is a promising approach to reduce the errors due to acoustic anisotropy and multiple modes of wave propagation (Kalafat and Sause 2015). In one study, an ANN localization approach was used in type III carbon-fiber-reinforced polymer pressure vessel with metallic liner (Kalafat and Sause 2015). Two types of test were performed to simulate signals produced by different failure mechanisms: the first test was the pencil lead break (PLB), and the second test used piezoelectric pulser to generate pulses to excite frequency bands above 100 kHz. They performed tests on empty and filled tanks to obtain the different signal path propagation. Two-dimensional source location was carried out using conventional arrival time and ANN methods. The results proved the ability of using the trained neural network from both test sources (PLB and pulser) and applied it to recorded data from a failed material. They concluded that the approach improves the accuracy of the localization of the AE source by a factor of 6, if the velocity and arrival time can be adequately estimated. The ANN source location estimates also showed less scatter in the estimated position compared to the arrival time method by a factor of 11. The researchers suggested that training neural network for

source localization could be improved more by thinking of alternative strategies of calculating the time of arrival or using alternative parameters extracted from AE signals (Kalafat and Sause 2015).

The ANN have also been used to predict the AE source location in a unidirectional carbon fiber reinforced plastic laminate having a high anisotropy ratio (Caprino et al. 2011). Three resonant transducers were attached on the plate surface and PLBs were used to generate AE sources. The difference in time arrival of the waves between the three sensors were measured using threshold method. The time differences between the three sensors, were calculated using a two-dimensional algorithm, and used as input for ANN and later compared using only the time difference between the two sensors. The ANN predicted the source location with a satisfactory accuracy, the mean difference between the actual and the calculated source location was 1.85 mm with a standard deviation of 3.89 mm. They concluded that the accuracy was not improved by increasing the number of inputs from one to two time differences (Caprino et al. 2011).

The ANN has been used to predict factor of delamination in 4 mm GFRP plate subjected to drilling tests and monitored by AE technique (Sudha et al. 2011). Three different ranges of cutting parameters were used to build 36 databases, and four AE parameters were used as inputs: RMS voltage, peak amplitude, AE counts, and energy. The results showed good correlation with the real factor of delamination that obtained from the experiment with a maximum absolute error of 2.75% (Sudha et al. 2011).

The ANN has also been used to predict AE impact source locations in both aluminum and CFRP plate (Fu et al. 2015). A new type of fiber optic acoustic emission sensor was developed to be embedded in the samples as it provides a better detecting of low frequency waves than the commercial piezoelectric transducer. Differences of the arrival time were used for 2D samples as inputs and AE source coordinates as outputs. The results showed that the ANN reduced the nonlinear errors and enhanced the accuracy with a maximum error of 6.3 mm (Fu et al. 2015).

2.13 Micro Computed Tomography (µCT)

A number of techniques have been used to study the microstructure of FRP materials. SEM microscopy has been used to visualize the presence of damage in FRP materials (Balaguru et al. 2008; Elgabbas et al. 2015; Sawpan et al. 2013) However, SEM images only provide information on the specific surface where the sample is cut and that represents a very small fraction of the sample. As a result, a comprehensive understanding of the damage quantification, geometry, and thickness requires the examination of many cross sections of the samples. Recently µCT has been used in as a promising tool to overcome some of these problems through direct observation of damage in three dimensions, without the need for cross sectioning (Awaja et al. 2009, 2011; Awaja and Arhatari 2009; Desplentere et al. 2005; Schell et al. 2006; Schilling et al. 2005).

Using X-ray micro CT (X-µCT) internal damage has been observed in Syntactic foam (hollow glass microspheres in polymeric matrix) subjected to a combined effect of cycling

and increased temperature (Awaja and Arhatari 2009). The 3D reconstructed images showed three types of damage: glass microsphere fracture, enlargement voids, and microcracks in resin due to the thermal stresses. The percentage of damaged glass spheres increased significantly with the evolution of the thermal cycle (Awaja and Arhatari 2009).

Internal and near-surface structure has also been investigated for different epoxy resin composites exposed to accelerated thermal treatment using X-μCT scan and optical coherence tomography (OCT) (Awaja et al. 2009). That work concluded that the percentage of crack volume is a useful method of evaluating the damage of epoxy resin composites. They also concluded that the most cracks were generated as a results of the expanded voids that are originally present during the manufacturing process (Awaja et al. 2009).

Using X-μCT internal damage has been also investigated for E-glass, 3D parabeam, and carbon fiber reinforced epoxy resin composites subjected to accelerated Ultraviolet (UV) degradation condition, and environmental conditions (Awaja et al. 2011). The 3D images showed that most damage occurred in the resin in regions closed to the surface for E-glass and 3D glass, while the damage was in form of internal delamination in the carbon fiber composite (Awaja et al. 2011).

Another study investigated a geometry of fiber bundle and voids in glass fiber reinforced polymer plate using X-μCT (Schell et al. 2006). The results showed that the voids were concentrated randomly near the outlet vent (Schell et al. 2006).

Previous study on woven glass-fiber composites has also been conducted to determine the microstructural variation of different 3D warp-interlaced fabrics architectures (Desplentere et al. 2005). Yarn thickness and width values, and the spacing between the yarns were compared using three techniques: optical micrography for surface scanning, optical microscopy for cross section scanning, and μCT for the internal geometry. Good agreement was obtained between these three imaging techniques (Desplentere et al. 2005).

Microcracking, matrix cracking, and delamination have been investigated in CFRP and GFRP composite laminates using μCT (Schilling et al. 2005). The size, location, and geometry of the voids were studied by three dimensional models for glass fiber tows that appeared as a dark grey, the resin that appeared as a grey, and voids that appeared as white (Schilling et al. 2005).

Both μCT and SEM have proven useful for detection of damage in the form of void within FRP materials, but μCT has better capabilities for quantifying damage.

Due to the uncertainties associated with production of FRP and their linear elastic characteristics, FRP design codes tend to be conservative and therefore costs of FRP reinforced systems maybe higher than necessary (Alampalli and Ettouney 2013; Chiewanichakorn et al. 2012) A better understanding of the detection and progression of internal damage in FRP rebars may aid in refining the limits provided by the codes. Therefore, there is a need to better characterize the microstructural damage evolution and its relationship to more field usable structural health monitoring techniques such as AE.

2.14 Summary

Literature search revealed that FRP composites samples, with different fiber and resin types, as well as different manufacturing methods, have been tested using the AE technique. The evaluation criteria were stated in their research according to the type of the composite materials and their configurations. It was noted that the type of resin, f fiber volume fraction, and the fibers orientation affect the onset of emission.

FRP rebars may develop micro damage during the manufacturing process or under service loads. The micro damage will ultimately affect the durability of the rebar (Mahal 2015). Thus, it is of interest to identify its early damage features, and hence aid in studying the effect of damage on performance of these materials.

The damage detection and localization can be done using NDE techniques such as ultrasonic, radiography, thermography, and acoustic emission. Up to date, there is no technique that can provide a complete quantitative evaluation of a material. Since FRP rebars are a relatively new material, setting standard NDE method to characterize the material is still challenging.

In this research, AE technique was employed for the structural evaluation of GFRP and CFRP rebars under tension. A better understanding of the correlation between the AE and the damage will give a better insight for the failure mechanisms. AE data were correlated

with loading, and the information may be beneficial in setting a data based criterion for monitoring FRP rebars.

The internal micro-structure of the FRP rebars subjected to tensile loading will be investigated using μCT and SEM images. The volume of voids in the samples is monitored throughout the loading process and the increase in void volume will be correlated to the increase in damage. The μCT method maybe useful in determining the structural integrity of the FRP rebars as a result of tensile loading that may play a significant role in determining the long-term durability of the rebars.

CHAPTER 3

EXPERIMENTAL APPARATUS AND PROCEDURES

3.1 Introduction

This chapter describes the test instrumentations and the experimental procedures. In the first section, the AE system, the loading machines for testing the FRP rebars under tension, μCT scan apparatus, SEM apparatus, and the low speed diamond saw for preparing the small samples are described. In the second section, FRP specimens' preparation according to the CSA S806 (2012) is described. In the third section, the AE monitoring and software are presented.

3.2 Experimental Apparatus

3.2.1 AE Apparatus

The equipment that was used to collect acoustic emission signals in this study is MISTRAS (Massively Instrumented Sensor Technology for Received Acoustic Signals), which is manufactured by Physical Acoustic Corporation**.** The main components of MISTRAS are a multi-channel Data translation device (DT9816-S 16 bit with maximum 750 kHz sampling rate for one channel as shown in Figure 3.1.

Figure 3.1 DT9816-S, 16 bit with maximum 750 kHz sampling rate for one channel

Two piezoelectric sensors type R15I-AST, manufactured by MISTRAS, (see Figure 3.2) were used to pick up the AE signals . Each sensor has an integral preamplifier with gain at 40 dB to increase the incoming voltage of the signal for easier transmission and conversion by Analogue to Digital Converter (ADC). The operating frequency range is 80 – 200 kHz. The diameter of the sensor is 29 mm, the height is 31 mm, and the weight is 70 g (MISTRAS 2014).

Figure 3.2 R15I-AST Transducer

3.2.2 Loading Apparatus

Experiments were conducted in the W. R. McQuade Structural Engineering Laboratory at the University of Manitoba.

- Servo-hydraulic testing machine, Instron 300 DX, was used for testing CFRP size 2 and GFRP size 4 bar specimens under increasing tensile loads as shown in Figure 3.3. The maximum capacity of the machine is 300 kN.

- Servo-hydraulic testing machine, Baldwin 600 XHV, was used for testing CFRP size 4 and GFRP size 6 bar specimens under ramping tensile loads as shown in Figure 3.4. The maximum capacity of the machine is 600 kN.

Figure 3.3 Instron 300 DX machine

Figure 3.4 Baldwin 600 XHV machine

3.2.3 µCT Scan Apparatus

SkyScan 1176 micro-CT scanner (Bruker Micro CT, Kontich, Belgium), as shown in Figure 3.5, was used to acquire µCT images at 9 µm resolution with an angular step size of 0.5^{o} . Three scans were acquired at each angular position and averaged.

Figure 3.5 SkyScan 1176 micro-CT scanner

3.2.4 SEM Apparatus

- JEOL JCM-6000 NEOSCOPE II Benchtop Scanning Electron Microscope, as shown in Figure 3.6, with magnifications range (10X-60000X) was used for providing cross section and transverse section images of FRP rebars.

Figure 3.6 JEOL JCM-6000 NEOSCOPE II Benchtop SEM

- FEI Nova Nano SEM 450 equipped with a Field Emission Gun, as shown in Figure 3.7, was used to acquire the backscattered electron images for SEM analysis.

Figure 3.7 FEI Nova Nano SEM 450 apparatus

- EXTEC Labcut 1010 Low Speed Diamond Saw was used for cutting FRP rebar samples for SEM investigation.

3.3 FRP Specimens Preparation

The AE signals were generated from different GFRP and CFRP bar specimens subjected to increasing tensile loads. According to the manufacturer specifications, the CFRP rebar specimens were composed of 27% of epoxy Vinylester based resin and 73% of carbon fibers (Brothers 2011a). Also according to the manufacturer, GFRP rebar specimens were composed of 27% of Vinylester based resin and 73% of glass fibers (Brothers 2011b). The bars chosen for this study are commonly used for reinforcing applications. The two bar diameters, Table 3.1, were chosen to see if bars of smaller and larger diameter have similar

AE characteristics. the method given in Annex B in the CSA S806 (2012) was used to prepare the specimens (CSA 2012) as shown in Figure 3.8. The code requires that the tension force be applied to the samples indirectly to prevent FRP crushing in the anchorage zone. As a result, FRP specimens were anchored into steel pipes with expansive grout that were gripped by the testing machine. Servo-hydraulic load system was used for the tensile loading test as shown in Figure 3.9. Strain gauges with gauge length of six millimetres and resistance of 120 $\Omega \pm 0.3$ % were glued on the surface of each specimen at the centre of the bar after removing the sand coating. A brief description of the FRP types, properties, and their configurations are listed in Table 3.1.

Table 3.1 Summary of FRP test specimens and their loading conditions. (* Tested under displacement control)

Bar Type	**Number of Samples**	**Diameter d (mm)**	**Surface Coating**	**Cross Area* (mm^2)**	**Tensile Strength f_u (MPa)**	**Sample Length (40d) mm**	**Anchor Length (fu × A/350) ≥250 (mm)**	**Loading Rate (kN/m)**
CFRP size 2	7	6	Sand coated	31.67	2241	240	250	0.8*
CFRP size 4	8	13	Sand coated	126.7	2068	520	800	45
GFRP size 4	9	13	Undulation & sand coated	126.7	758	520	300	4*
GFRP size 6	9	19	Undulation & sand coated	285	690	760	600	80

*Cross area was used from the manufacturer data sheet (nominal diameter)

Figure 3.8 Types of GFRP and CFRP samples

3.4 AE Monitoring and Software

R15I-AST sensors were attached firmly to the surface of the anchors by plastic cable ties and a stainless-steel hose clamps. A layer of Proceq couplant gel was used between the sensor and the surface of the anchors to eliminate air gaps, and to ensure good transmission of AE signals to the sensor. Experimental test set up of the AE monitoring system for the tensile load testing is shown in Figure 3.9. The sampling rate was set to 400 k samples/sec. The amplitude threshold for detection of acoustic events was set to 46 dB_{AE}. This level is

approximately ten times the typical observed peak to peak noise amplitude and hence produces only few false triggers under the threshold level. A pencil lead break (PLB) test was performed near the sensor before any AE data recording took place in order to check the sensitivity of the sensor and the functioning of the amplifier and DAQ.

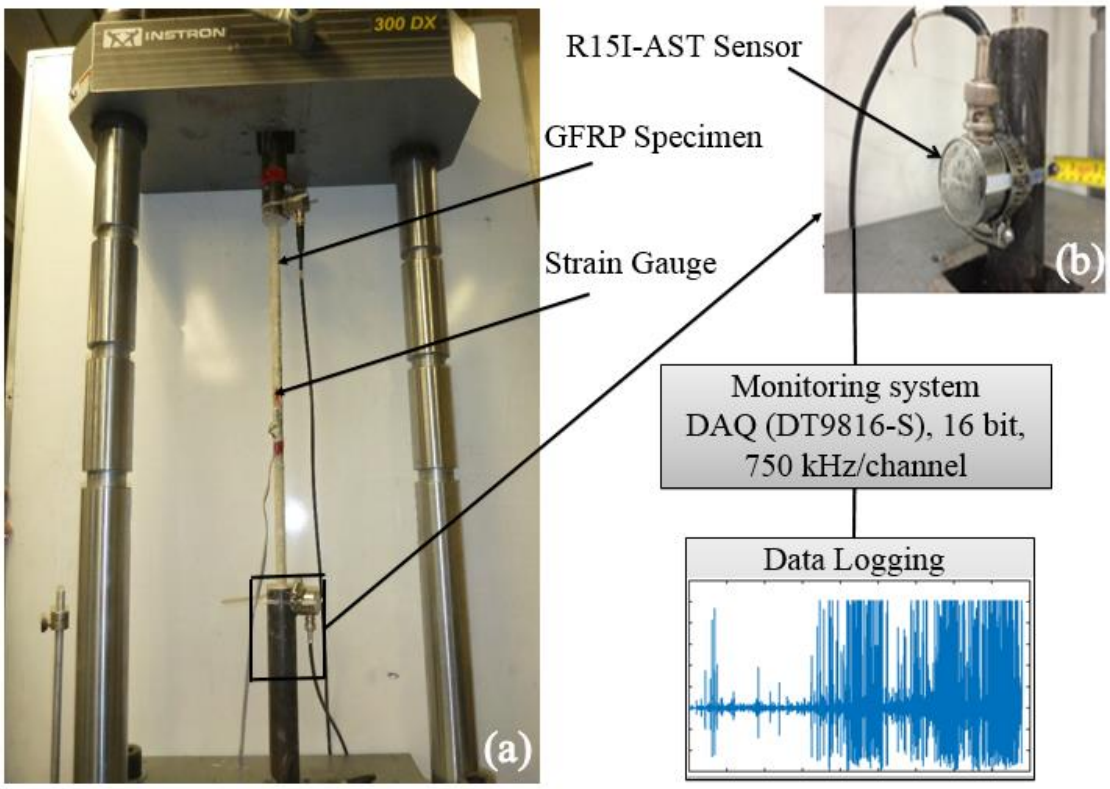

Figure 3.9 AE system set up for the tensile load testing. (a) FRP specimen with anchors in servo-hydraulic load frame (b) Sensor coupled to the anchor using couplant gel

For each type of rebar, one sample was used for PLB measurement of the velocity under load-unload-reload conditions at every 10% of the predicted ultimate load to check the

velocity and modulus of elasticity at each stage, and another sample was used for PLB and tension tests. For each sample type, the predicted ultimate load was estimated by using the average ultimate load from five FRP samples that were tested up to failure. Two 5 cm samples were cut from each diameter of the FRP bars, before loading, to be used as control samples for the μCT scanning. The test samples were subjected to increasing tension until 30 to 98% of the predicted ultimate load was reached. By not testing to failure the disintegration of the sample was prevented so that the samples could be analyzed by μCT.

CHAPTER 4

STUDY OF FRP BARS UNDER TENSION USING ACOUSTIC EMISSION TECHNIQUE

4.1 Introduction

This chapter presents the behaviour of pultruded FRP which have been manufactured using continuous fibers. AE was applied to investigate the fracture of different diameters of CFRP and GFRP bars during tensile loading. A burst AE signal was generated every time material components undergo cracking or fracture. These signals were analyzed to identify their sources, using conventional signal analyses in time domain and time – frequency domain. Amplitude distribution over time, cumulative ratio of the amplitude distribution corresponding to the percentage of the ultimate load, RA (rise time divided by amplitude) and AF (number of counts divided by duration) as a function of time, cumulative counts, amplitude versus duration, and frequency peaks of the acoustic signals were plotted for this purpose. The frequency maxima were determined for different amplitude signals using STFT.

4.2 Typical AE Signals

AE waveforms can be classified using several of the AE parameters that can be related to different stages of the tensile test. Figure 4.1 shows AE signals for CFRP and GFRP that have different amplitudes. For the highest peak amplitude signals, some non-linearity can

be observed. For peak amplitudes exceeding 80 dB_{AE} there is an offset in the signal before and after the AE event that is an artifact of instrumentation. An artifact is an error of representation the information (i.e: the amplifier does not amplify the high amplitude signal properly, and that is called an amplifier saturation). When a small signal amplified, These results overestimate the peak amplitude at the largest signal levels (> 95 dB_{AE}) of up to ~1.6 dB. For peak amplitudes of less than 80 dB_{AE} this offset is not observed. The duration of the AE signals ranges from 27.5 microseconds to several milliseconds.

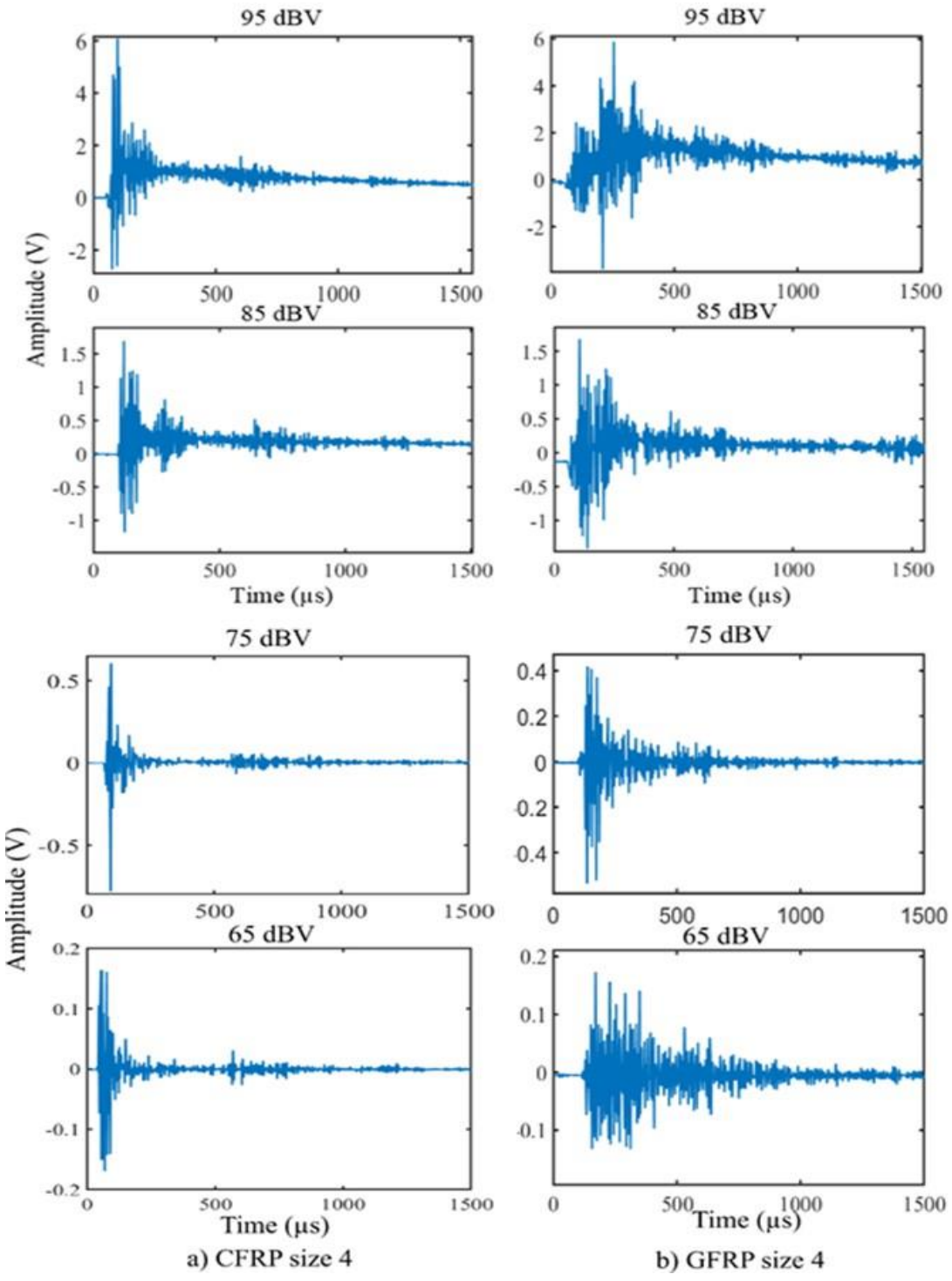

Figure 4.1 Typical unfiltered AE signal at 98, 85, 75, and 65 dB_{AE} for a) CFRP and b) GFRP size 4 (d = 13mm)

4.3 Results and Discussion

4.3.1 AE Signal Analysis in Time domain

The three-part RMS algorithm described in (Shateri et al. 2017) was used to separate one event from another. For each AE event, a number of parameters were measured such as amplitude, duration, number of counts, rise time, peak frequency, and average frequency.

4.3.1.1 Amplitude

Twenty tests in total were carried out on different diameters of CFRP and GFRP reinforcing bars. Each of the tests had similar trends in the AE parameters. Therefore, only typical plots are presented.

Evolution of the peak amplitude of individual AE signals over time is shown in Figure 4.2. In Figure 4.2, each AE event is presented as a single dot on the plot. In total 146 to 811 events per cm^3 were observed in the GFRP size 4 bars, 157 to 792 events per cm^3 in GFRP size 6 bars, 557 to 4578 in the CFRP size 2 bars, and 48 to 604 in the CFRP size 4 bars. The voltage threshold for detection of acoustic events was set at 46 dB_{AE}, and hence there are no events below this threshold. Two interesting observations can be made from Figure 4.2. First, the number of events per unit time increases as strain level increases. The direction of the loading is parallel to the fibers and in past work the low and medium amplitude levels have been attributed to debonding between the fibers and matrix and the

longitudinal microcracks in the matrix (Barré and Benzeggagh 1994; Bhat et al. 1994; Ely and Hill 1995) Fiber breakage was thought to release more energy per event and has been attributed to the higher amplitude AE signals (Bai et al. 2017; Drummond et al. 2007). Second, the number of higher amplitude signal events per unit time also increase with strain levels.

At early stages of the test, CFRP bar specimens had higher amplitude signals than the GFRP specimens. The mean ratio of the high amplitude signals to the low and medium amplitude signals, for the five CFRP specimens, was 4% and 6% for size 2 and 4 respectively. In contrast, the GFRP specimens had a very small fraction of high amplitude events relative to the low and medium amplitude events. The average ratio of the high amplitude signals to the low and medium amplitude signals for five test specimens was 1% for both size 4 and 6 bars.

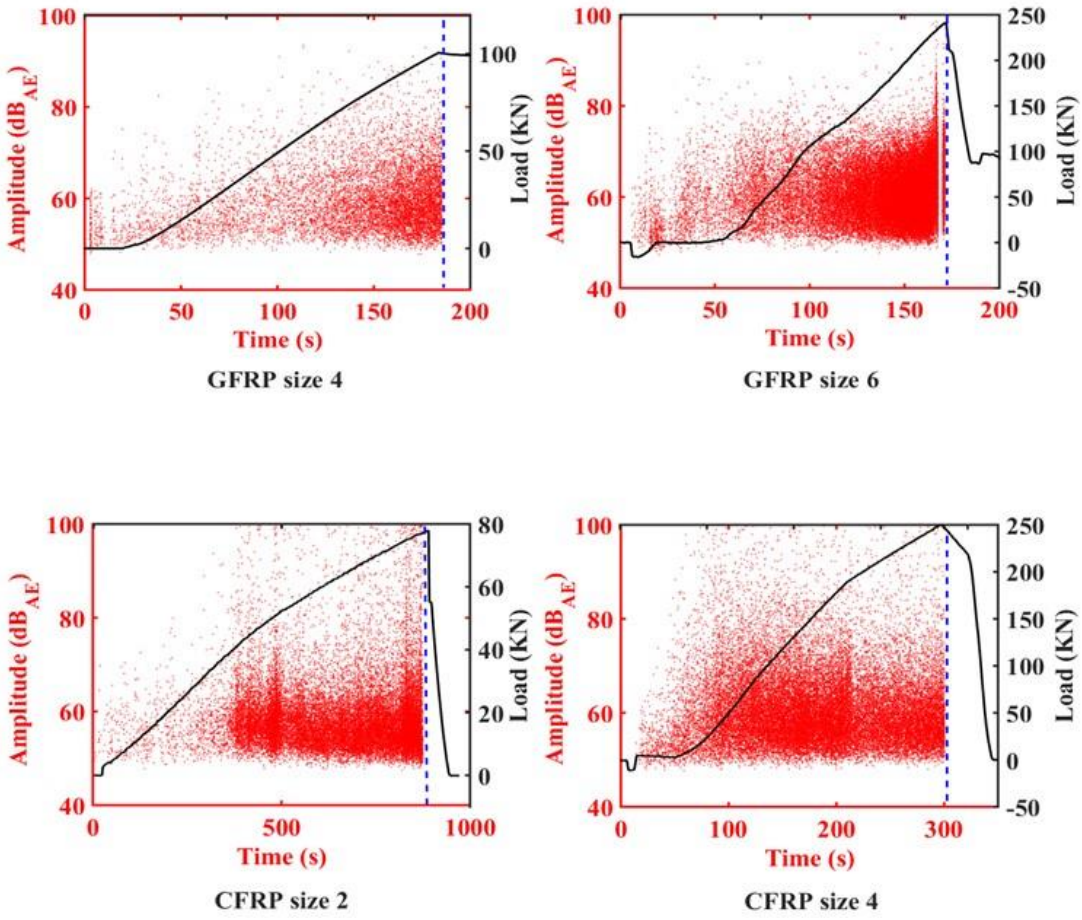

Figure 4.2 Amplitude vs. time with load time superimposed. Dashed line represents time at which failure occurred for CFRP size 2 and GFRP size 6. CFRP size 4 and GFRP size 4 were loaded up to 93% and 95% predicted ultimate load respectively

4.3.1.2 Average Frequency (AF) and RA Value and Cumulative Counts

Average frequency is calculated by dividing the number of counts by the duration, for one hit (Ohtsu 2008). RA value is calculated by dividing the rise time, by the amplitude of the hit (Ohtsu 2008). The rise time is the time interval from the start of a detected hit to the

maximum amplitude of a hit. These parameters have proven useful in linking AE event characteristics to the types of physical damage and damage accumulation (Aggelis 2011; Ohno and Ohtsu 2010). These two parameters have been used to link AE events to the type of cracks in concrete materials, and have been standardized in JCMS-III B5706 for active cracks in concrete (JCMS-III B5706 2003).

In concrete materials, high RA value is an indication of shear cracks, while the low RA value refers to the tensile cracks (Aggelis 2011; Ohno and Ohtsu 2010). In a buried water-pipeline that was located below road, low AF have been attributed to traffic noise (Suzuki and Ohtsu 2005).

Soulioti et al. studied RA and AF parameters of AE signals from concrete containing different percentages of steel fiber under four – point bending (Soulioti et al. 2009). They concluded that the damage mode changed from tensile to shear as fiber content increased in concrete. This resulted in an increasing RA and decreasing AF (Soulioti et al. 2009). In laminated composites, a similar change has been associated with a transition from matrix cracking to delamination (Aggelis et al. 2010; Anastassopoulos and Philippidis 1995).

AF and RA values of AE signals during tensile loading were calculated and plotted as function of time for CFRP bars in Figure 4.3 and for GFRP bars in Figure 4.4. Cumulative counts were also plotted together with stress – strain curves. Most CFRP and GFRP samples were loaded up to failure, while one CFRP size 4 was loaded up to 93 % of the predicted ultimate load and one GFRP size 4 was loaded up to 95 % of the predicted

ultimate load. This saved the specimens from being totally destroyed, so that they could be used later for SEM analysis. Five tests were loaded up to failure and the average of their ultimate loads was taken as the predicted ultimate load. High RA value and low AF were observed at the start of the test, up to 10-20% of the predicted ultimate load as shown in Figures 4.3a, b and 4.4a, b. AE signals of this type have been associated with friction between the machine grips and may also be due to the anchor (Ramirez-Jimenez et al. 2004). After this early region, the AF and RA became relatively steady with some fluctuations. However, the magnitude of these early AE signals was variable in some tests, which had relatively lower initial levels of these signals. As the load increases, there is an increase in the slope of cumulative counts curve (point A) in Figures 4.3c, d that is associated with an increasing rate of internal damage for CFRP bars.

In contrast, GFRP bars show a linear increase of the cumulative counts curve up to 40 % of the predicted ultimate load (point A), as shown in Figure 4.4c, d. As the load increases and reaches the occurrence of an impending brittle failure, an abrupt increase of the slope of the cumulative counts occur. In this stage, RA values start to increase and AF values start to decrease. Some possible reasons for the change in RA and AF with the evolution of the damage have already been discussed in a study of AE signals from concrete in 4-point bending (Aggelis et al. 2011). The AE waves travel through the material in different modes, depending on the source of the damage. For example, some types of damage cause a release of energy that is primarily converted into a longitudinal wave mode (P) of a large amplitude, which is parallel to the wave propagation. This kind of wave travels fast causing a short rise and a small RA value. As the load increases, the wave travels in other wave

modes such as shear waves (S), perpendicular to the wave propagation, or surface waves, mixed of P and S waves, due to scattering of damage in the specimen. These types of waves are slower than the longitudinal waves, which results in a longer rise time and larger RA value.

In the present work, there is also a change in the magnitude of both RA and AF that is correlated with the changes in the slope of the cumulative counts. It can be observed that at the failure of GFRP size 6 or before failure of GFRP size 4 in Figure 4.4a and b, RA decreases and AF increases. This change could be related to the delaminating of the outside layer of the GFRP, which was observed with the naked eye. In contrast, CFRP size 2 shows a continuous increase in RA value as shown in Figure 4.3a, which may be due to some elongation in the matrix that was observed in the longitudinal section sample. This elongation will be shown later in the SEM section. On the other hand, these changes in the RA and AF values were not observed in CFRP size 4 specimen, which were loaded up to 93% of the predicted ultimate load. A longitudinal section of the CFRP size 4 specimen after the load test did not show transverse cracks using SEM observation, which is consistent with the AE observations.

It should be pointed out that the changing of the slope of the cumulative counts as shown in Figures (4.3c, d) and (4.4c, d) is not mimicked in the stress versus strain graph. A summary of these results is shown in Table (4.1) for both CFRP and GFRP specimens.

Table 4.1 AE Signal Parameters for CFRP and GFRP specimens

	Point on the Cumulative Counts Curve	RA* Value Range* (μs/V)	AF* Value Range (kHz)	Strain* Range (%)	Load* Range (kN)	Percentage of the Predicted Ultimate Load Range (%)
CFRP size 2	A	952-1366	48-60	0.67-1.04	32-45	44-55
	B	810-1588	29-64	0.90-1.15	29-64	60-72
	C	1200-1560	26-60	1.10-2.10	71-87	75-96
	D	2589-8557	31-60	1.24-2.20	72-87	92-100
CFRP size 4	A	1389-2823	58-85	0.15-0.24	15-59	5-22
	B	1140-1756	68-100	0.55-0.93	126-188	47-70
	C	835-1077	81-83	1.33-1.51	250-290	93-100
GFRP size 4	A	465-1378	58-75	0.93-1.00	44-58	42-50
	B	741-1256	51-83	1.68-1.96	99-117	90-100
GFRP size 6	A	787-1890	70-80	0.54-0.85	96-142	40-62
	B	1047-2271	50-92	1.19-1.92	216-241	92-100

* RA, AF, Strain, and Load are the values at the change of the slope of the cumulative counts curve
* Range indicate the results of five FRP sample tests for each type.

In conclusion, the slope of the cumulative counts increases with increasing load. However, the absolute number of events at failure varies considerably from specimen to specimen, and by itself is not reliable predictor of failure.

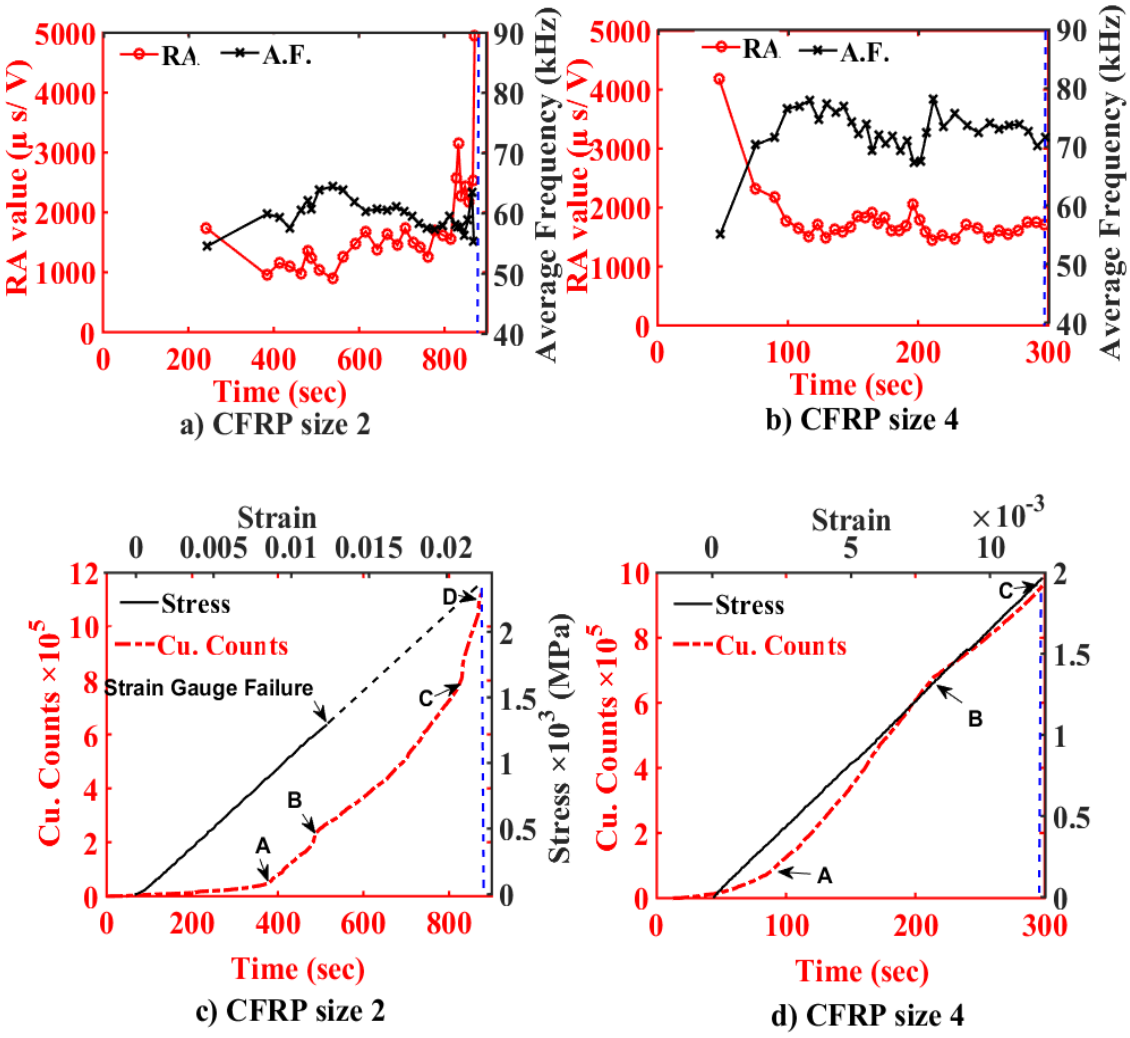

Figure 4.3 Variation of AF and RA values. Cumulative counts vs. time with stress-strain superimposed. Dashed line represents time at which failure occurred for CFRP size 2. CFRP size 4 was loaded up to 93% of the predicted ultimate load

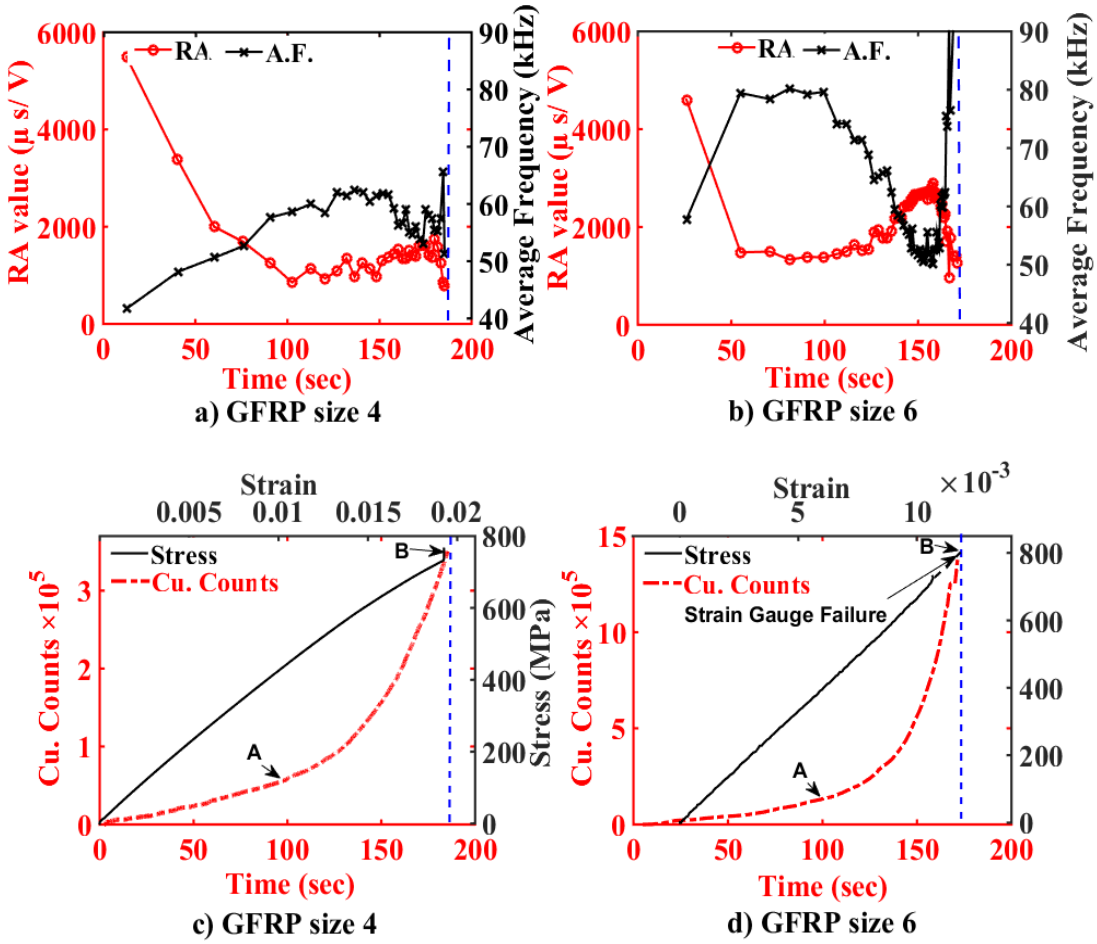

Figure 4.4 Variation of AF and RA values. Cumulative counts vs. time with stress-strain superimposed. Dashed line represents time at which failure occurred for GFRP size 6. GFRP size 4 was loaded up to 95% of the predicted ultimate load

4.3.1.3 Amplitude – Duration

The amplitude and duration of the AE events has been used to check the quality of the recorded data and to correlate with the type of damage mechanism (CARP 1999). Research on short glass fiber composites has been conducted for linking damage identification to the

amplitude and duration parameters (Nguyen et al. 2005). The results showed that increases in the average magnitude of these parameters is an indication of damage evolution during loading (Nguyen et al. 2005).

In this study, the duration of each AE signal for one specimen was plotted in Figure 4.5, as a function of amplitude for the three stages that were determined in Table 4.1. Based on the evaluation criteria in (CARP 1987), events with high amplitude and long duration were attributed to fiber breakage. Low to medium amplitude events with low to medium duration were attributed to matrix cracking (CARP 1987). Similar results were also observed in studies on composite laminates (Gudmundson and Johnson 2000) and GFRP bridge deck panels (Gostautas et al. 2005).

Figure 4.5 plots the duration of AE signal versus its amplitude. The results in Figure 4.5 are clustered in a well banded area, with very few outliers outside the banded area. Previous research correlated these outlier events as unwanted signals that could be either due to Electromagnetic interference, Mechanical rubbing (MR), or overlapping events (OE) (Fowler et al. 1989). The data presented in Figure 4.5 indicates few of these unwanted events. Considering the scarcity of the unwanted events, the testing setup was satisfactory.

Pattern recognition techniques have proven valuable for AE signals classification (Godin et al. 2005; Ono and Huang 1994) In the present work, a k-means algorithm (Arthur and Vassilvitskii 2007) was used to classify the AE signals. In this case, the k-means algorithm used five parameters in time domain as the input data. The parameters used were peak

amplitude, duration, counts, energy, and rise time as described in Figure 2.3. The algorithm classifies the input data depending on a predefined number of clusters, which was set to three to match the expected types of damage. The types of damage will be discussed in the SEM section later in this paper. The principle of this method is to minimize the sum of the squared distance between the assigned cluster and its center. After that, the cluster vector and its centroid are iteratively actualised until the centroid is fixed. The classification was replicated five times each time with randomly assigned initial conditions.

Based on previous published articles (Fowler et al. 1989) and the experimental data, most likely cluster 1 corresponds to debonding, cluster 2 corresponds to fiber breakage, and cluster 3 corresponds to matrix cracking. Also, the figure shows that these three clusters were observed in all three stages of the test. It should be noted that some signal misclassification could be due to the signal attenuation from the source to the sensor. Attenuation will result in amplitude and duration reduction, so an event that is classified as matrix cracking or debonding could have originally been due to fiber breakage mode.

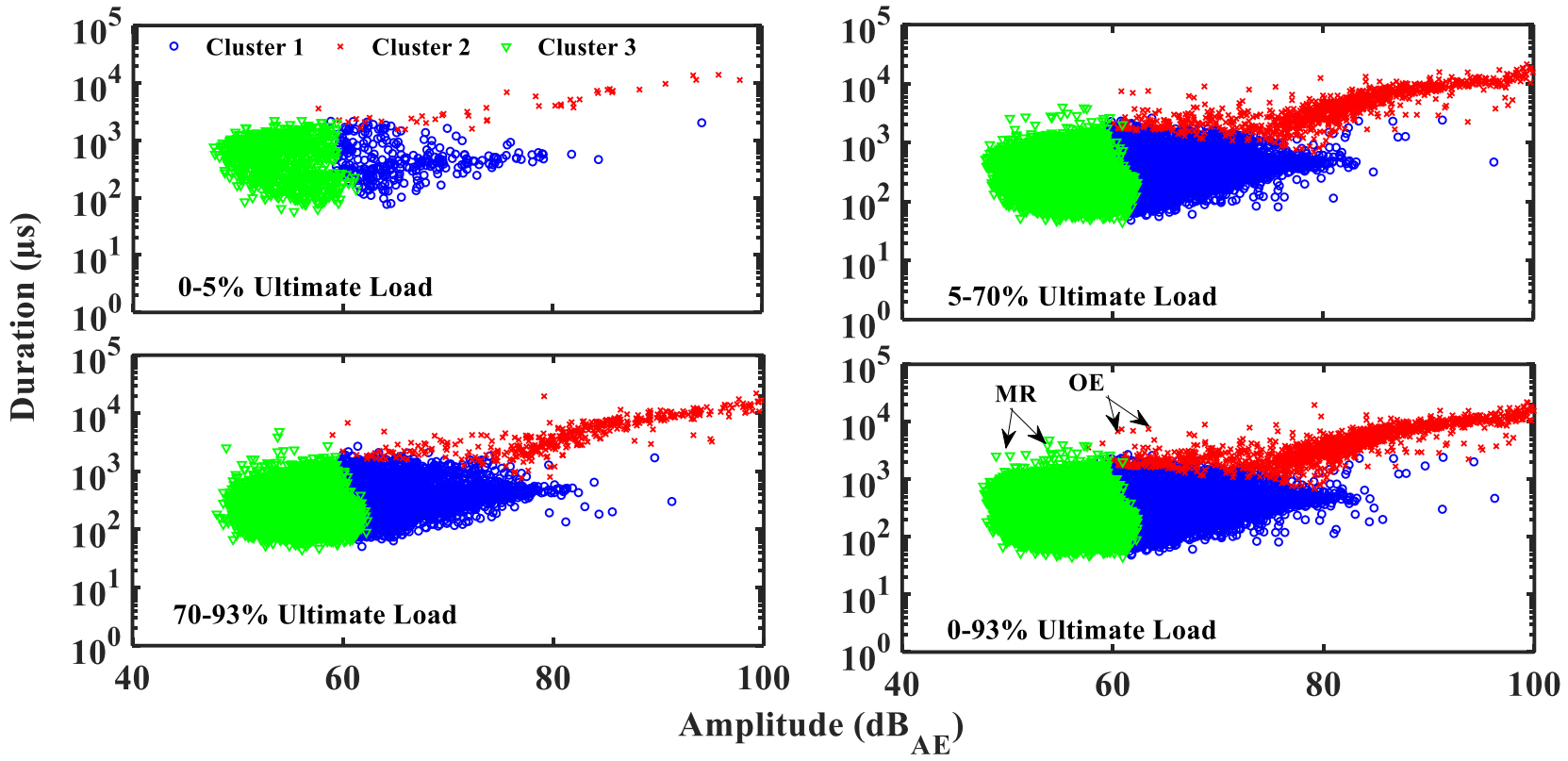

Figure 4.5 Duration vs. Amplitude for three stages in CFRP size 4 specimen. Duration is the time of a signal from the first point exceeding the threshold level to the last one. MR: mechanical rubbing; OE: overlapping events; cluster 1: deboning; cluster 2: fiber breakage; cluster 3: matrix cracking

It can be concluded from Figure 4.5 that the peak amplitude is correlated with the duration, and that larger amplitude signals tend to also be of longer duration. This may in part be due to the duration from the first to the last threshold crossing being longer for higher-amplitude events, simply because higher-amplitude events will take more cycles to ring down. The number of AE signals within the various amplitude ranges were investigated in CFRP and GFRP specimens. The mean of AE features, such as duration and rise time, for each range were calculated for the three stages described in Table 4.1. The results showed that the CFRP signals have a mean duration and mean rise time that are less than GFRP signals at the start of the test, but they are larger as the load increases after about 40% of the predicted ultimate load.

4.3.2 AE signal Analysis in Time – Frequency Domain

Time – varying signals were analyzed in terms of time – frequency domain using STFT to determine the frequency magnitudes that were predominant during the tension test. AE signals that were generated during the test are associated with the magnitude of the released strain energy. Accordingly, these AE signals have specific characteristics due to their amplitude, duration, and frequency content that could be related to a specific damage mechanism (Yang et al. 2009). The nonstationary nature of the AE signal limits the choice of the time window length for STFT; therefore, for acceptable spectral resolution the length of window should be at least the same size as is the longest signal duration. In the current study, a signal was divided into sections of length of 128 samples with overlapping of 120 samples using Hamming windows, and the spectrum was evaluated at 129 frequencies

according to (Mathworks 2009). This leads to a 20 μs time window length. In the time – frequency plot, energy in the signal is represented by calculating the squared coefficient of STFT matrix in MATLAB. STFT was performed on different AE signal amplitudes, and then energy distribution is calculated using the formula in equation 2.8, and plotted in Figure 4.6 as a function of frequency content. In fact, the 80 – 200 kHz resonant sensor could limit the results of the frequency ranges. Most of the energy lies in the range of 125 – 180 kHz in CFRP with some small peaks between 80 and 125 kHz. While they are distributed in almost all frequency ranges for GFRP for 98 dB_{AE} signal amplitude which indicate that several types of damage could be occurring simultaneously. For example, a fiber breakage is more likely to be accompanied with other kinds of damage such as fiber pull out or the movement of the fiber. For 85 dB_{AE} signal amplitude, the peak frequency is about 136 kHz for CFRP, while the frequencies are distributed equally between 110 and 160 kHz for GFRP. For 75 dB_{AE} signal amplitude, the energy lies in the frequency range of 150 – 180 kHz for CFRP, and is distributed equally between 80 – 200 kHz in GFRP.A similar pattern can be seen in the 65 dB_{AE} signal.

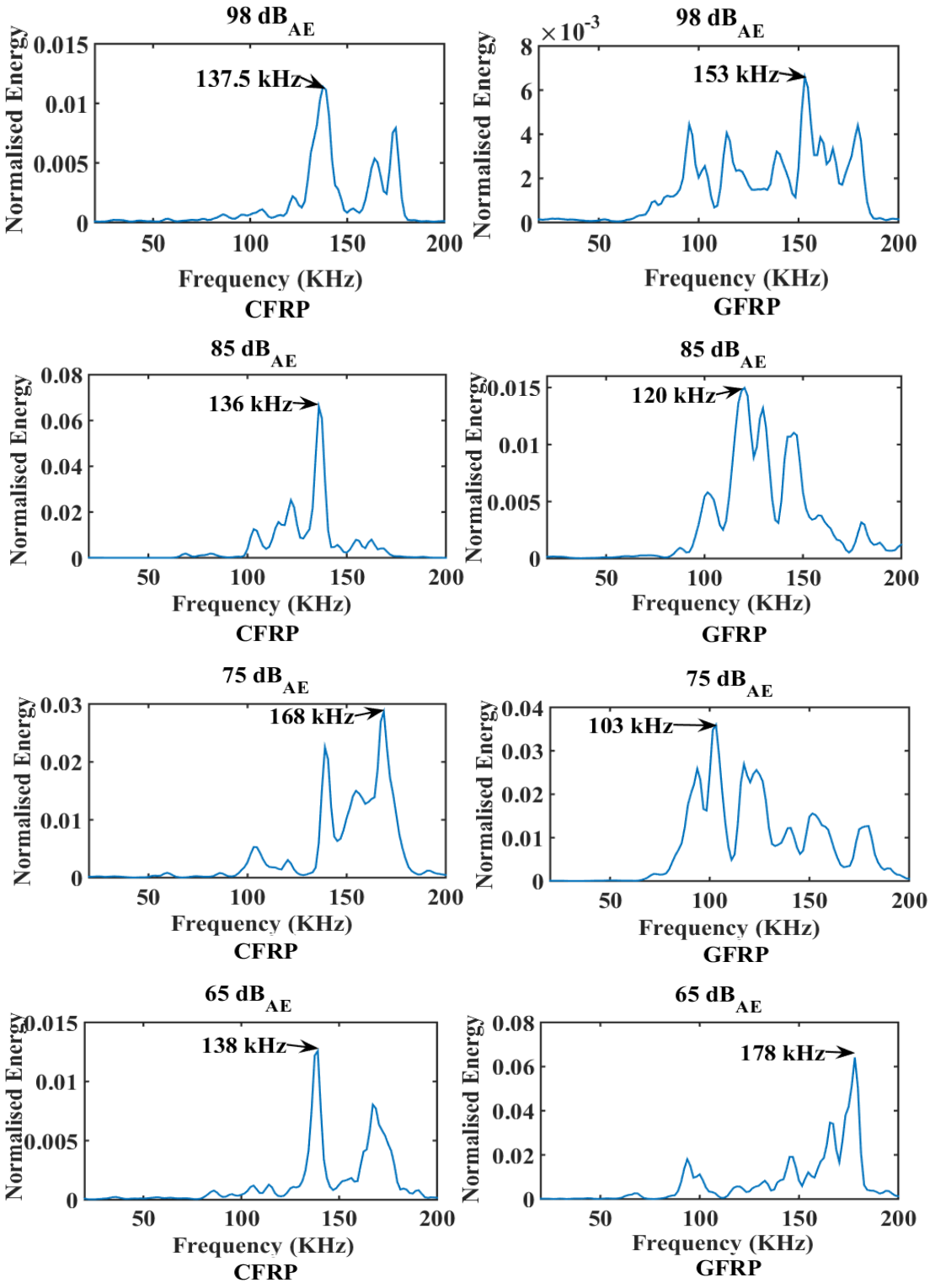

Figure 4.6 Energy distribution versus frequency content for various signal amplitude for CFRP and GFRP size 4 bar specimens

4.4 SEM Observation

Scanning electron microscopy (SEM) identified damage mechanisms in continuous unidirectional GFRP composites and has been correlated to AE signals by using different span to depth ratio samples subjected to testing in three-point bending (Siegmann and Kander 1992). Another study has been used SEM to observe damage mechanisms of different glass/polypropylene plate samples subjected to tensile loads (Ramirez-Jimenez et al. 2004). Different fiber orientations were used in the study: 0^o, $\pm 45^o$, 90^0, $(0\text{-}90^o)$ for each sample (Ramirez-Jimenez et al. 2004). Previous studies have not addressed AE correlation with SEM on FRP bars. The work presented in this paper will use SEM to compare microstructure of FRP pultruded bars before testing and at failure to aid in identifying the origin of AE signals recorded during load tests.

Typically, no damage is visible in the FRP bars to the naked eye until failure and therefore SEM analysis was used for microstructural examination. Transverse and longitudinal sections were cut from each bar before and after testing. Clean and flat sections were prepared using the following procedures: the samples were mounted into epoxy to prevent surface damage during the cutting process, and then a slow speed diamond saw was used to cut them. After that, the sections were polished to remove marks generated during the cutting process, and to get a smooth surface for imaging. The polishing started with 40 and 30 μm silicon carbide sand paper, followed by 5 and 1 μm alumina slurry with a nylon cloth. The polished sections were cleaned using ultrasound bath with ethanol, and then coated with gold palladium.

Figure 4.7 shows the SEM images of both CFRP and GFRP rebar samples. The micrographs were acquired in the secondary and backscattered electrons modes at an accelerating voltage of 15 kV and magnification range of 100x – 600x. After loading CFRP size 2 to failure and GFRP size 4 to 95% of the predicted ultimate load, three types of damage were observed in the longitudinal sections; matrix cracking that developed longitudinally parallel to the fiber direction, debonding, and fiber fracture. On the other hand, no transverse matrix cracking was observed in the cross-section sample; only enlargement of the original voids was detected. In the CFRP size 2 sample, the longitudinal section showed misalignment of fibers, which indicated damage in the matrix. In general, modulus of elasticity of fibers is higher than the one for matrix; therefore, some fibers were fractured throughout the specimens with increasing load. Most of the fracture occurred due to splitting of the outside layer of the bars at failure as shown in Figure 4.7h. It can be concluded from these observations that the damage tends to start near the voids. The voids concentration was higher in the outside layer leading to the damage propagation in this layer at loads closer to failure.

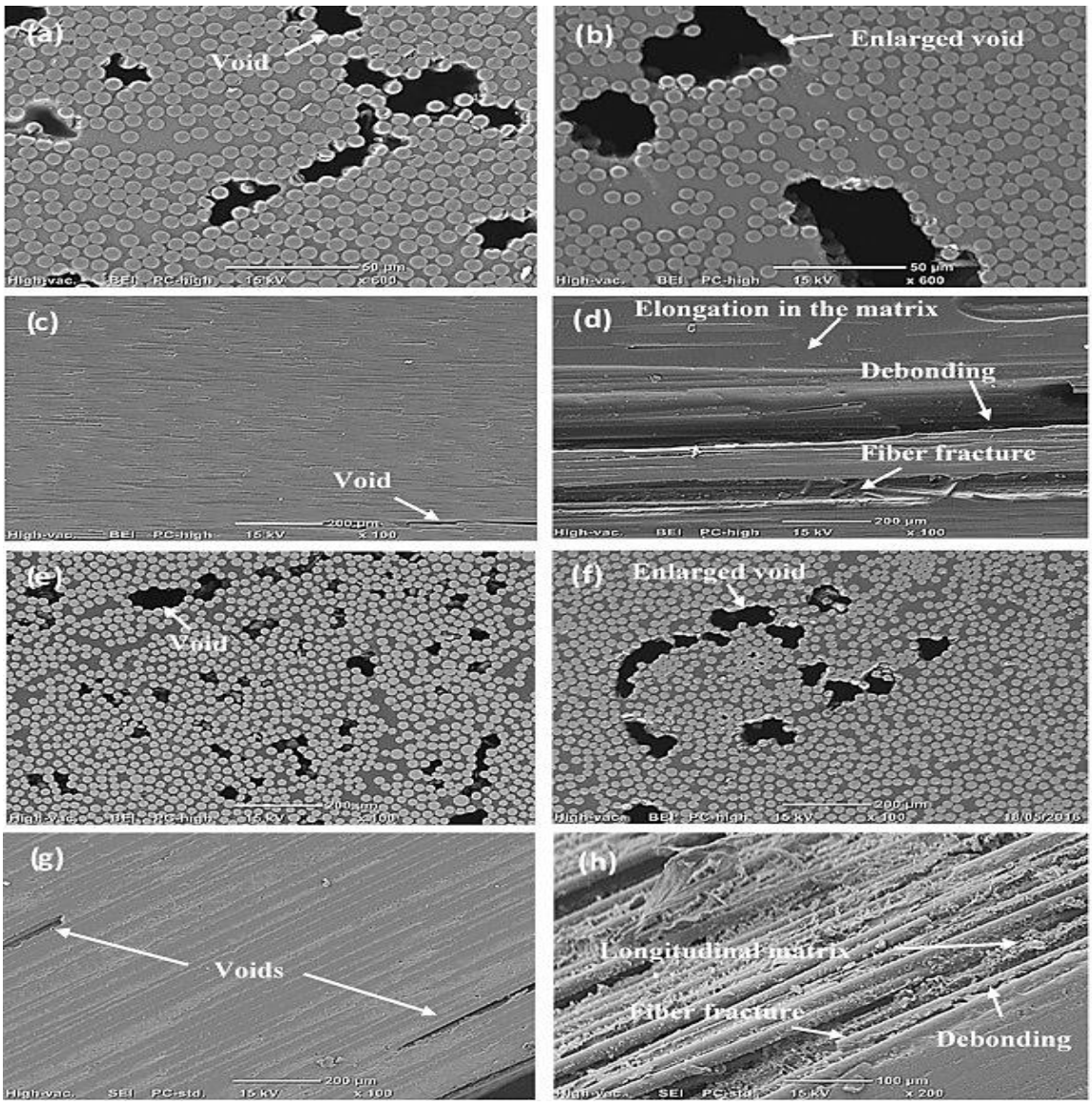

Figure 4.7 SEM micrograph for untested and tested CFRP size 2 and GFRP size 4 bar specimens. a) Cross section for untested CFRP size 2 specimen; b) Cross section for tested CFRP size 2 specimen until failure; c) Longitudinal section for untested CFRP size 2 specimen; d) Longitudinal section for tested CFRP size 2 specimen until failure; e) Cross section for untested GFRP size 4 specimen; f) Cross section for tested GFRP size 4 specimen until failure; g) Longitudinal section for untested GFRP size 4 specimen; h) Longitudinal section for tested GFRP size 4 specimen until failure

CHAPTER 5

COMPARISON BETWEEN MICROSTRUCTURAL ANALYSIS OF GFRP AND CFRP REBARS USING MICRO COMPUTED TOMOGRAPHY (µCT), SCANNING ELECTRON MICROSCOPE (SEM) AND ACOUSTIC EMISSION (AE) TECHNIQUES

5.1 Introduction

In this chapter, different FRP bars were subjected to tension at different percentage of ultimate load. The internal micro-structure of the loaded FRP bars was investigated using µCT and SEM techniques. 3D and 2D images were used to quantify the internal voids, that were entrapped during the manufacturing process, and their distribution. In this work the void volume was used as a measure of damage. AE technique was also employed to study the internal damage progression in the same FRP samples. Characteristics of the AE signals were correlated with the µCT and SEM analyses. This work could be used to improve the safety of workers in precast plants by providing an early warning of failure during the pretensioning of FRP prestressed components.

5.2 Scanning Electron Microscopy (SEM)

The nature of FRPs' microstructure and their micro damage were assessed using SEM cross-sectional analysis.

5.2.1 Image Acquisition

FEI Nova Nano SEM 450 equipped with a Field Emission Gun was used. SEM images were acquired in the Backscattered Electron mode at an accelerating voltage of 15 kV. FEI Maps 2.0 software was used for creating the montages with resolution of 768x512 pixels for each tile in a dwell time of 10μs per pixel.

5.2.2 Image Analysis

SEM Image analysis was performed using MATLAB using the following steps:

1) The montage image is loaded and saved in a matrix.

2) The image is converted to grayscale.

3) The region of interest (ROI) is chosen using ellipse mask.

4) The ellipse mask is applied to the original image.

5) Set a threshold by finding the index of the voids and equated to zero, and everything higher than the index value of the voids are converted to white (index of 255).

6) The image now has only two index values (0 and 255).

By calculating the area of voids (number of black pixels), the area of the cross section in the ROI without voids (number of white pixels) and the area of the total cross section (all pixels in the ROI), the percentage of the voids to the total area can be determined.

5.3. Micro Computed Tomography (µCT)

5.3.1. Image Acquisition

X-ray micro-CT scan were obtained using a SkyScan 1176 micro-CT scanner (Bruker Micro CT, Kontich, Belgium). The system contains an X-ray micro-focus tube operating at a maximum source voltage of 90 kV within a maximum power of 25 W and source current of 278 uA (SkyScan1176 2011). Images were acquired at 9 µm resolution with an angular step size of 0.5^{o} to provide a view from different angles which were gathered by the detector. Three scans were acquired at each angular position and averaged. Depending upon the density of the material, the conditions were used in the three scans is described in the table below:

Table 5.1 Parameters of the µCT scan images in the different three scans

Source Voltage (kV)	Source Current (uA)	Filter	Exposure Time (ms)	Object to Source Distance (mm)	Camera to Source Distance (mm)
40	600	No Filter	800	118.163	165.226
50	500	Al 0.5mm	125	118.163	165.226
90	278	Cu 0.1mm	1700	118.163	165.226

2D Images were reconstructed using NRecon (Bruker Micro CT, Kontich, Belgium). The X-ray beam contains different ranges of energy from soft to hard. The soft X-rays are absorbed at the surface while the hard ones pass through the sample. The preferential absorption of soft X-rays at the FRP sample surface yields an artifact in the form of a bright ring at the sample surface. A filter was applied to remove this effect. However, some relatively soft X-rays are still in the beam. Thus, a beam hardening correction of 35% was applied to the data during reconstruction to correct the presence of these soft x-rays. In addition, ring artifacts can occur when a pixel in the detector is responding either more or less than it should to a given X-ray intensity. Therefore, a ring artefact reduction factor of 7 was applied to reduce such artifacts. A ring artefact reduction factor of 7 is quite low, indicating that the CT detector is performing well. These 2D reconstructed images were stacked to generate a three-dimensional (3D) image.

X- Ray is sensitive to the density of the sample which is represented as differences in X-ray attenuation of materials (Stock 1999, 2008) This feature is useful to utilize the microcracks, voids, and fractures in inhomogeneous materials such as FRP composites where there is a variety in densities. In this study, the damage volume which refers to the volume of cracks and voids represent a gap in the densities and that provide a good contrast in the 3D image reconstructed by CT scan. The micro structure of different diameter of GFRP and CFRP rebar specimens at different loading stages were investigated using a series of 1000 slices of a sample, equal to 9.8 mm. Figure 5.1 shows an example of images obtained from CFRP size 2 sample tested up to 50% of the ultimate load using SEM and μCT scan techniques. This sample was first analyzed using μCT scan techniques and then

cut and analyzed using SEM techniques. The image plane in µCT scan was aligned as closely as possible to the SEM cross-section. There are many features shared between the two images and the correlation between the SEM and µCT images is very high. The voids in the SEM are also observed in the µCT image.

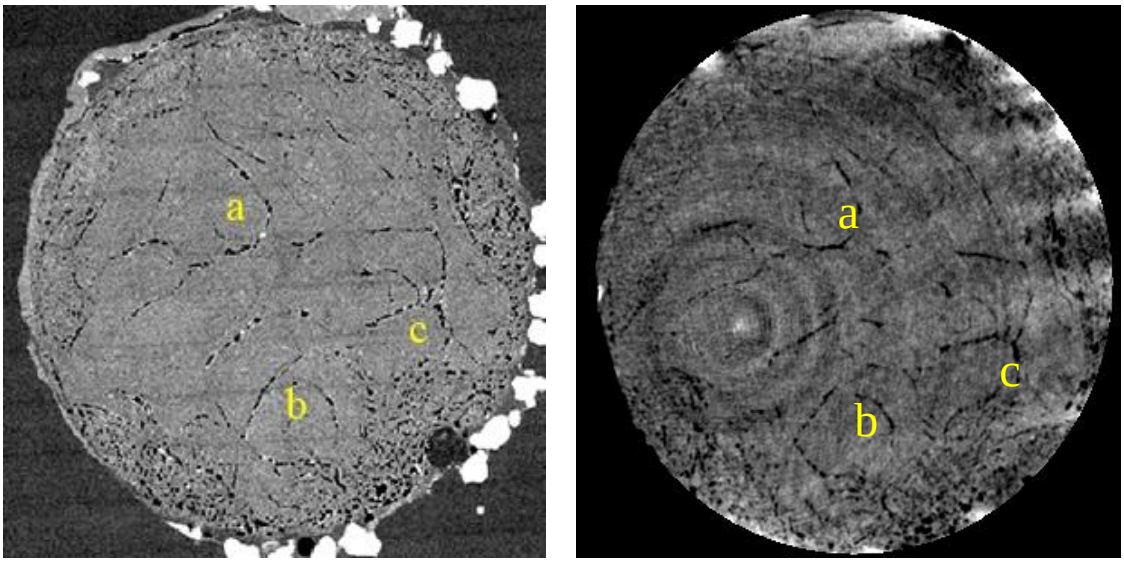

Cross section image using SEM Reconstructed cross section using µCT scan

Figure 5.1 Microstructure of CFRP size 2 tested up to 50% of the ultimate load. Letters a, b, and c refer to the features that can observed in both images

5.3.2. Image Analysis

μCT Image analysis was performed using CTAn software version 1.11.10

5.3.2.1. Threshold Determination

The choice of the threshold value, for the binarization of greyscale images, affects the determination of the damage percentages dramatically. The voids and cracks can be detected from the cross section of the reconstructed image as they represent the black area; however, the manually choice of threshold level especially for samples that represent different lower and upper values of the grey levels could fail or lead to biases. Accordingly, the threshold level is determined by using the equation below to get the same conditions for all samples:

$$Th = m - 2\sigma \quad \ldots\ldots\ldots\ldots\ldots\ldots\ldots\ldots\ldots\ldots\ldots\ldots\ldots\ldots\ldots\ldots\ldots\ldots \quad (5.1)$$

Where Th is the threshold level for a given data, and it depends on the distribution of the brightness value; m is the mean brightness within the binary threshold selection, and; σ is the standard deviation. The binary threshold was selected between the lower and upper limit of the brightness values which was chosen by comparing the reconstructed image by the binary selection as shown in Figure 5.2.

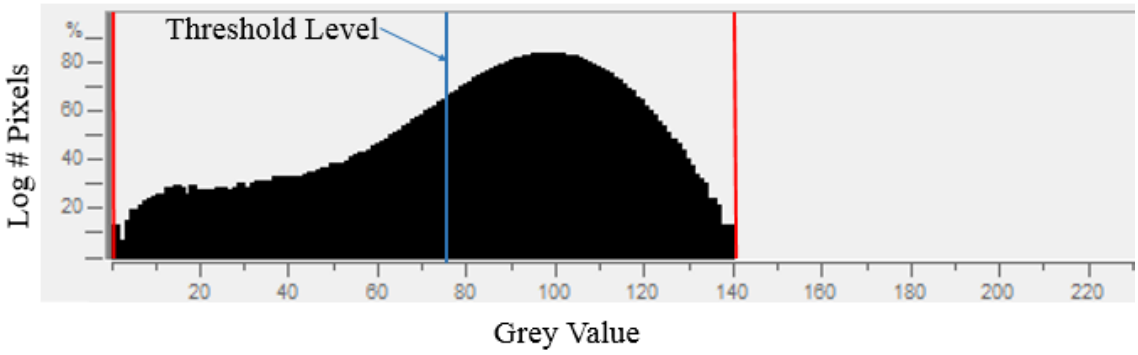

Figure 5.2 Pixel histogram and binary selection for GFRP size 4 rebar sample. Red lines represent the minimum and maximum limit of the binary selection

5.3.2.2. Analysis Procedures

The analysis procedures are summarized in Figure 5.3 and outlined as follows:

1) For each sample, a series of 1000 cross-sections from the reconstructed µCT images were collected, Figure 5.3a. The chosen region was indicated by the double red arrows.

2) A region of interest (ROI) Fig. 5.3b is used to crop all the cross-sections and the resulting images, Figure 5.3c, are saved into a new file.

3) Using a threshold, the saved images are converted into binary images. White pixels represent the solid phase such as the resin and fibers, while black pixels represent the voids, Figure 5.3d.

4) A shrink wrap operation on the ROI is used to eliminate regions that are outside of the sample (Bruker 2013), Figure 5.3e.

5) Bitwise operation plug-in is used to mask the currently loaded image using the ROI, Figure 5.3f.

6) The despeckle plug-in is used to remove all voids from ROI, Figure 5.3g.

7) Voids which are connected to the boundary of the ROI are closed using a morphological operation plug-in. As a result, these closed voids are included in the analysis (Bruker 2013), Figure 5.3h.

8) Within the ROI the image is inverted, so that the voids become binary positive and appear white in the image, Figure 5.3i.

9) 2D analysis, 3D analysis, and 3D model are performed as final steps, Figure 5.3j.

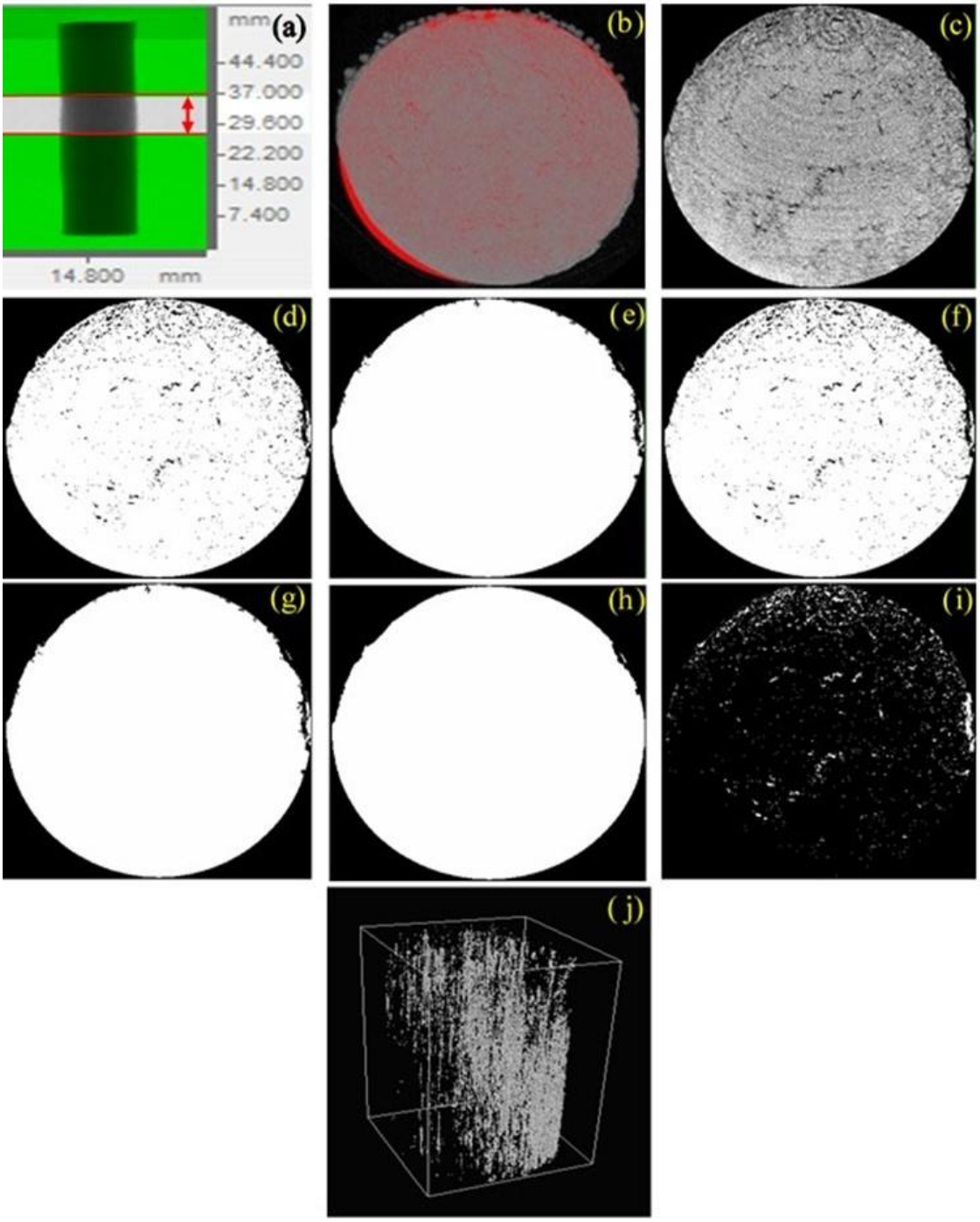

Figure 5.3 Sequence of images in the image analysis methodology using CTAn, CTvox, and CTvol

5.4 Results and Discussion from µCT Scan

For each sample, a 9.8 mm section was selected from approximately the center of the rebar for the analysis.

5.4.1 3D Analysis and Image Visualization

Using CTAn the image processing outlined in Figure 5.3 was carried out on the µCT image stack from each sample. The CTAn also estimated the void fraction and thickness distribution for each sample. For the three-dimensional visualization of the voids the CTvol software was used (Skyscan 2008). An example of a 3D image of GFRP size 4 sample is illustrated in Figure 5.4. Figure 5.4b shows the distribution of the voids for the control sample, while Figure 5.4c shows the distribution of the voids and cracks in the sample as a result of a tensile loading up to 95% of the ultimate load. It shows that the damage is concentrated near the location of the voids that were present in the untested sample.

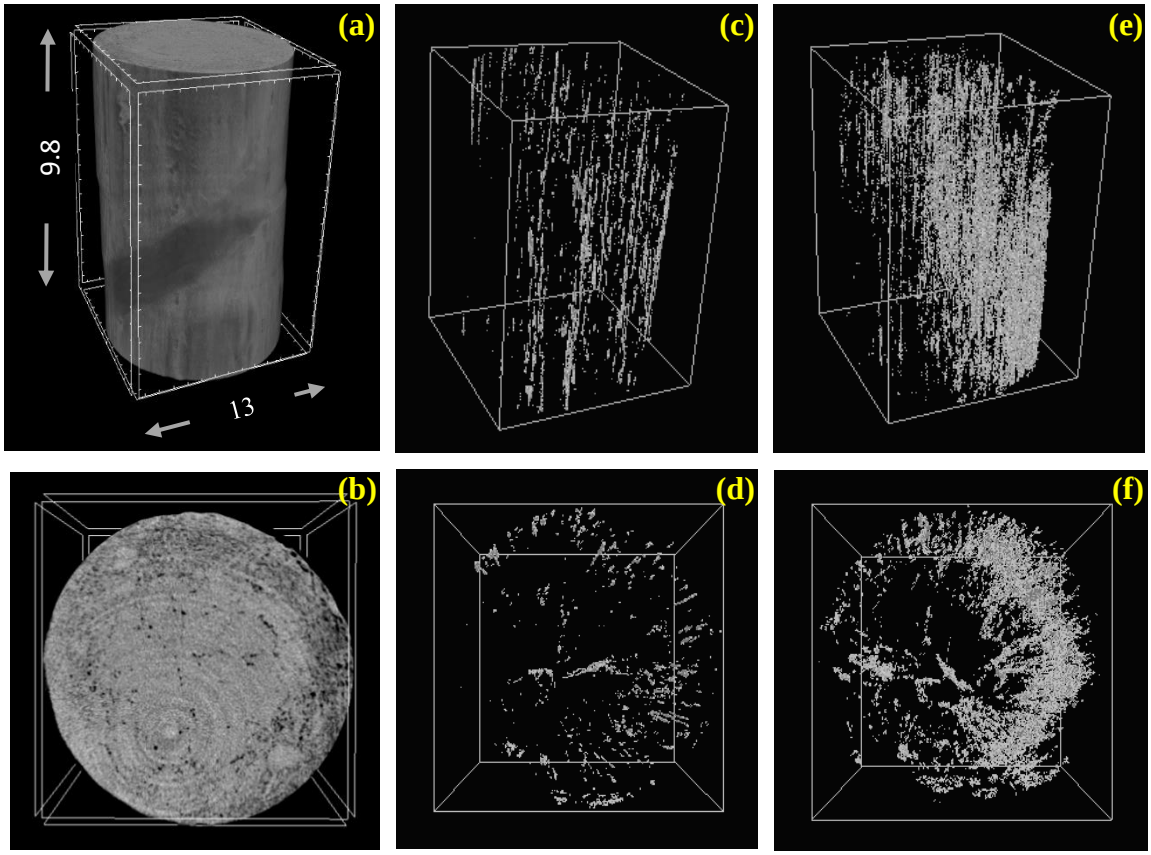

Figure 5.4 Showing: (a) reconstructed 3D image for GFRP size 4 sample; (b) cross section image of sample a; (c) 3D image of the distribution of voids for control sample; (d) cross section image of sample c; (e) 3D image of the distribution of voids and their increasing for the tested sample up to 95% ultimate load; (f) cross section image of sample e. (*Note:* the fibers and matrix are depicted invisable while the voids and their increasing are depicted as white)

Voids and their increase with load was visualized using the CTvox software (Bruker). Figure 5.5 and Figure 5.6 show some reconstructed slices in the x-z plane that are extracted from control samples and loaded FRP rebars. After a thorough investigation of the samples using reconstructed longitudinal section images of control rebar and a loaded GFRP size 4 the examples in Figure 5.5 were chosen as they show the more critical changes observed in the rebar with increasing load. For the control sample the fibers in the image, Figure 5.5a, are well distributed. The control sample does contain some noticeable voids, but they are less than 2 mm in length. For the sample tested up to 40 % of the ultimate load voids with length more than 2 mm were observed, in Figure 5.5b. For the sample tested up to 64 % of the ultimate load, Figure 5.5c, the interconnection between voids increases and the voids increase in thickness. For the sample tested up to 64 % of the ultimate load the misalignment of the voids with the longitudinal axis is noticeable, indicating the starting of other type of damage such as longitudinal matrix micro-cracking. For a sample tested up to 95 % of the ultimate load, Figure 5.5d, shows again a misalignment of the longitudinal voids and an increasing density of voids near the outer surface. The reason for the growth of the voids maybe that the resin has a smaller modulus of elasticity than the fibers. Therefore, some fibers were broken and pulled out under tension leading to the longitudinal growth of the voids.

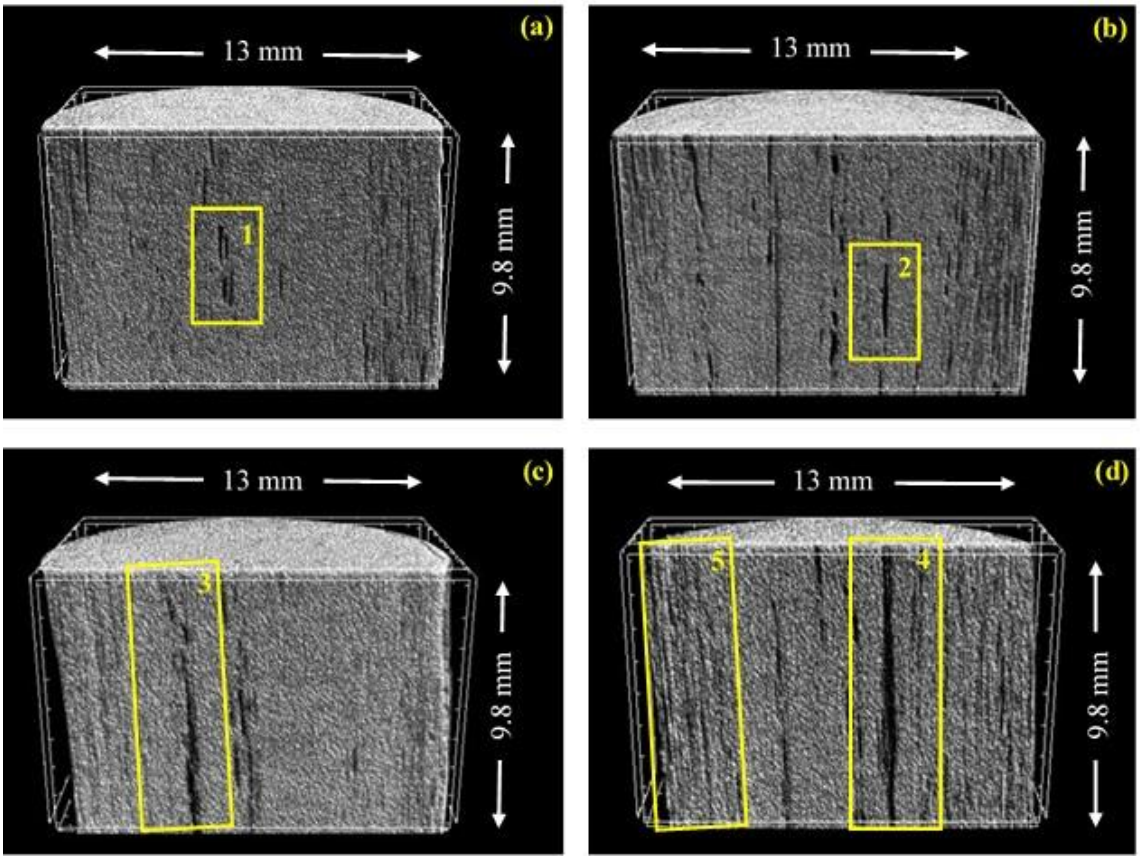

Figure 5.5 Microstructural changes observed using 3D μ CT images of the GFRP size 4 rebar samples after being subjected to tension at varying fractions of the ultimate load. (a) Control sample showing the voids that are less than 2 mm (1); (b)Tested up to 40% of the ultimate load showing the voids that are more than 2 mm (2); (c) Tested up to 64% of the ultimate load showing to the interconnection between the voids (3); (d) Tested up to 95% of the ultimate load showing the misalignment of the longitudinal voids (4), and the increases of the voids density near the outer surface (5)

Figure 5.6 shows representative reconstructed longitudinal section images for a control rebar and a loaded CFRP size 4 samples. These images were also chosen after a thorough investigation of the samples using reconstructed longitudinal section images of control rebar and a loaded CFRP size 4. The examples in Figure 5.6 were chosen as they show the more critical changes observed in the rebar with increasing load. It should be noted that each image is from a different sample. For the control sample, Figure 5.6a, the image has longitudinal voids that extend through the length of the 9.8 mm sample. For the sample tested up to 40 % of the ultimate load, Figure 5.6b, there is an increase voids with length more than 4 mm and a small increase in the void thickness were observed. For the sample tested up to 70 % of the ultimate load, Figure 5.6c, there is an increase in the number of voids extending through the entire length of the sample and an increase in the thickness of the voids. For the sample tested up to 99 % of the ultimate load, Figure 5.6d, a longitudinal split of the outside layer occurred along the full 9.8 mm of the sample. The figure also showed off longitudinal axis alignment of some of the voids.

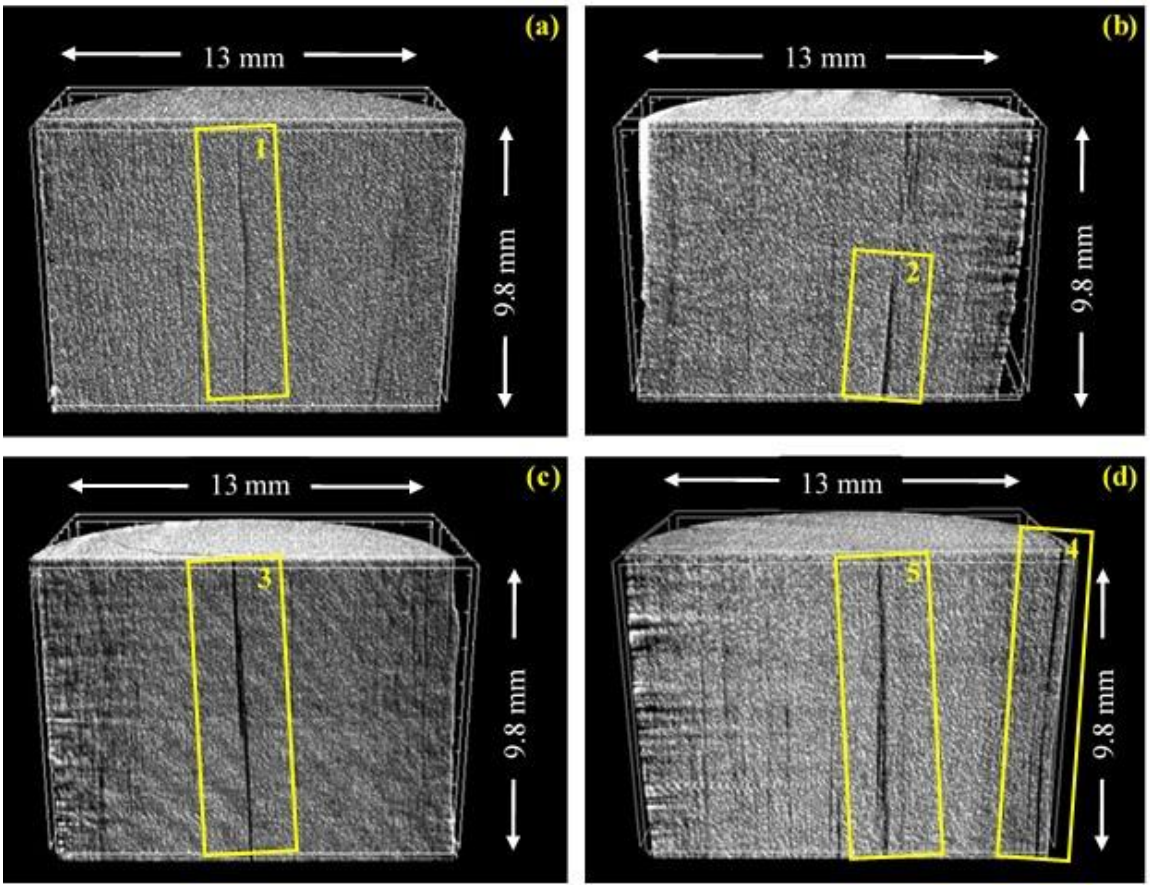

Figure 5.6 Microstructural changes observed using 3D μ CT images of the CFRP size 4 rebar samples after being subjected to tension at varying fractions of the ultimate load. (a) Control sample showing the longitudinal voids (1); (b) Tested up to 40% of the ultimate load showing the voids with length more than 4 mm (2); (c) Tested up to 70% of the ultimate load showing the longitudinal voids (3); (d) Tested up to 99% of the ultimate load sample showing longitudinal split (4), and off longitudinal axis alignment of some of the voids (5)

5.4.2 Damage Volume Fraction

The percentage of the damage area was calculated for each slice using fraction of pixels above a set threshold (see Figure 5.3i). In other words, the damage is assumed to be the void fraction. Then, the volume percentage for the four different FRP rebar samples was averaged over 1000 slices and is plotted in Figure 5.7. Figure 5.7 shows CFRP size 2 rebar has a higher void percentage than CFRP size 4. GFRP size 4 has a higher void percentage in the early stage of loading, but lower void percentage after 50% ultimate load. The CFRP rebars have a noticeable increase of void percentage after 40 % ultimate load for size 2 and after 50% ultimate load for size 4. GFRP rebars in comparison have a noticeable increase of void percentage after 30 to 40% ultimate load. The void percentage increases steadily with loading in both CFRP and GFRP bars. Table 5.2 shows the void percentage for these sample rebars, after subtracting the void percentage of the control bars formed during the pultrusion process.

Table 5.2 Void volume percentage of FRP sample rebars

	% Void Volume			
% Ultimate Load	**CFRP-2**	**CFRP-4**	**GFRP-4**	**GFRP-6**
30	0.13	0.04	0.12	0.05
50	0.57	0.19	0.65	0.70
70	1.14	0.64	0.84	1.35
90	1.28	1.13	1.10	1.71
99	2.48	1.57	1.35	1.81

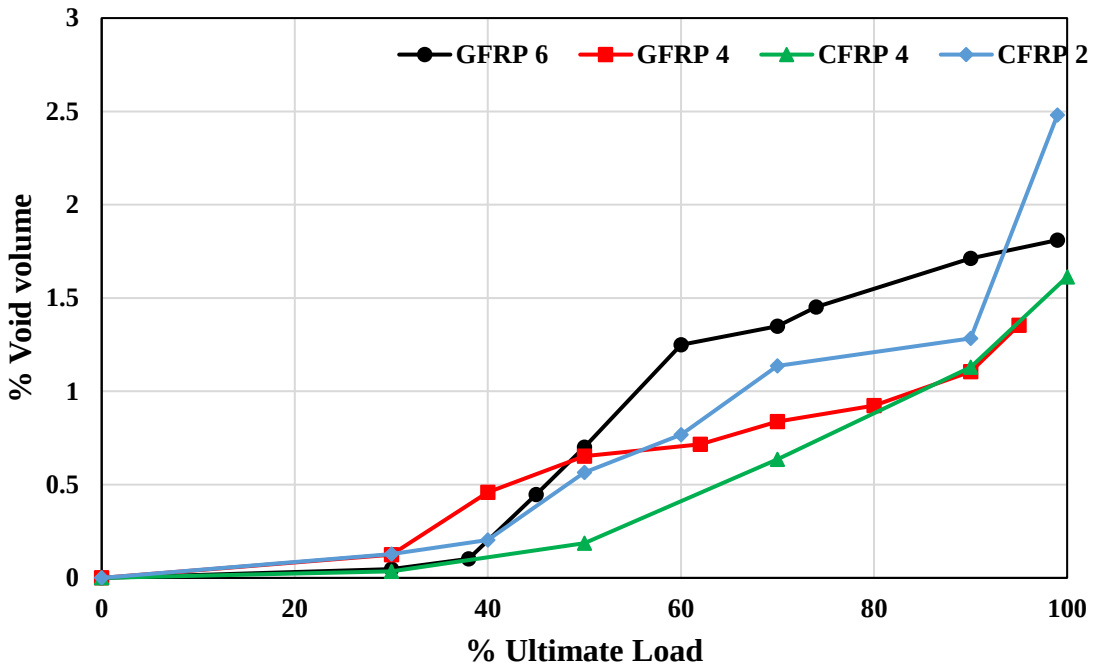

Figure 5.7 Ratio of the void volume as a function of the increasing tensile loading, after subtracting the void percentage of the control bars formed during the pultrusion process

5.4.3 Void Thickness Evolution with Load

Thickness of the voids were estimated using the distance transform method (Remy and Thiel 2002). The distance transform defines a distance between a specific pixel and the nearest nonzero pixel of the binary selection which was explained firstly by Hildebrand and Ruiegsegger (1997) by means of local thickness (Hildebrand and Rüegsegger 1997). In this method, Local thickness was defined as a diameter of a largest sphere within the volume of interest that include a specific pixel need to be measured. This point is not needed to be at the centre of the sphere, but the sphere should be completely fit inside the structure, voids and their increasing in this study. After that, a mean value was calculated

for all local thicknesses and defined as a mean thickness of this specific object (Hildebrand and Rüegsegger 1997). Figure 5.8 summarizes the damage thickness distribution data gathered from µCT images at different ultimate load stages for GFRP size 6 and CFRP size 4 respectively. The figure shows the void volume representing a given thickness.

Assessment of µCT data showed that the void volume increases at a higher load level with a slight trend in increasing in void thickness in GFRP size 6, while there is a noticeable increase in the void volume and thickness with increasing load level in CFRP size 4. It can be noticed that the maximum void thickness for the control CFRP size 4 sample is 0.11 mm, and that the void thickness increases up with the void volume as the load increases. Minimum void volume for the void thickness of 0.11 mm equals to 0.009 mm^3 for the control sample and the maximum volume equals to 0.523 mm^3 for a sample tested up to 90% ultimate. In comparison, the maximum void thickness for the control sample of GFRP size 6 is 0.27 mm, and the void thickness has a small increase with the void volume as the load increases. Minimum void volume for the void thickness of 0.27 mm equals to 0.018 mm^3 for the control sample and the maximum volume equals to 0.0545 mm^3 for a sample tested up to 99% ultimate. Maximum void thickness equals to 0.285 mm in GFRP sample and 0.18 mm in CFRP sample.

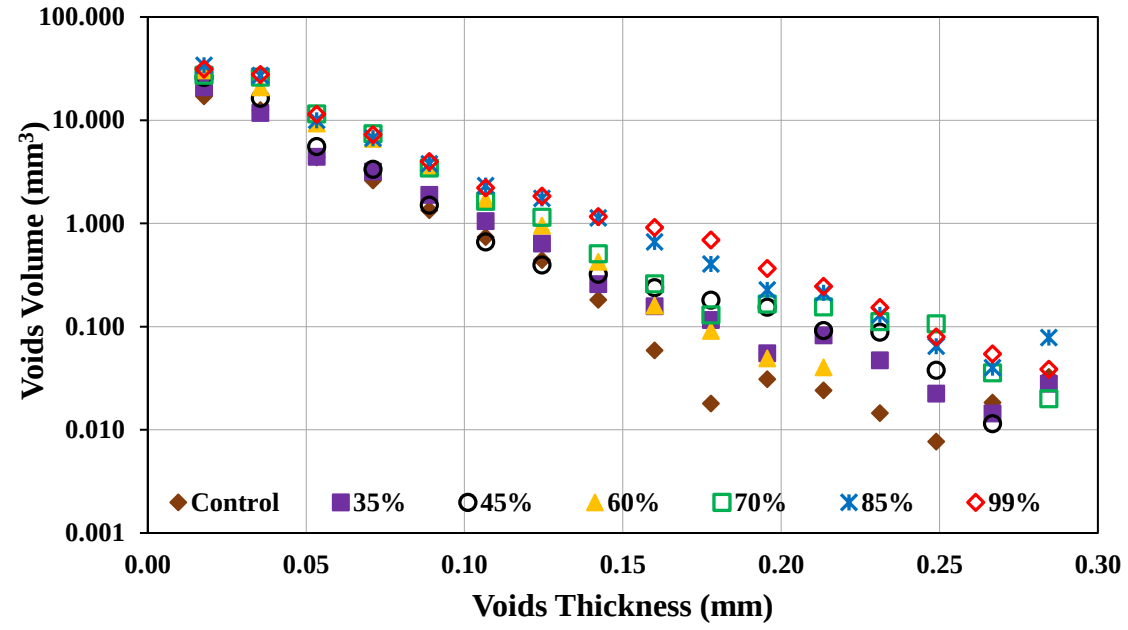

a) GFRP size 6

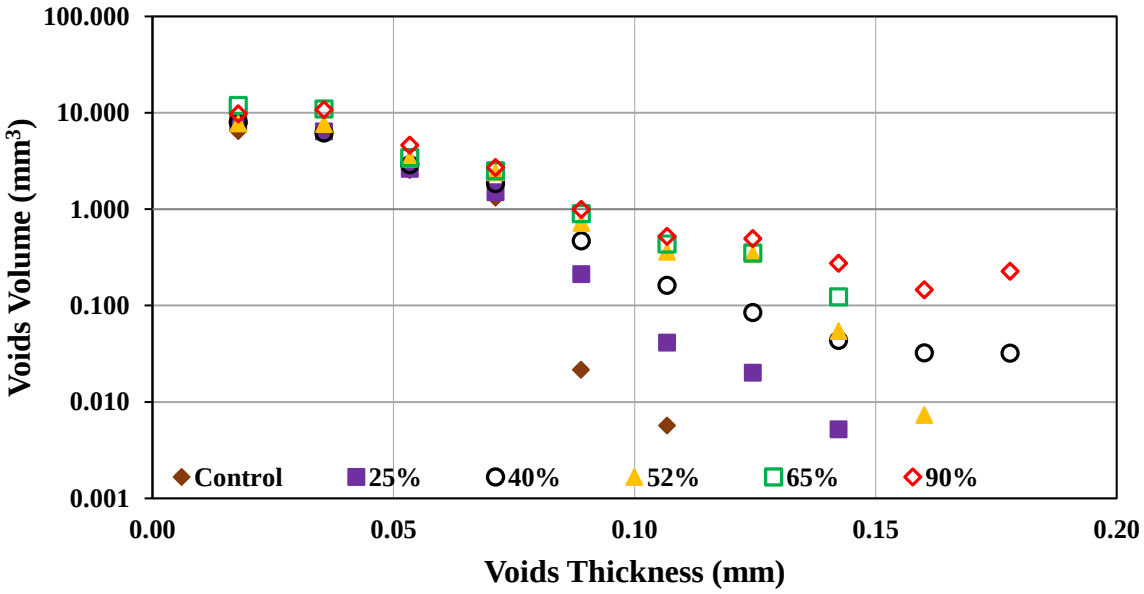

b) CFRP size 4

Figure 5.8 Distribution of voids thickness as a result of tension test for a) GFRP and b) CFRP

5.5 Comparison between µCT scan and SEM Results

The percentage of void area was calculated for a chosen slice by finding the fraction of pixels above the threshold. Table 5.3 compares the void percentage of the CFRP and GFRP rebar samples measured using µCT scan and SEM analysis. Maximum difference was 0.15% and average difference was 0.05%.

Table 5.3 Percentage of void area of FRP rebar samples using µCT scan and SEM techniques

Rebar Type	% Ultimate Load	Void Percentage Area (%) using µCT	Void Percentage Area (%) using SEM
GFRP-4	95	4.02	4.17
GFRP-6	74	4.36	4.32
CFRP-2	50	3.35	3.36
CFRP-2	70	3.62	3.68
CFRP-4	52	3.34	3.37

5.6 Results and Discussion from AE Analysis

The acoustic data in this section was compared to results obtained from µCT results. Frequency domain was used to analyze AE data. Each acoustic event was identified using the Root Mean Square (RMS) algorithm as described in (Shateri et al. 2017). The FFT was

calculated for each event and all of these have been plotted in Figure 5.9 for two types of FRP rebar. Frequencies bands were chosen using these distributions by identifying notches. Acoustic emissions originate from the release of acoustic energy due to cracking and delamination. Therefore, void volume growth was compared to the cumulative energy of the acoustic emissions. The cumulative energy of the FFT signals was calculated by means summing the energy within the band. The cumulative energy for each band was plotted relative to the fraction of ultimate load ranging from zero to 99% in 5% increments. GFRP size 6 in Figure 5.9a was divided into two frequency bands: 100 – 130 kHz and 130-190 kHz, while CFRP size 4 in Figure 5.9b was divided into three bands: 50 – 120 kHz, 120 – 160 kHz, and 160 – 200 kHz. Since the cumulative energy raised more or less uniformly for the different frequency bands, the frequency band with the largest cumulative energy was used in Figure 5.10 for comparing AE and μCT results. Normalized cumulative energy was plotted for frequency band of 130 – 190 kHz for GFRP size 6 and 160 - 200 kHz for CFRP size 4 as a function of the percentage load in Figure 5.10. In addition to that, the normalized void volumes at a void thickness of 0.142 mm for GFRP size 6 and 0.107 mm for CFRP size 4, and were plotted as a function of the percentage load as well. The correlation between cumulative energy in the AE and void percentage measured using μCT are very good. This correlation supports the notion that the growth in the void volume is due to increasing damage.

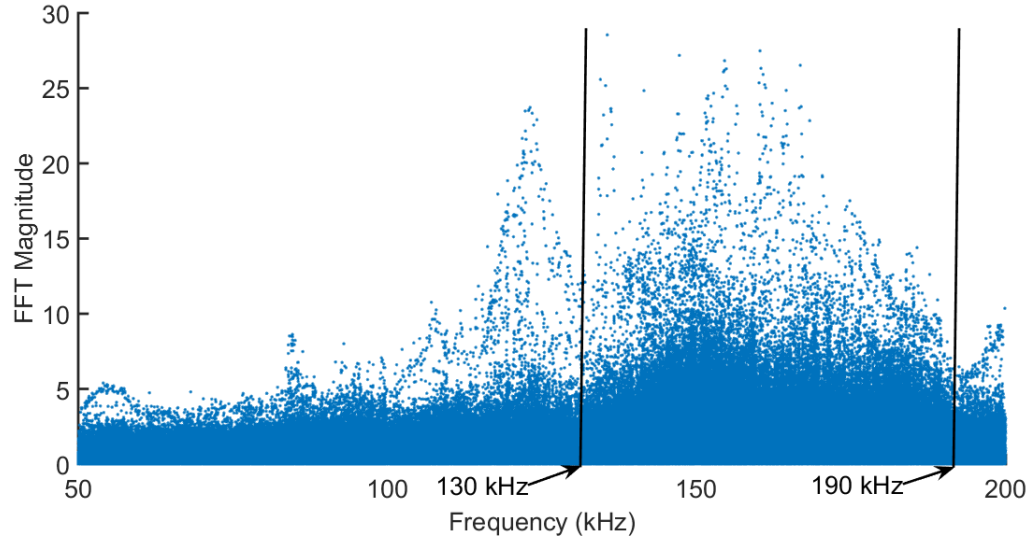

a) GFRP size 6

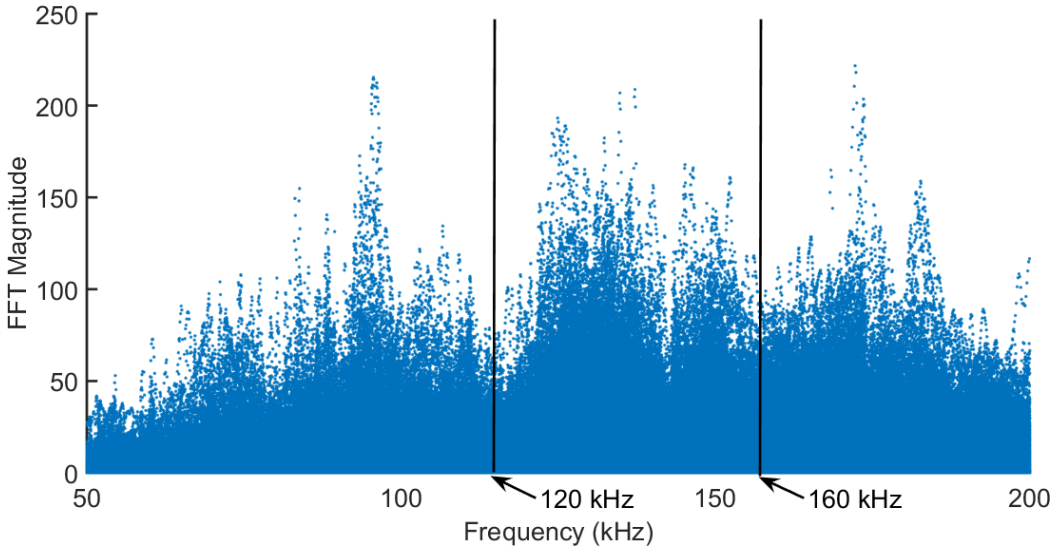

b) CFRP size 4

Figure 5.9 Fast Fourier Transform (FFT) of acoustic emission events for a) GFRP size 6 and b) CFRP size 4 rebar samples

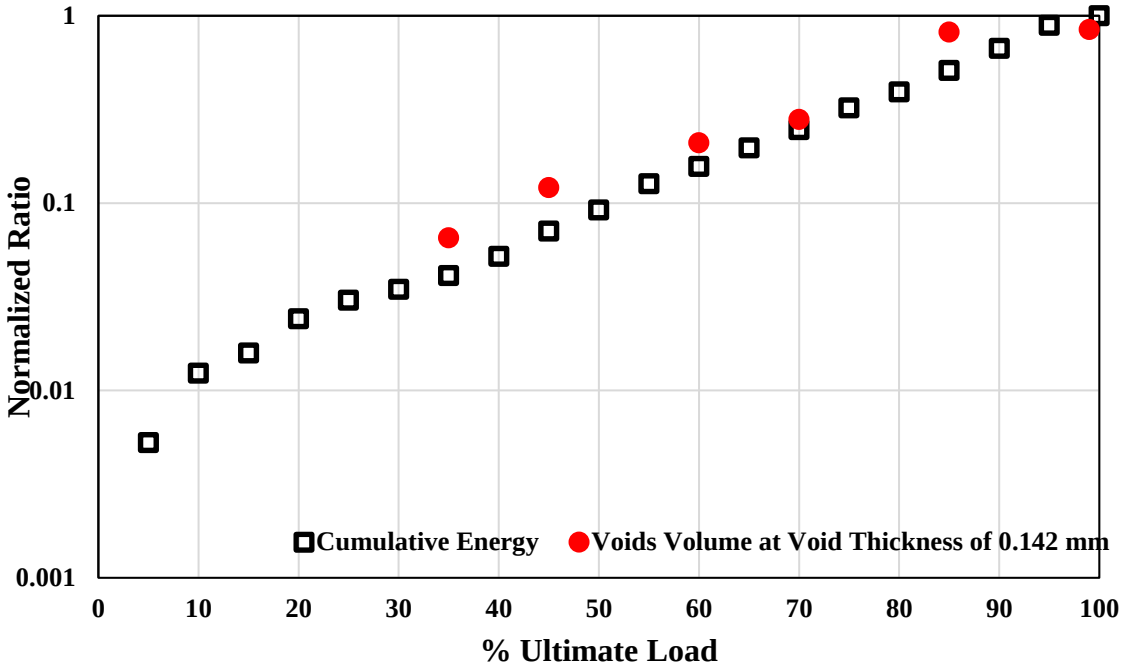

a) GFRP size 6

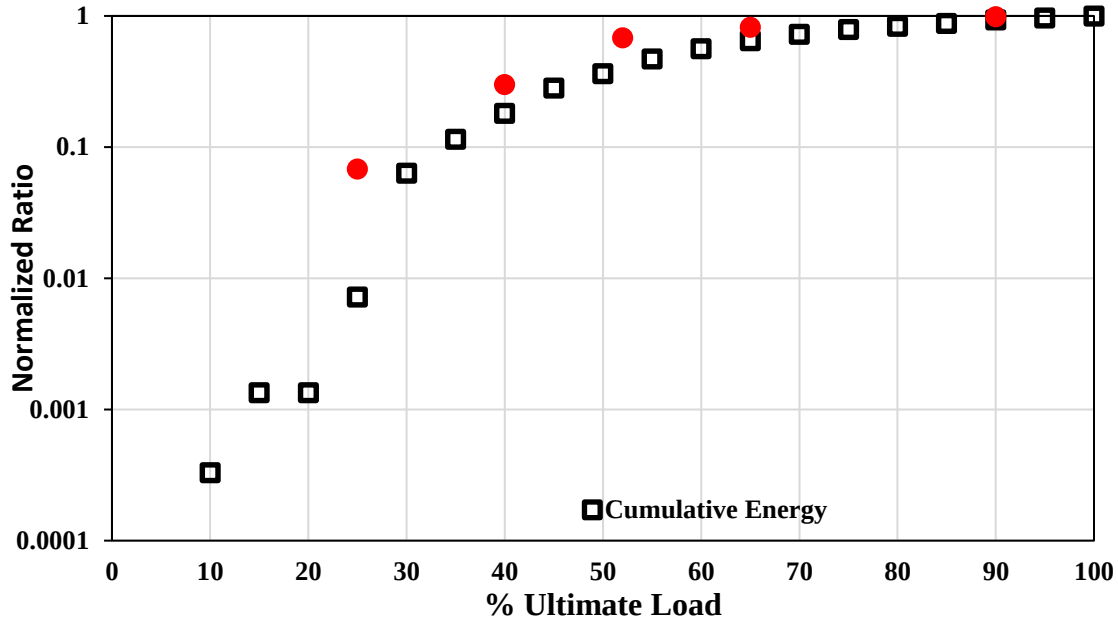

b) CFRP size 4

Figure 5.10 Comparison between normalized cumulative energy behaviour and cumulative void volumes at a specific void thickness behaviour for a) GFRP and b) CFRP rebar samples

CHAPTER 6

ENHANCED SOURCE LOCATION IN PULTRUDED GFRP AND CFRP REINFORCING BARS USING ACOUSTIC EMISSION (AE) AND MICRO COMPUTED TOMOGRAPHY (µCT) SCAN

6.1 Introduction

In this chapter, the AE that were generated from PLBs test on different locations at the FRP rebars were used to estimate the source location using the conventional linear source location using Δ_t. Δ_t is calculated (Prosser 2002) from the arrival time of the AE waves (Prosser 2002). However, the determination of the arrival time is complicated by the presence of multiple modes that the AE waves can travel in (Prosser 2002). The studies to date have confirmed that an ANN can improve the accuracy of source location. Neural network is known to be appropriate for resolving multidimensional non-linear problems. In composite materials, the inhomogeneity and acoustic anisotropy results to signal attenuation and dispersion that could make the source localization more challenge. The ANN can use different input data for localization, so it is possible to account for the attenuation and different propagation paths. However, the ANN have not yet been applied to FRP rebar, which are important materials for civil engineering applications. In the present study the ANN were used to reduce the AE source location errors in the FRP rebar. The system was trained and tested using the PLB to simulate the AE events. The trained ANN was used to identify source locations during a tensile loading test on two different FRP bars. The µCT was used to measure the damage density along the FRP bars after

tensile load testing. An additional contribution of this study is a comparison between the density of location of AE signals determined by the ANN method with damage density measured with the μCT analysis along the same CFRP and GFRP rebars.

6.2 Wave Velocity

PLB tests were used to determine the velocity of the AE wave propagation for CFRP and GFRP rebars. When the pencil lead breaks, an elastic wave is produced that propagates through the rebar sample. These waves have short rise time and are similar to AE signal generated from a crack (Prosser 2002). Ten PLBs were performed within a few mm of the anchor and hence within 2 cm of one sensor, while the second sensor was located on the anchor at the opposite end of the bar, as shown in Figure 6.1. The PLB test is performed with a 0.5 mm HB pencil lead with the length of 2.5 mm at an angle of 30^o, as suggested in (Miller 1987). Circular foam ring was used to ensure that the pencil was held at the same angle. The difference in time, Δ_t , that it takes a wave to travel from one sensor to another in a FRP sample, was determined by using the equation below:

$$\Delta_t = |t_2 - t_1| \quad \ldots\ldots\ldots\ldots\ldots\ldots\ldots\ldots\ldots\ldots\ldots\ldots\ldots\ldots\ldots\ldots\ldots\ldots \quad (6.1)$$

Where: t_1 and t_2 are the arrival time of the wave at sensor 1 and 2. The RMS algorithm was used to identify the start of each signal to minimize the effect of threshold level, as shown in Figure 6.2. The velocity was determined by dividing the distance between the two positions of the PLB by Δ_t.

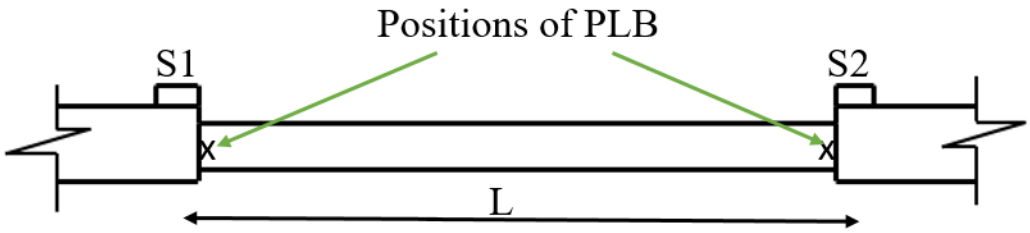

Figure 6.1 A schematic of pencil lead break test on FRP bar samples used to determine the AE propagation velocity

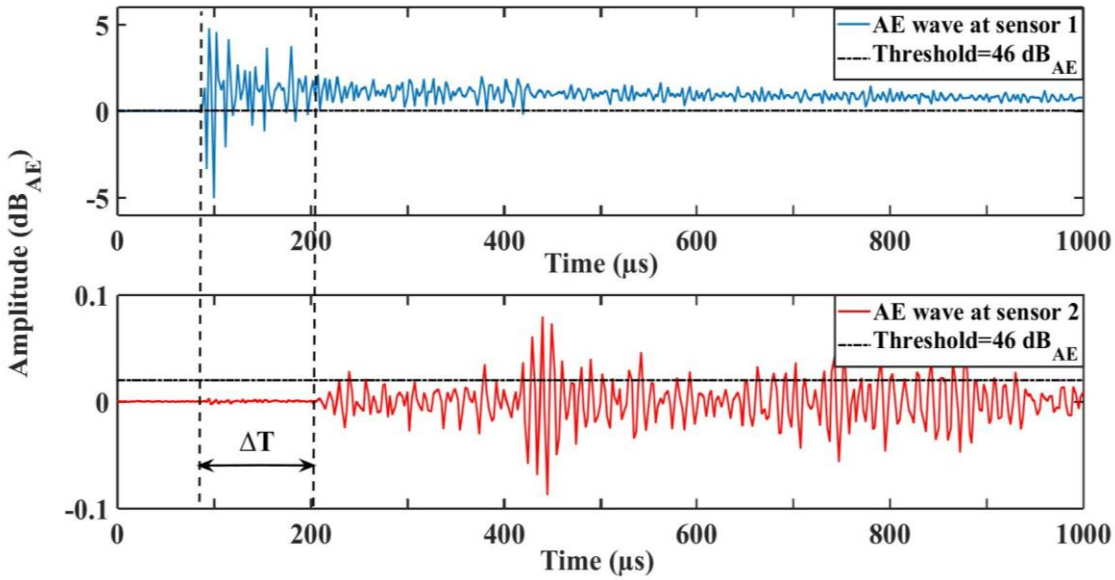

Figure 6.2 Signal arrival from a PLB at the two sensors. Dashed lines denote the arrival time at each sensor

It is expected that there will be variation in the time difference between the arrival of each signal due to factors such as the wave's propagation mode or dispersion (Prosser et al. 1995). For example, the flexural mode will travel at lower velocity and is highly dispersive

than waves that travel in extensional mode (Prosser et al. 1995). Figure 6.3 shows different velocities for signals with amplitudes more than 90 dB_{AE} for untested FRP rebars.

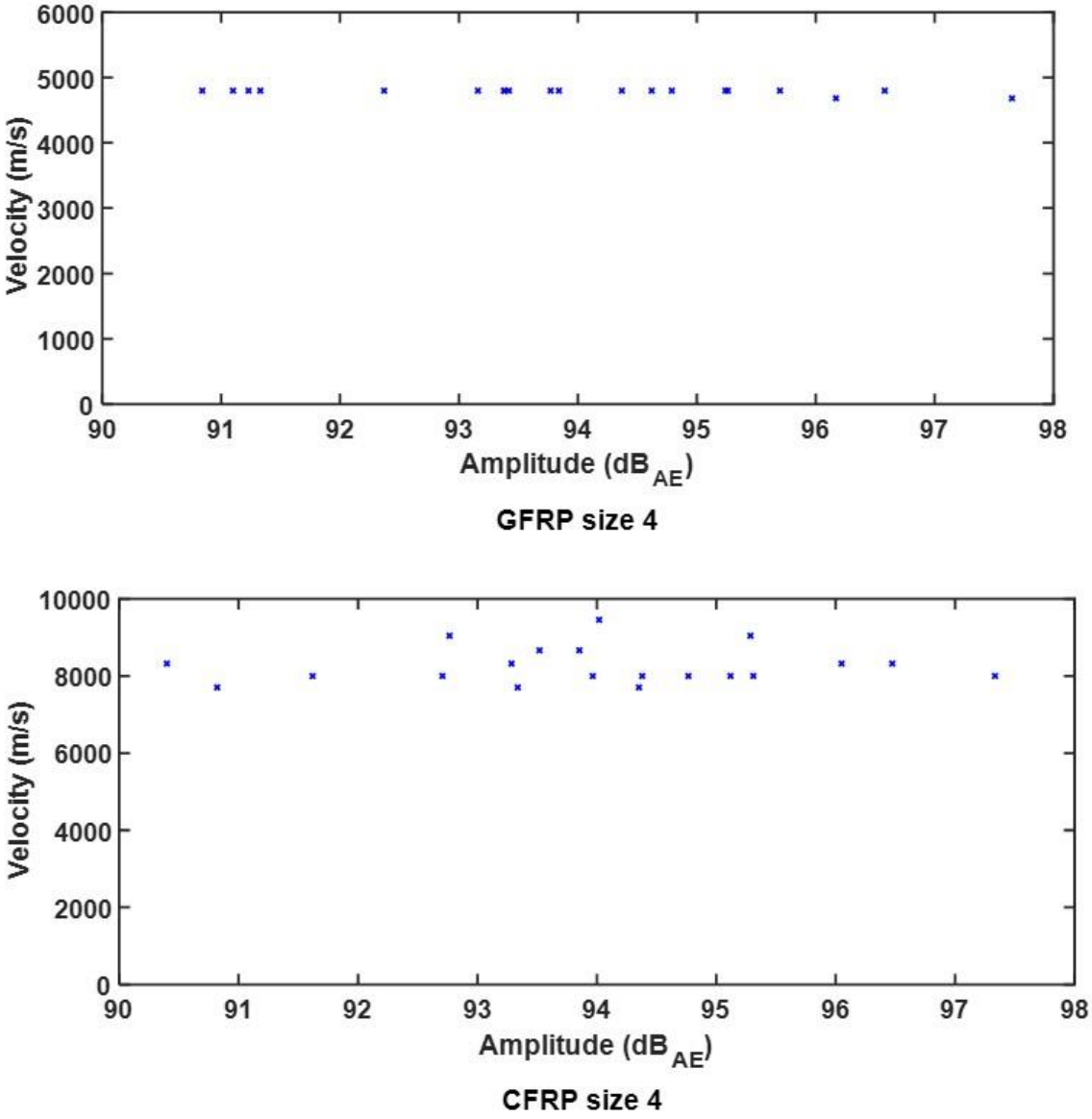

Figure 6.3 Velocity calculations of different high amplitude AE signals for untested CFRP and GFRP rebars

Previous work has demonstrated that the velocity of composite laminates depends on the fiber orientation and the elastic properties of the material (Nunes et al. 2002). In the current study, the wave velocity of continuous FRP bars was checked to determine if it changes during the load – unload – reload tension test. Ten PLBs were performed at loads from 0 to 90% predicted ultimate load in increments of 10 % of the predicted ultimate load. The velocity was determined and correlated to Modulus of Elasticity (E) estimated from the stress strain relationship. The stress strain relationship remained elastic until the ultimate load was reached and hence the modulus of elasticity and velocity also maintained constant up to failure.

Differences in mode velocity and dispersion of AE events will lead to errors in the estimated source location. In addition, many overlapping signals would be displayed in a real-time test as many AE signals are generated in different positions and arrive to the sensors at the same time. Source location results would be inaccurate if it depends on velocity itself. In homogeneous materials, the error would be small; however, the error would increase in inhomogeneous materials such as FRP composites as the wave propagates in different wave modes and velocities (Rose and Nagy 2000).

6.3 Source Location Determination

6.3.1 Conventional Linear Source Location Method

In conventional linear source location, the time difference between the arrival time of an AE event is used to estimate the position of the AE source. Source location can be either linear, two, or three dimensional depending on the structure geometry. Source location on FRP rebars can be calculated using the linear source location as the bar can be regarded as one dimensional. In this study, artificial AE signals were generated on a FRP rebar using PLB test and detected by two sensors attached on each anchor. Six PLB tests at 3 cm intervals were carried on GFRP size 4 while five PLB tests were carried out every 5 cm for CFRP size 4 as shown in Figure 6.4. The signals were stored for post processing.

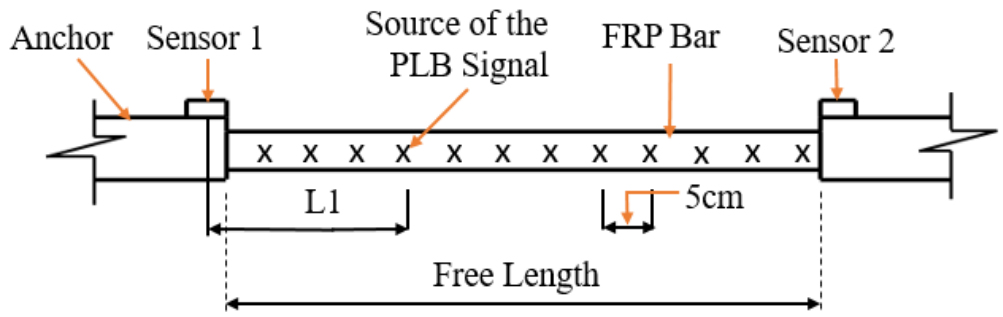

Figure 6.4 A schematic of pencil lead break test performance on FRP bar samples for linear source location determination

The arrival time and AE event amplitude were determined using both the RMS and threshold based algorithms. From the 90 PLB tests the RMS algorithm identified 164 AE events and threshold based algorithm identified 222 AE events for the GFRP size 4 sample. From the 55 PLB tests the RMS algorithm identified 71 AE events and threshold based algorithm identified 135 AE events in the CFRP size 4 sample. The difference in the arrival time ΔT was calculated using equation 2. The propagation velocities used were 4800 m/sec for GFRP and 8000 m/sec for CFRP, as determined before in Figure 6.3. The conventional linear source location for both RMS and threshold based algorithms was calculated using difference in the arrival time according to the following relationship:

$$L_1 = \frac{1}{2}(L + V \times \Delta_T) \quad \ldots\ldots\ldots\ldots\ldots\ldots\ldots\ldots\ldots\ldots\ldots\ldots\ldots\ldots\ldots\ldots \quad (6.2)$$

Where: L_1 is the distance from a PLB at a specific point on the FRP rebar to the sensor that attached at one end; L is the free length.

6.3.2 Artificial Neural Network (ANN) Source Location

The ANN is a computing system that was designed to simulate the processing of information by layers of neurons (Shanmuganathan and Samarasinghe 2016). The system consists of individual elements called neurons that connected via coefficient (weights). The system consists of an input layer, one or more hidden layers and an output layer.

Information processes in two phases, training and recall phases. The network is trained using examples and find a relation between the input and output data (Shanmuganathan

and Samarasinghe 2016). In the recall phase, the new set of data is used through the trained network and a recall algorithm is used to calculate the results.

In general, there are two groups of learning algorithms: supervised and unsupervised learning algorithms. The supervised learning algorithm uses a symbolic function to relate the input vectors to the desired output vectors, while the unsupervised learning algorithm uses only input vectors and classify the measured values using their internal features.

A supervised learning ANN approach was used to determine the source location of the PLB tests, described in 6.3.1, for both GFRP size 4 and CFRP size 4 samples. In an ANN neurons process information in a connected network. In this work, the connected network of neurons consists of an input layer, an output layer and two hidden layers. In this work supervised learning was used to adjust the weights of the hidden layers. After training the ANN provides a function that relates the input and output data (Demuth 2000).

The ANN was trained using preprocessed signals that were fed to the input layer and the PLB locations. The AE signals were preprocessed using the RMS algorithm or threshold based algorithm. For each AE event, the preprocessing produced peak amplitude for the signal at sensor 1 (A1), peak amplitude for the signal at sensor 2 (A2), and Δ_t which were used as the input for the neural network (three neurons in the input layer). Distance from the source of the PLB signal to sensor 1 (L1) was used as the target (correct answer for every input data). Using the preprocessed inputs and the PLB locations the network was trained using the neural network fitting tool (Demuth 2000) . The input data was divided

into training data to find the weights, and another set of data to check the final performance of the network (Demuth 2000). In this work a two-layer feed-forward network was used to fit the data with a nonlinear hidden layer (sigmoid neurons) and a linear output layer as shown in Figure 6.5. Bayesian Regularization training algorithm was used as that is the recommended approach that yields acceptable generalization for smaller data sets (Demuth 2000). The number of neurons was incremented from 10 to 26 and training was carried for each number of neurons. The average error for the testing data was calculated and compared in order to select the number of neurons that produced the minimum average error. As shown in Figure 6.6, the average error was minimum with 20 neurons. After 20 neurons, the network was overfitting and did not generalize it properly. Therefore, in this study, 20 neurons were used in the hidden layer.

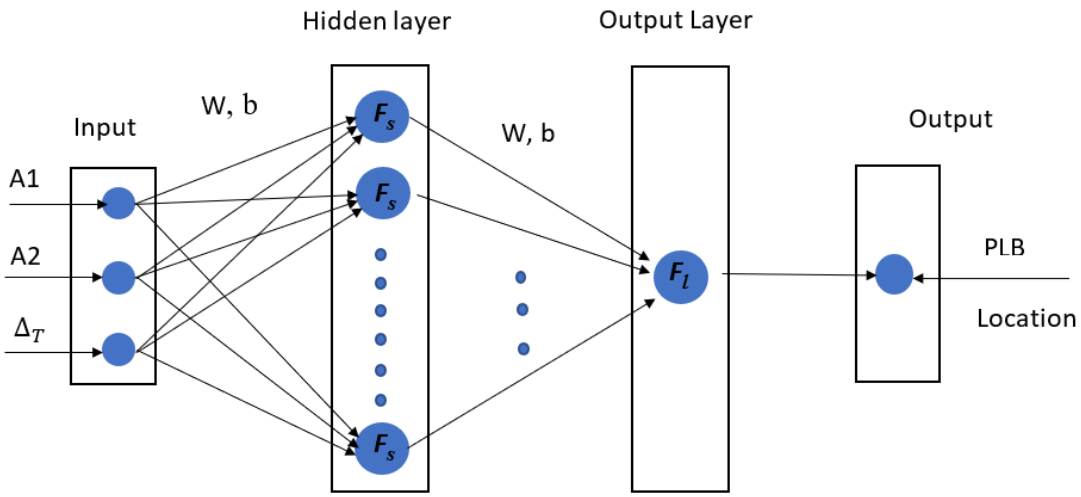

Figure 6.5 Schematic of the ANN used in this study where A1 and A2 are the peak amplitude of AE signal at the sensor 1 and sensor 2 respectively; Δ_T is the difference time; F_s is the activation of the hidden layer (sigmoid function); F_l is the activation function of the output layer (linear function); W is the weight; and B is the bias

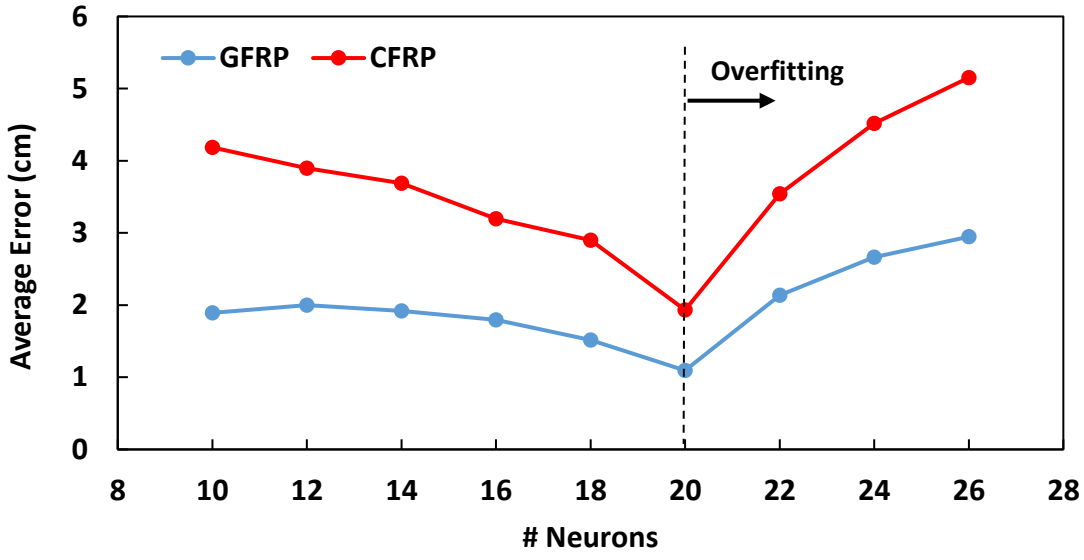

Figure 6.6 The average error of the testing data versus the number of neurons

For GFRP size 4, 164 AE events were used and for each event three features were extracted that became the three input vectors. For CFRP size 4, 71 AE events were used as input. For GFRP size 4, 85% of data was used for training the network and 15% was used for checking the accuracy of the localization. For CFRP size 4, 80% of data was used for training the network and 20% was used for checking the accuracy of the localization. The error was calculated as the difference between the calculated and actual position. The error then passed backward through the network to adjust the weights to reduce the error (Demuth 2000). The ANN with the minimum standard deviation occurred at iteration number 774 and number 433 for GFRP and CFRP size 4 respectively. Figure 6.7 shows the errors between the calculated and actual position for GFRP and CFRP samples.

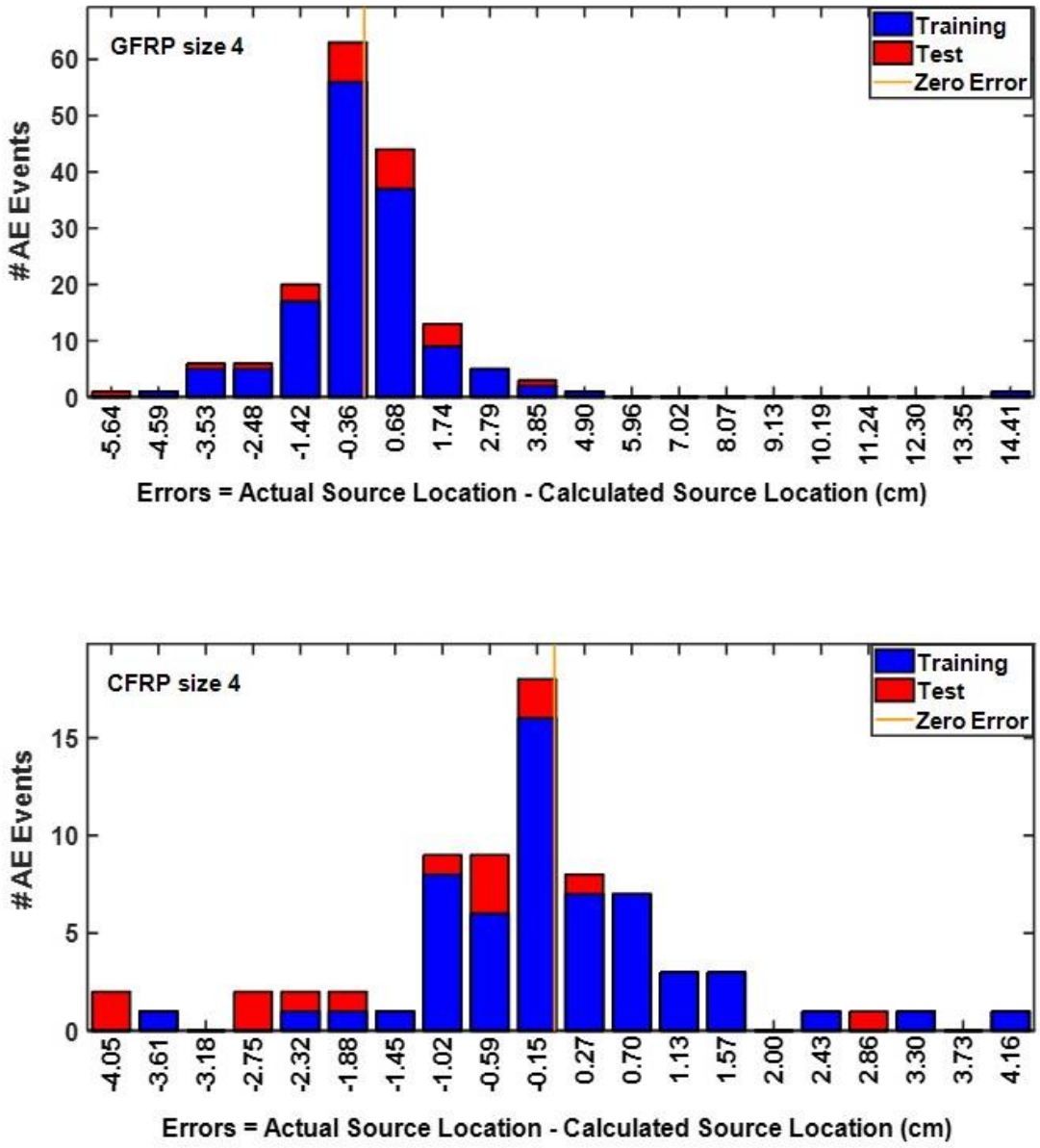

Figure 6.7 Errors between real PLB source and the calculated ANN locations for GFRP and CFRP samples

6.3.3 Comparison of The Source Location Results Obtained from Conventional Linear Source Location and ANN

Scatter plots of actual and calculated PLB source location are shown in Figures 6.7 and 6.8 for GFRP and CFRP size 4 rebars respectively. PLB source locations were calculated using the three methods: conventional linear source location using both threshold based and RMS algorithms and the ANN method. One metric that can be used to compare the methods is the standard deviation between the actual PLB and the calculated source location. Standard deviation between the actual PLB and the calculated source location for GFRP size 4 rebar sample is 8.43 cm using the RMS algorithm, 7.75 cm using threshold based algorithm, and 1.95 cm using ANN method. For CFRP size 4 sample, standard deviation between the actual PLB and the calculated source location is 7.84 cm using the RMS algorithm, 7.51 cm using threshold based algorithm, and 1.48 cm using ANN method.

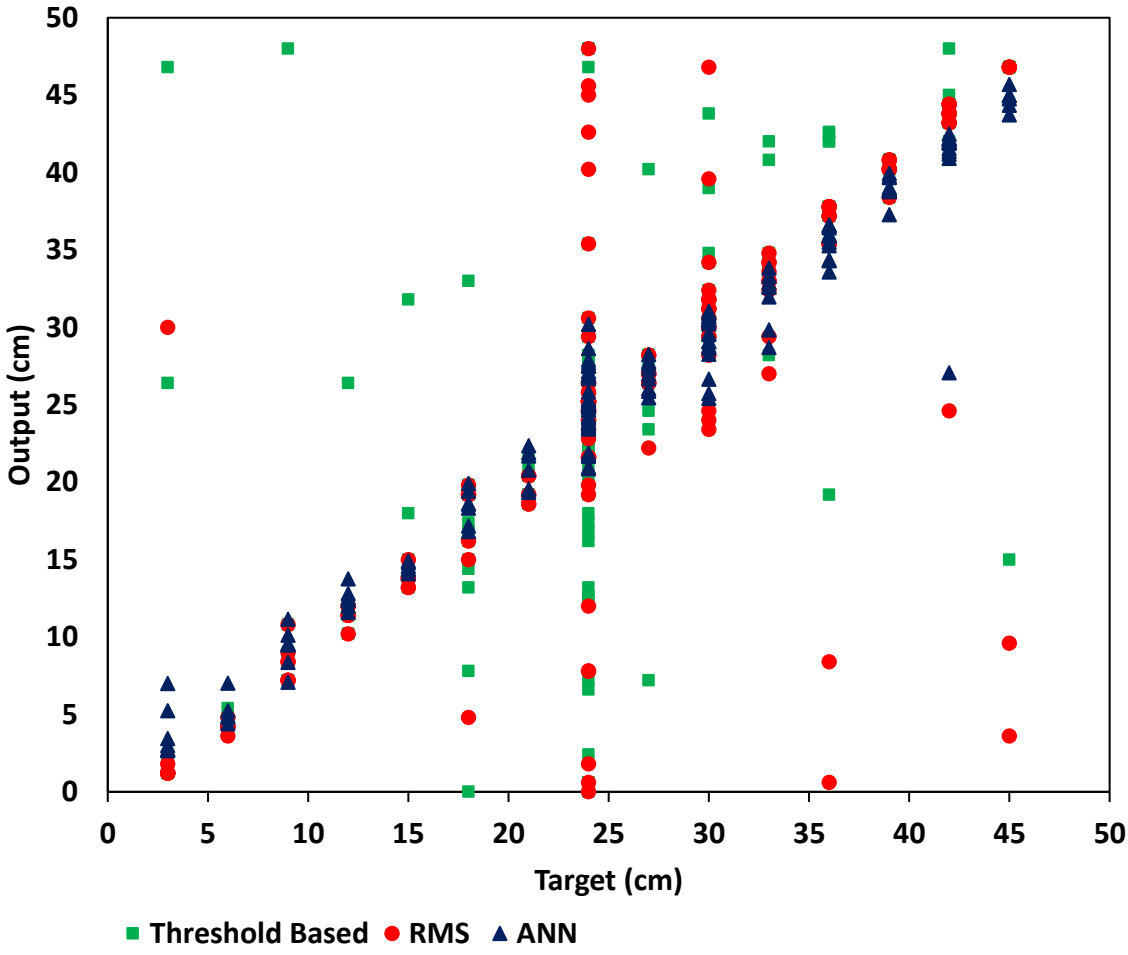

Figure 6.8 Calculated vs actual PLB source locations for GFRP size 4 rebar sample using the ANN and conventional linear source location methods. Difference in the arrival time was calculated using both threshold based and RMS algorithms

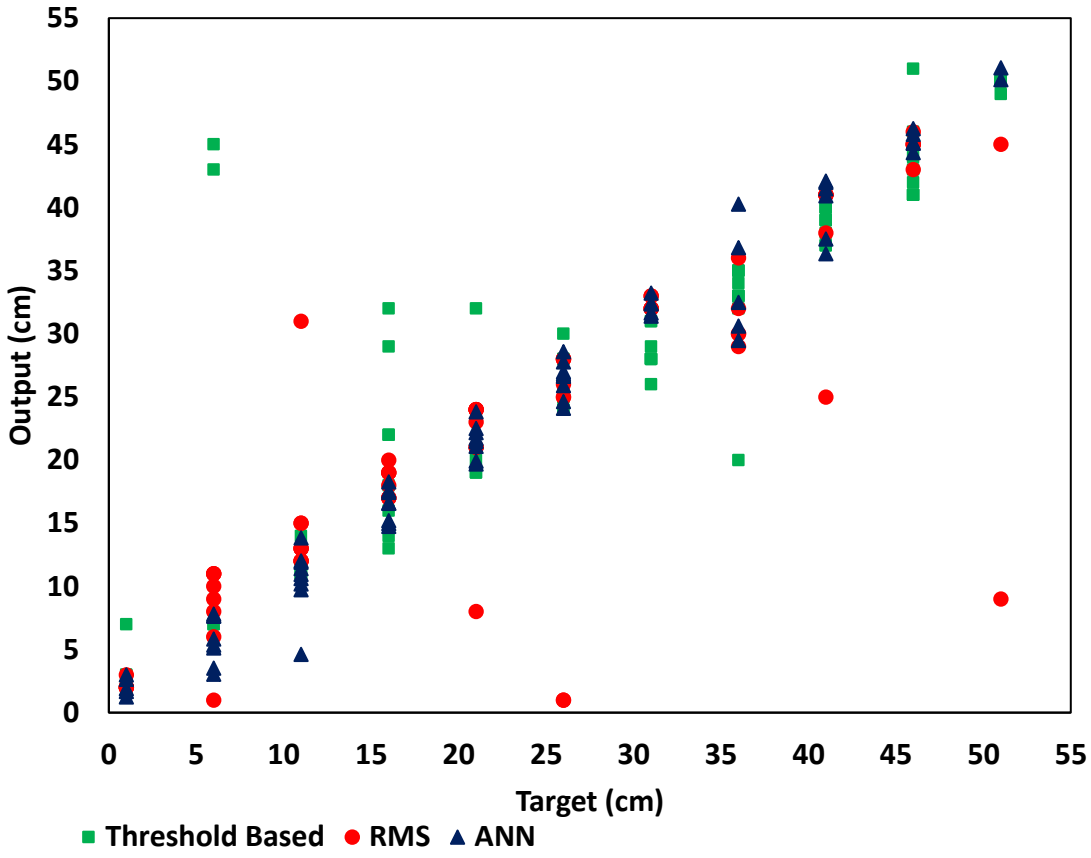

Figure 6.9 Calculated vs actual PLB source locations for CFRP size 4 rebar sample using the ANN and conventional linear source location methods. Difference in the arrival time was calculated using RMS algorithm

The variance between the actual and calculated source locations was improved by a factor of 4 for the GFRP and a factor of 5 for the CFRP when using the ANN method. The GFRP and CFRP trained neural networks were saved for later analysis of tension tests of FRP rebar samples.

6.4 Source Location of AE Events During Tension Test Using ANN

The tension tests and AE signals were carried out as outlined in chapter 3. The acoustic signals were recorded and then post processed. The RMS algorithm was used to identify the AE events. During post processing AE analysis, the amplitude at each sensor and Δ_t were used as input data and processed using the functions from the ANN for GFRP and CFRP from section 6.3.2.

The free length of the sample between the sensors was approximately 52 cm for both GFRP and CFRP. For GFRP sample, 52% of the recorded AE events had a calculated location along the sample length between the two sensors, and the rest of the events were calculated to have positions beyond the free length of the sample. For CFRP sample, 70% of the AE events were calculated to be within the free length of the sample. Any AE events calculated to have positions outside the free length of the sample as shown in Figure 6.4 were discarded and not included in the analysis. The signals with estimated positions outside the free length of the sample could be signals that were created at the grip of the machine or due cracking in the grout. Another reason that estimated positions could be outside the free length of the sample is that AE signals from different locations might arrive at the sensors close enough in time that they are erroneously considered to be originating from one signal location.

The distribution of AE events along the samples length for GFRP and CFRP rebars were also calculated using the conventional linear source location by using the RMS algorithm

and plotted in Figures 6.10a and 6.11a. For GFRP sample using the RMS algorithm, 18% of the recorded AE events had a calculated location along the sample length between the two sensors, and the rest of the events were calculated to have positions beyond the free length of the sample. For CFRP sample using the RMS algorithm, 35% of the AE events were calculated to be within the free length of the sample.

The distribution of AE events along the samples length for GFRP and CFRP rebars using ANN method were shown in Figures 6.10b and 6.11b respectively. The results showed there are differences between the conventional linear source location and ANN methods especially for CFRP sample.

6.5 µCT Analysis

6.5.1 Damage Density Along the Bars Using µCT Technique

Damage density along the bars after tension testing was determined using µCT Technique and compared with AE event localization results. After the tension test up to a load of 95-98% of ultimate, the samples of FRP bars were cut into 5 cm lengths and imaged using µCT scan. After imaging, 2000 reconstructed images near the centre of each 5-cm length, equal to a 1.8 mm length, were chosen from each piece to find the volume of damage. In the analysis the void fraction was estimated from the images and the damage percentage was set equal to the increase in void percentage. Figures 6.10c and 6.11c show the percent damage volume for GFRP and CFRP samples along the sample length.

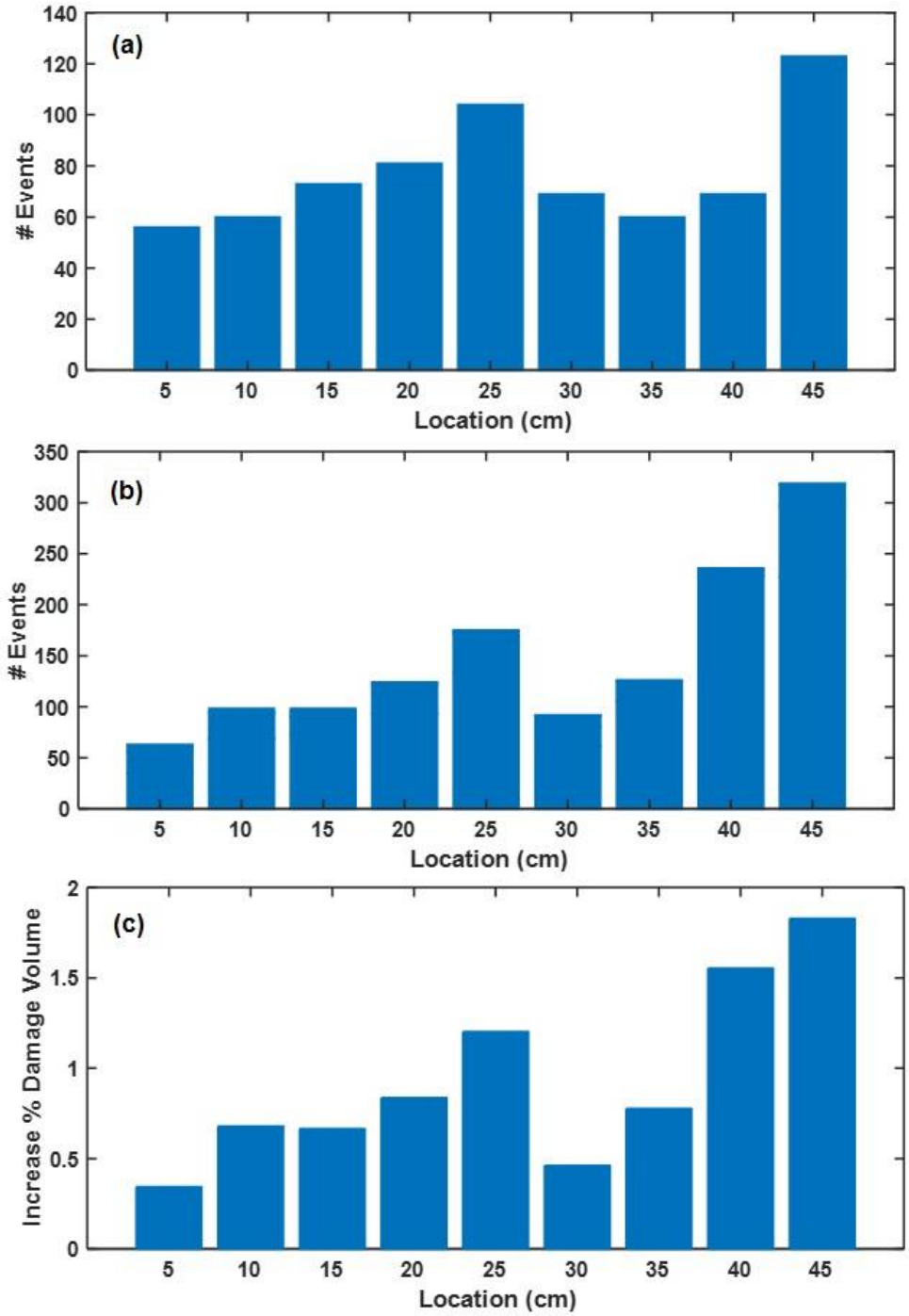

Figure 6.10 (a) Distribution of AE events along the GFRP rebar sample using conventional linear source location method. (b) Distribution of AE events along the GFRP rebar sample using the ANN method. (C) Distribution of the ratio of damage / total sample volume for the GFRP using the µCT scan

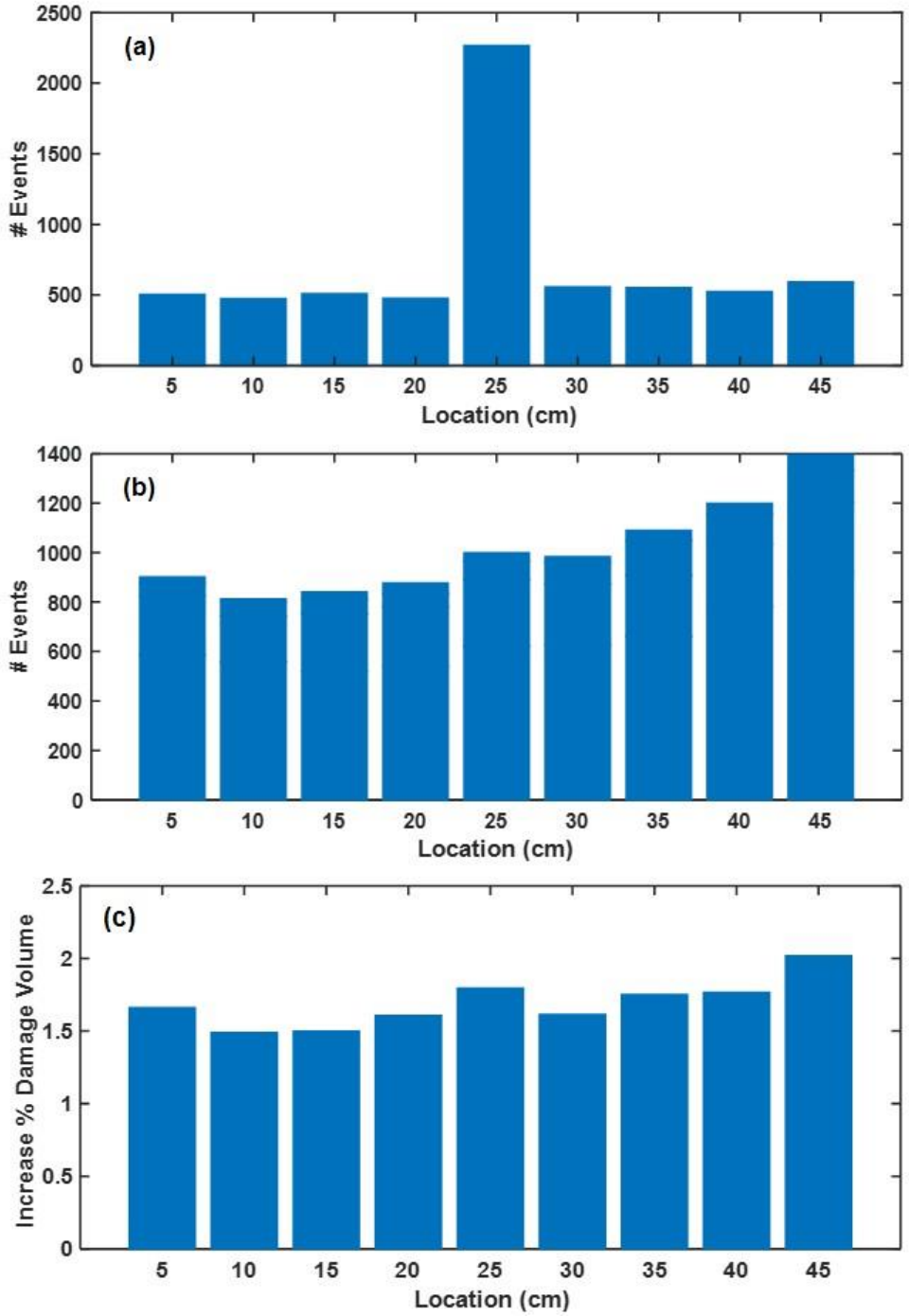

Figure 6.11 (a) Distribution of AE events along the CFRP rebar sample using conventional linear source location method. (b) Distribution of AE events along the CFRP rebar sample using the ANN method. (C) Distribution of the ratio of damage / total sample volume for the CFRP using the µCT scan

6.5.2 µCT Longitudinal Section Images

µCT Image analysis was performed using CTAn software version 1.11.10. Within each 5cm sample a length of 18 mm was selected for analysis. The entire diameter, excluding the coating, was included in the analysis. Figures 6.12 and 6.13 below show some 2D reconstructed images in the x-z plane for the tested GFRP and CFRP size 4 respectively. A µCT image in Figure 6.12a for GFRP sample has small voids at distance of 4 – 6 cm from the sensor. This region has the lowest damage volume in the bar as indicated in Figure 6.10c. The image of the sample taken from 19 – 21 cm, Figure 6.12b, has a larger void volume than sample taken from 4 – 6 cm, as indicated in Figure 6.10c. Figure 6.12c shows more damage represent as a longitudinal debonding, and Figure 6.12d show the more increasing of damage in the longitudinal direction. The AE location results in Figures 6.10a and 6.10b have similar shapes to the µCT results.

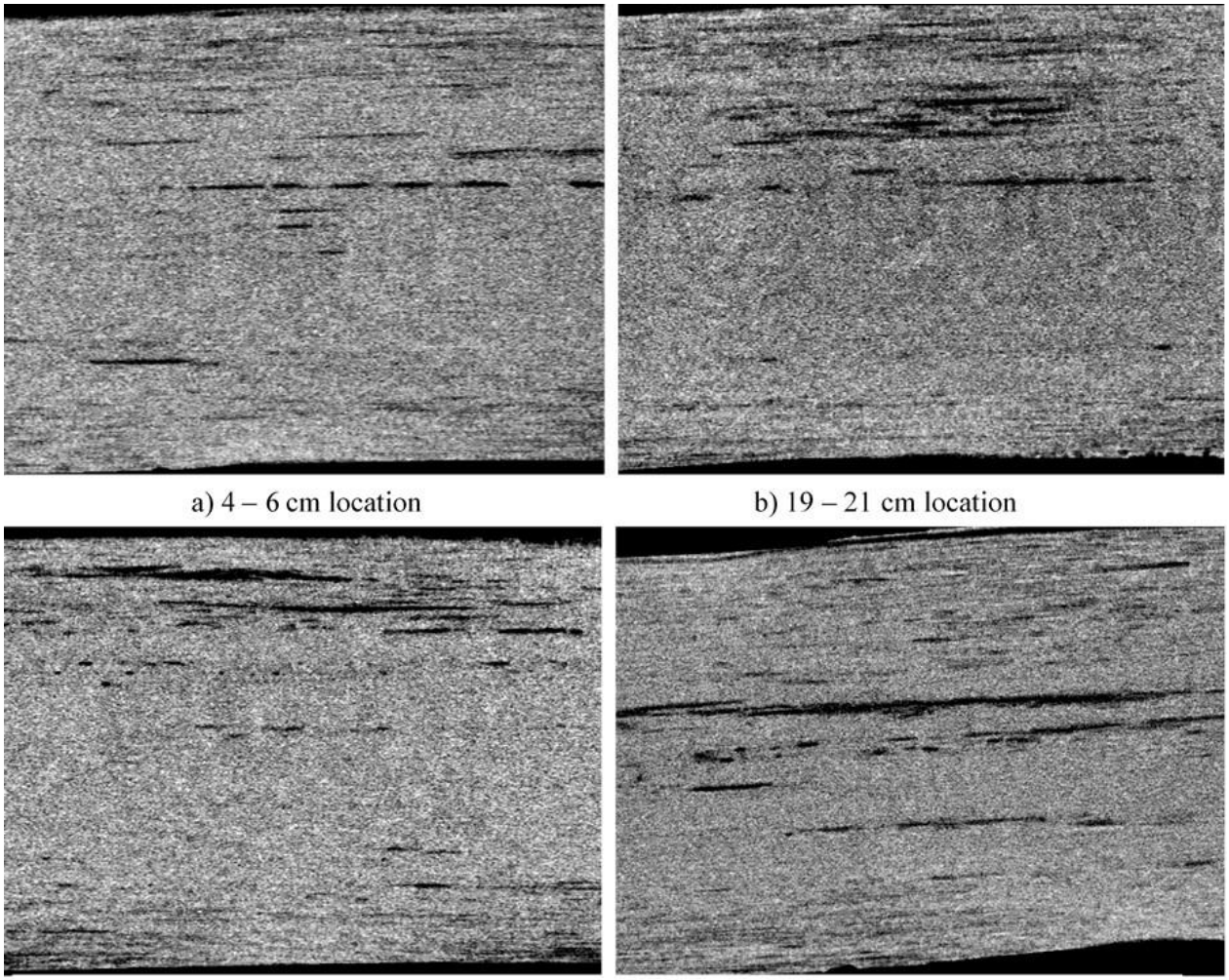

Figure 6.12 2D image slices along the GFRP size 4 sample using µCT

A μCT image for a CFRP sample after load testing is shown in Figure 6.13. In the image of the sample shown in Figure 6.13a, taken from 9 – 11 cm from the sensor, the damaged regions do not appear to be as contiguous as other regions of the bar. This region has the lowest damage volume in the bar as indicated in Figure 6.11c. The image of the sample taken from 19 – 21 cm, Figure 6.13b, shows the damage starts to increase longitudinally. The same increase in damage volume was observed in the ANN location maps presented in Figure 6.11c. Figure 6.13c shows the growth of a longitudinal splitting. Figure 6.13d shows the increasing longitudinal and transverse damage in both directions. The AE source location density results in Figure 6.11c have a similar pattern as the μCT void volume including a maximum in 45 cm location.

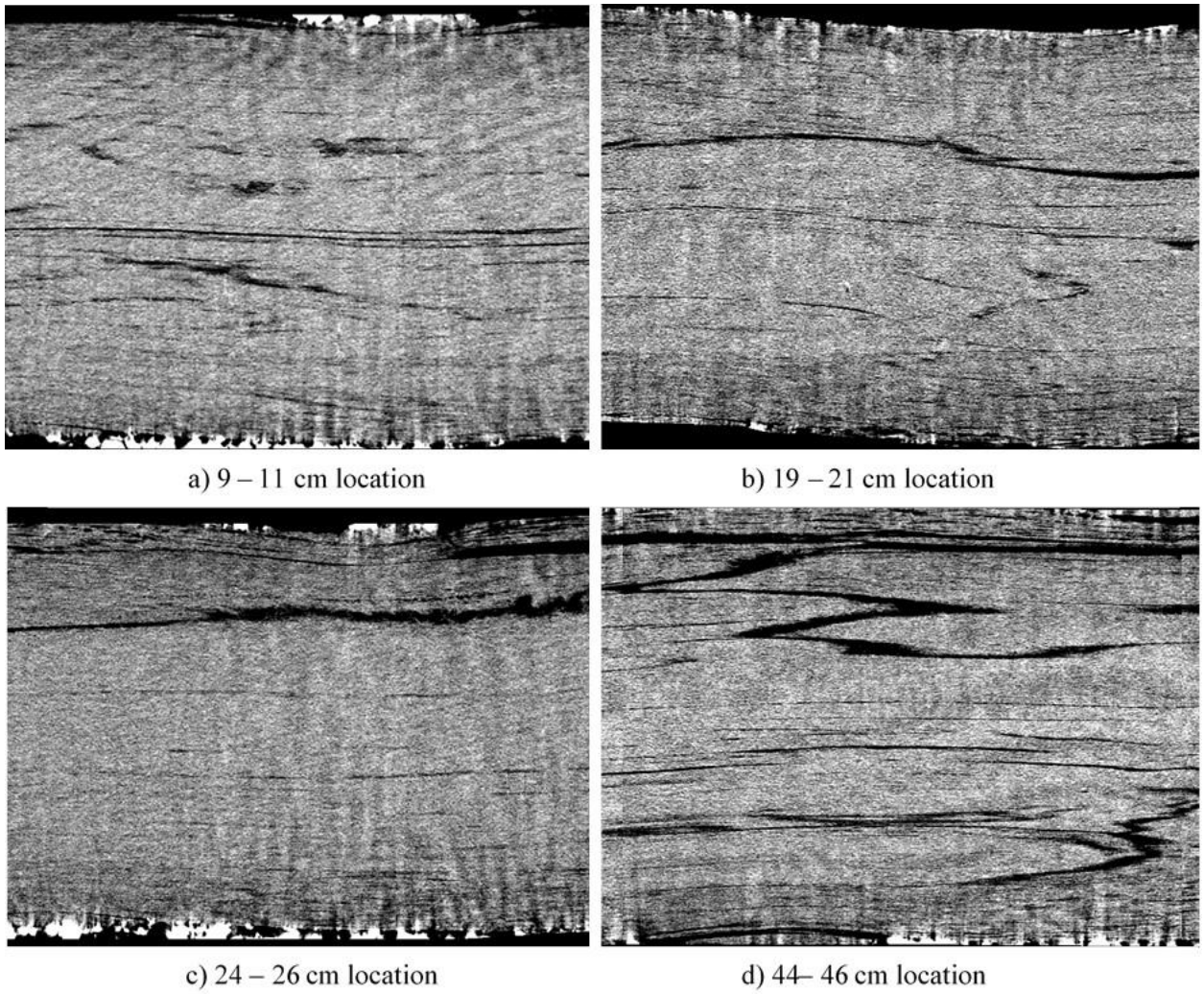

Figure 6.13 2D image slices along the CFRP size 4 sample using µCT

6.6 Comparison Between ANN and RMS with µCT

To quantitatively compare the ANN and RMS with the µCT method, each of the graphs in Figures 6.10 and 6.11 were normalized by dividing the number of events in each location by the sum of all events for the all locations on the rebar as shown in Tables 6.1 and 6.2. The difference between the methods was then determined from the normalized graphs. Figure 6.14 shows the differences of the localized AE events between the RMS and µCT, and the differences between the ANN and µCT for both GFRP and CFRP samples. The figures show better correlation in the localization results for the ANN and µCT methods than the conventional source location by factor of 1.6 and 3 for GFRP and CFRP bar samples respectively.

Table 6.1 Normalized # events using RMS, ANN, and normalized % damage volume using μCT for GFRP size 4 sample

Conventional Arrival Time Using RMS			ANN		μCT			
Position (cm)	**# Events**	**Normalized # Events**	**# Events**	**Normalized # Events**	**% Damage Volume**	**Normalized % Damage Volume**	**RMS-μCT**	**ANN-μCT**
5	56	0.081	63	0.047	0.34	0.041	0.040	0.007
10	60	0.086	98	0.074	0.68	0.082	0.005	-0.008
15	73	0.105	98	0.074	0.66	0.079	0.026	-0.006
20	81	0.117	124	0.093	0.84	0.101	0.016	-0.008
25	104	0.150	175	0.131	1.2	0.144	0.006	-0.012
30	69	0.099	92	0.069	0.46	0.055	0.044	0.014
35	60	0.086	126	0.095	0.78	0.094	-0.007	0.001
40	69	0.099	236	0.177	1.55	0.186	-0.087	-0.009
45	123	0.177	319	0.240	1.83	0.219	-0.042	0.020
Σ	695		1331		8.34			

Table 6.2 Normalized # events using RMS, ANN, and normalized % damage volume using µCT for CFRP size 4 sample

	Conventional Arrival Time Using RMS		ANN		µCT			
Position (cm)	**# Events**	**Normalized # Events**	**# Events**	**Normalized # Events**	**% Damage Volume**	**Normalized % Damage Volume**	**RMS-µCT**	**ANN-µCT**
5	502	0.078	901	0.099	1.659	0.109	-0.031	-0.010
10	472	0.073	812	0.089	1.489	0.098	-0.025	-0.009
15	507	0.079	841	0.092	1.497	0.099	-0.020	-0.006
20	475	0.074	876	0.096	1.607	0.106	-0.032	-0.009
25	2264	0.351	998	0.110	1.794	0.118	0.233	-0.008
30	557	0.086	983	0.108	1.613	0.106	-0.020	0.002
35	552	0.086	1089	0.120	1.75	0.115	-0.030	0.005
40	522	0.081	1198	0.132	1.765	0.116	-0.035	0.016
45	592	0.092	1395	0.153	2.017	0.133	-0.041	0.021
Σ	6443		9093		15.191			

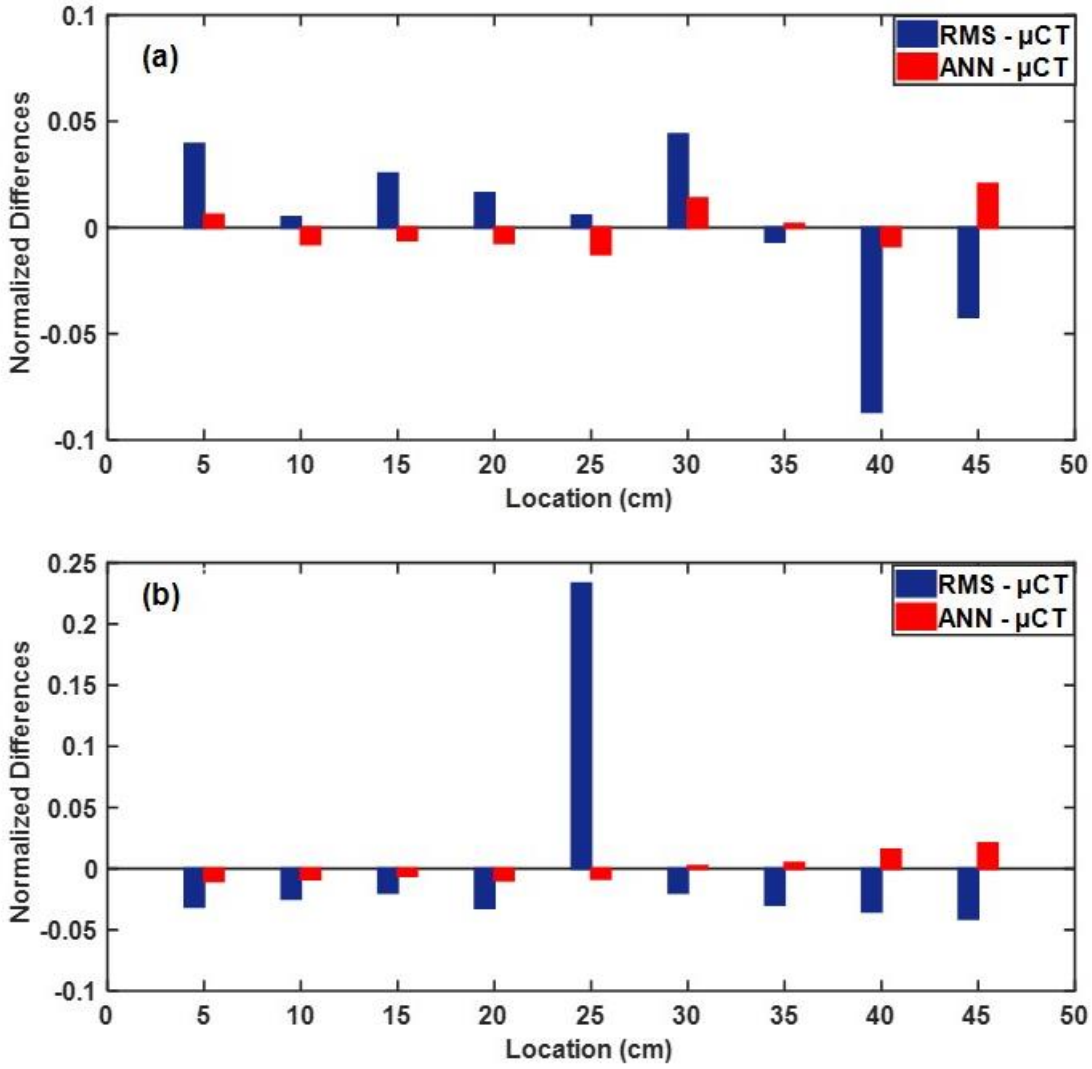

Figure 6.14 The normalized differences between the RMS, ANN source location density and µCT void volume results for: (a) GFRP sample and (b) CFRP sample. To quantitatively compare the ANN and RMS with the µCT method, each of the graphs were normalized by dividing by the sum of all values

CHAPTER 7

SUMMARY, CONCLUSIONS, AND RECOMMENDATION FOR FUTURE WORK

7.1 Summary

In this work, research was done in two phases, experimental and analytical phases. In the experimental phase, different diameters of CFRP and GFRP bar specimens were subjected to tensile loading. The specimens were prepared according to Annex B of CSA S806-12 (2012) standard. Some specimens were loaded until failure and others were loaded up to different stages of the ultimate load (in 10% ultimate load increments) and were used for SEM and µCT investigation. Two rebars were tested under load – unload – reload in 10% increments up to failure to estimate the wave velocity in CFRP and GFRP. AE signals generated from damage were detected by two piezoelectric transducers that were attached to the surface of the specimens' anchorage.

In the analytical phase, MATLAB was used for analysis of AE signals and SEM images, and CTAn software was used for analysis of µCT Images. The AE signals were analyzed using the RMS AE hit detection algorithm, and then parameters were extracted in time and time – frequency domain. The parameters that were extracted in time domain are: amplitude, cumulative events, duration, energy, rise time, number of counts, cumulative counts, average frequency, and frequency peak. In time frequency domain, STFT was used to calculate the energy and FFT for both GFRP and CFRP rebar samples.

For a comparison between ANN and conventional linear source location, AE signals were analyzed using threshold method as well. For μCT analysis, 3D and 2D – μCT reconstructed images were used to calculate the void volume and its distribution. In this work the void volume was used as a measure of damage.

7.2 Conclusions

1. The results of twenty FRP bar specimens that were loaded up to 90 – 100% ultimate load showed that AE parameters changed as the quasi static load on the bar was increased. FRP is a linear elastic material and the stress-strain curves were linear until failure and did not show any indication of increase in damage with load.

2. In previous work, the observed changes in AE parameters, similar to those reported in this work, have been correlated with the occurrence of different damage mechanisms in FRP materials. With pultruded FRP bars, AE signals with high amplitude and duration occur more frequently as the load approaches the ultimate load, while the low to medium amplitude signals appeared throughout the testing period. The RA and AF also showed some correlation with the increasing the slope of cumulative counts curve. In CFRP, the increasing of RA and decreasing of AF refers to the elongation in the matrix. In GFRP, the decreasing of RA and increasing of AF refers to the delaminating of the outside layer. Moreover, AE signals generated from CFRP bars have a shorter duration than GFRP bars. The mean values were equal to 16.16 milliseconds during the last third of the test time for

CFRP bars, and 20.24 milliseconds for GFRP bar. CFRP bars have higher amplitude signals than GFRP. Specifically, the ratio of high to the sum of low and medium amplitude events is 4% for CFRP size 2, 6% for CFRP size 4, and 1% for both GFRP size 4 and 6. In addition, frequency peaks were obtained using STFT and energy distribution. Most AE signals have more than one frequency band, which indicates that different damage mechanisms occurred at the same time of the real-time testing. These peaks are limited to the sensitivity of the resonant transducer, R15I-AST of 80 – 200 kHz frequency range.

3. SEM investigation revealed three types of damage in the longitudinal sections: matrix cracking that started from the voids and developed at the same direction of the fibers, debonding, and fiber fracture. On the other hand, the transverse sections did not show any transverse matrix cracking; just the enlargement of the voids which indicate that the matrix cracking occurred at regions between voids. In contrast, AE analysis revealed different number of events for different specimens of the same type of FRP bar, and that is due to different void volume fraction that was observed under SEM investigation. This work contributes to better understanding the behaviour of these bars.

4. The experimental results from the AE monitoring system could be used to identify different stages of internal damage of the specimens related to micro – crack propagation and the failure of FRP bars. The results also confirmed that the slope of the cumulative counts increases with increasing load. However, the large variation of the absolute number of events at failure make it a poor metric to predict when FRP bars will fail. Furthermore,

the time-frequency characteristics determined from different signal amplitudes are different and may be performed for different damage identification.

5. μCT scan proved to be an appropriate method to investigate the internal damage and its distribution along FRP specimen subjected to tension loads. The determination of the void ratio is an appropriate method to quantitatively evaluate FRP rebars internal damage when subjected to tensile load. The results of cumulative energy from tension test experiments indicated a strong correlation with the percentage void volume obtained from μCT results. The cumulative energy of FFT acoustic emission events was shown to be proportional to the percentage void volume accumulation in FRP rebars.

6. μCT results show that the percentage void volume for CFRP rebars decreases with bar diameter. For GFRP rebars however this trend is not valid for loads exceeding 50% of ultimate. It can be concluded from the 3D analysis that the thickness and length of voids, present after the pultrusion process, increased as damage progressed. In CFRP, voids are growing in thickness as damage progresses. However, GFRP size 6 shows a smaller increase in void thickness and volume as damage progresses, but has a higher initial void thickness than CFRP.

7. The analysis of FRP rebars by μCT opens up the possibility of tracking changes in the internal structure of FRP rebars as a result of tensile loading that may play a significant role in determining the long-term durability of the rebars.

8. AE source locations have been determined using conventional linear source location and ANN methods. The velocity of AE waves and Modulus of Elasticity kept constant as the damage accumulated. A study of 164 AE events for GFRP size 4 and 71 AE events for CFRP size 4 the use of an ANN method provided a better estimation of source location over the conventional linear method in training a data obtained from PLB test. Standard deviation for GFRP sample was 1.95 cm using ANN method versus 8.43 cm and 7.75 cm using conventional linear source location for both RMS and threshold based algorithms respectively. Standard deviation for CFRP sample was 1.48 cm using ANN method versus 7.84 cm and 7.51 cm using conventional linear source location for both RMS and threshold based algorithms.

9. Analysis of the AE results from a tension test on GFRP and CFRP rebars using the neural network trained on the PLB results reduced the number of times that source locations were predicted to be outside the free length of the sample. For ANN method, 48% and 30% of the AE events in GFRP and CFRP samples were considered as outlier events. For conventional method, 82% and 65% of the AE events in GFRP and CFRP samples were considered as outlier events. In addition, the trained ANN predicted source location densities that were better correlated with the μCT analysis than the conventional source location methods by factor of 1.6 and 3 for GFRP and CFRP samples respectively. GFRP sample showed stronger correlation than CFRP sample with the μCT analysis.

10 AE characterestucs are useful in setting a in setting a data based criterion for monitoring FRP rebars.

11 The analysis of FRP bars by μCT method may be used to estimate the quality and consistency of pultruded FRP bars. It allows the manufacturers to track changes during manufacturing process such as continuous voids or micro cracks that generated during the thermal stresses.

7.3 Recommendations for Future Work

- Develop a failure warning system for relating the AE parameters to the impending failure and to particular faiure mechanisms in an FRP tendon.
- Develop multi channel systems which will be capable of predicting failure in a number of bars undergoing prestress in the precast plant, and triggering an alarm if a rupture is expected to occur.
- Evaluate the damage propagation using Felicity and Kaiser effects.
- AE technique should be further investigated for concrete structures that are reinforced with FRP bars with the using of sensors attached to the bar and embedded in the concrete.
- The μCT scanning would be further investigated on untested samples as another method for establishing a standard to assess the integrity of untested FRP bars.
- Testing concrete reinforced with FRP bars and subjected to increased or sustained loads to study the impact of the increasing voids on the bond of FRP bars with the surrounding concrete.

- Check the performance of the ANN method to predict the source location for a concrete structure that is reinforced with FRP rebars by using the two-dimentional source location.

References

ACI Committee 440. (2006). "Guide for The Design and Construction of Concrete Reinforced with FRP Bars." ACI 440.1R-06, American Concrete Institute, Farmington Hills, MI.

Aggelis, D. G. (2011). "Classification of cracking mode in concrete by acoustic emission parameters." *Mechanics Research Communications*, 38(3), 153–157.

Aggelis, D. G., Barkoula, N. M., Matikas, T. E., and Paipetis, A. S. (2010). "Acoustic emission monitoring of degradation of cross ply laminates." *The Journal of the Acoustical Society of America*, 127(6), EL246-EL251.

Aggelis, D. G., Soulioti, D. V., Sapouridis, N., Barkoula, N. M., Paipetis, A. S., and Matikas, T. E. (2011). "Acoustic emission characterization of the fracture process in fibre reinforced concrete." *Construction and Building Materials*, 25(11), 4126–4131.

Akaike, H. (1974). "Markovian representation of stochastic processes and its application to the analysis of autoregressive moving average processes." *Ann Inst Stat Math*, 26, 363–387.

Al-Jumaili, S. K., Pearson, M. R., Holford, K. M., Eaton, M. J., and Pullin, R. (2016). "Acoustic emission source location in complex structures using full automatic delta T mapping technique." *Mechanical Systems and Signal Processing*, 72–73, 513–524.

Alampalli, S., and Ettouney, M. M. (2013). "Structural Health Monitoring." *The International Handbook of FRP Composites in civil Engineering*, M. Zoghi, ed., 559–572.

Anastassopoulos, A. A., and Philippidis, T. P. (1995). "Clustering methodology for the

evaluation of acoustic emission from composites." *Journal of acoustic emission*, 13(1–2), 11–22.

Arthur, D., and Vassilvitskii, S. (2007). "k-means++: the advantages of careful seeding." *Proceedings of the eighteenth annual ACM-SIAM symposium on Discrete algorithms*, 1027–1025.

ASM International Handbook Committee. (1989). *ASM Handbook, Volume 17 - Nondestructive Evaluation and Quality Control*. ASM International. ASTM E1316. (2006). "Standard Terminology for Non-Destructive Examinations." American Standard for Testing and Materials.

ASTM F1430. (2005). "Standard Test Method for Acoustic Emission Testing of Insulated and Non Insulated Aerial Personnel Devices with Supplemental Load Handling Attachments." American Standard for Testing and Materials.

Ativitavas, N., Fowler, T. J., and Pothisiri, T. (2004). "Identification of fiber breakage in fiber reinforced plastic by low-amplitude filtering of acoustic emission data." *Journal of Nondestructive Evaluation*, 23(1), 21–36.

Awaja, F., and Arhatari, B. D. (2009). "X-ray Micro Computed Tomography investigation of accelerated thermal degradation of epoxy resin/glass microsphere syntactic foam." *Composites Part A: Applied Science and Manufacturing*, 40(8), 1217–1222.

Awaja, F., Arhatari, B., Wiesauer, K., Leiss, E., and Stifter, D. (2009). "An investigation of the accelerated thermal degradation of different epoxy resin composites using X-ray microcomputed tomography and optical coherence tomography." *Polymer Degradation and Stability*, 94(10), 1814–1824.

Awaja, F., Nguyen, M. T., Zhang, S., and Arhatari, B. (2011). "The investigation of inner

structural damage of UV and heat degraded polymer composites using X-ray micro CT." *Composites Part A: Applied Science and Manufacturing*, 42(4), 408–418.

Bai, F., Gagar, D., Foote, P., and Zhao, Y. (2017). "Comparison of alternatives to amplitude thresholding for onset detection of acoustic emission signals." *Mechanical Systems and Signal Processing*, 84, 717–730.

Bakht, B., and Mufti, A. (2015). "Fibre Reinforced Bridges." *Bridges analysis, Design, Structural Health Monitoring, and Rehabilitation*, Springer, Switzerland, 271 – 291.

Balaguru, P., Nanni, A., and James, G. (2008). *FRP Composites for Reinforced and Prestressed Concrete Structures:A Guide to Fundamentals and Design for Repair and Retrofit*. CRC Press.

Barré, S., and Benzeggagh, M. L. (1994). "On the use of acoustic emission to investigate damage mechanisms in glass-fibre-reinforced polypropylene." *Composites Science and Technology*, 52(3), 369–376.

Bhat, M. R., Majeed, M. A., and Murthy, C. R. L. (1994). "Characterization of fatigue damage in unidirectional GFRP composites through acoustic emission signal analysis." *NDT and E International*, 27(1), 27–32.

Bohse, J. (2000). "Acoustic emission characteristics of micro-failure processes in polymer blends and composites." *Composites Science and Technology*, 60, 1213–1226.

Brothers, H. (2011a). *Carbon Fiber Reinforced Polymer (CFRP) Bar - Aslan 200 series*.

Brothers, H. (2011b). *Glass Fiber Reinforced Polymer (GFRP) Rebar - Aslan 100 series*.

Busel, J. P. (2016). "Introduction to Fiber Reinforced Polymer (FRP) Composites In Infrastructure." *American Composites Manufacturers Association (ACMA)*, Arlington, 72.

Canadian Standards Association (CSA). (2012). *Design and Construction of Building structures with Fibre-Reinforced Polymer, CAN/CSA S806-12. Canadian Standards Association*. Ontario, Canada

Caprino, G., Lopresto, V., Leone, C., and Papa, I. (2011). "Acoustic Emission Source Location in Unidirectional Carbon-Fiber-Reinforced Plastic Plates with Virtually Trained Artificial Neural Networks." *Journal of Applied polymer Science*, 122(6), 3506–3513.

CARP. (1999). "Recommended Practice for Acoustic Emission Evaluation of Fiber Reinforced Plastic (FRP) Tanks and Pressure Vessels." The Committee on Acoustic Emission for Reinforced Plastics (CARP), A Division of the Technical Council of The American Society for Nondestructive Testing, Inc, Columbus, Ohio.

Chang, P. C., Flatau, A., and Liu, S. C. (2003). "Review paper: Health monitoring of civil infrastructure." *Structural Health Monitoring*, 2(3), 257–267.

Chang, P. C., and Liu, S. C. (2003). "Recent Research in Nondestructive Evaluation of Civil Infrastructures." *Journal of Materials in Civil Engineering*, 15(3), 298–304.

Chen, H. L., Sami, Z., and GangaRao, H. V. (1993). "Identifying damages in stressed aramid FRP bars using acoustic emission.''." *Dynamic characterization of advanced materials*, 172, 171–178.

Chiewanichakorn, M., Aj, A., and Alampalli, S. (2012). "Failure Analysis of Fiber-Reinforced Polymer Bridge Deck System." *Journal of Composites, Technology and Research*, 25(2), 1–9.

Cole, T. A., Lopez, M., and Ziehl, P. H. (2006). "Fatigue behavior and nondestructive evaluation of full-scale FRP honeycomb bridge specimen." *ASCE Journal of Bridge*

Engineering, 11(4), 420–429.

Colombo, S., Forde, M. C., Main, I. G., Halliday, J., and Shigeishi, M. (2005). "AE energy analysis on concrete bridge beams." *Materials and Structures*, 38(283), 851–856.

Crump, T. N. (1981). "Acceptance criteria for acoustic emission testing of FRP tanks." *SPI/CARP Meeting Paper*, Atlanta, Georgia.

Czichos, H. (Ed.). (2013). *Handbook of Technical Diagnostics: Fundamentals and Application to Structures and Systems*. Springer Heidelberg, New York Dordrecht London.

Daubechies, I. (1990). "The wavelet transform, time-frequency localization and signal analysis." *Information Theory, IEEE Transactions on*, 36(5), 961–1005.

Degala, S., Rizzo, P., Ramanathan, K., and Harries, K. A. (2009). "Acoustic emission monitoring of CFRP reinforced concrete slabs." *Construction and Building Materials*, 23(5), 2016–2026.

Dehghan Niri, E., and Salamone, S. (2012). "A probabilistic framework for acoustic emission source localization in plate-like structures." *Smart Materials and Structures*, 21(3), p.035009 (16pp).

Demuth, H., Beale, M., and Hagan, M. (2009). *Neural Network Toolbox ™ 6 User ' s Guide*. MaATLAB, *The MathWorks. Inc*.

Deng, L., and Cai, C. S. (2007). "Applications of fiber optic sensors in civil engineering." *Structural Engineering and Mechanics*, 25(5), 577–596.

Desplentere, F., Lomov, S. V., Woerdeman, D. L., Verpoest, I., Wevers, M., and Bogdanovich, A. (2005). "Micro-CT characterization of variability in 3D textile architecture." *Composites Science and Technology*, 65(13), 1920–1930.

Dowla, F. U., Taylor, S. R., and Anderson, R. W. (1990). “Seismic discrimination with artificial neural networks: Preliminary results with regional spectral data.” *Bulletin of the Seismological …*, 80(5), 1346–1373.

Drummond, G., Watson, J. F., and Acarnley, P. P. (2007). “Acoustic emission from wire ropes during proof load and fatigue testing.” *NDT and E International*, 40(1), 94–101.

Dry, C. (1996). “Procedures developed for self-repair of polymer matrix composite materials.” *Composite Structures*, 35(3), 263–269.

ElBatanouny, M. K., Larosche, A., Mazzoleni, P., Ziehl, P. H., Matta, F., and Zappa, E. (2014). “Identification of Cracking Mechanisms in Scaled FRP Reinforced Concrete Beams using Acoustic Emission.” *Experimental Mechanics*, 54(1), 69–82.

Elgabbas, F., Ahmed, E. A., and Benmokrane, B. (2015). “Physical and mechanical characteristics of new basalt-FRP bars for reinforcing concrete structures.” *Construction and Building Materials*, 95, 623–635.

Ely, T. M., and Hill, E. V. K. (1992). “Characterization of failure mechanisms in graphite/epoxy tensile test specimens using acoustic emission data.” *Forth International Symposium on Acoustic Emission from Composite Materials AECM-4*, Seattle, WA, 187–199.

Ely, T. M., and Hill, E. K. (1995). “Longitudinal splitting and fibre breakage characterization in graphite/epoxy using acoustic emission data.” *Materials Evaluation*, 53(2), 288–294.

Ettouney, M. M., and Alampall, S. (2011). *Infrastructure Health in Civil Engineering Application and management*. CRC Press; London, Taylor & Francis Group.

Fowler, T. J. (1988). “Acoustic Emission Testing of Vessels.” *Chemical Engineering*

Progress, 84(9), 59–70.

Fu, T., Zhang, Z., Liu, Y., and Leng, J. (2015). "Development of an artificial neural network for source localization using a fiber optic acoustic emission sensor array." *Structural Health Monitoring*, 14(2), 168–177.

Fuwa, M., Harris, B., and Bunsell, A. R. (1975). "Acoustic Emission During Cyclic Loading of Carbon-Fibre-Reinforced Plastics." *Journal or Physics D: Applied Physics*, 8(13), 1460–1471.

Gholizadeh, S. (2016). "A review of non-destructive testing methods of composite materials." *Procedia Structural Integrity*, 1, 50–57.

GI-MR. (2009). "Guidelines on use OF Acoustic Emission Technique (AET) on Railway Bridges." (Government of India. Ministry of Railways).

Godin, N., Huguet, S., and Gaertner, R. (2005). "Integration of the Kohonen's self-organising map and k-means algorithm for the segmentation of the AE data collected during tensile tests on cross-ply composites." *NDT and E International*, 38(4), 299–309.

Golaski, L., Gebski, P., and Ono, K. (2002). "Diagnostics of reinforced concrete birdges by acoustic emission." *Journal of Acoustic Emission*, 20, 83–98.

Gostautas, R. S., Ramirez, G., Peterman, R. J., and Meggers, D. (2005). "Acoustic Emission Monitoring and Analysis of Glass Fiber-Reinforced Composites Bridge Decks." *ASCE, Journal of Bridge Engineering*, 10(6), 713.

de Groot, P. J., Wijnen, P. A. M., and Janssen, R. B. F. (1995). "Real-time frequency determination of acoustic emission for different fracture mechanisms in carbon/epoxy composites." *Composites Science and Technology*, 55(4), 405–412.

Grosse, C., and Ohtsu, M. (Eds.). (2008). *Acoustic Emission Testing: Basics for Research*. Springer, Verlag Berlin Heidelberg.

Gutkin, R., Green, C. J., Vangrattanachai, S., Pinho, S. T., Robinson, P., and Curtis, P. T. (2011). "On acoustic emission for failure investigation in CFRP: Pattern recognition and peak frequency analyses." *Mechanical Systems and Signal Processing*, Elsevier, 25(4), 1393–1407.

Hamstad, M. a., O'Gallagher, a., and Gary, J. (2002). "A Wavelet Transform Applied To Acoustic Emission Signals: Part 1: Source Identification." *Journal of Acoustic Emission*, 20(853), 39–61.

Hildebrand, T., and Rüegsegger, P. (1997). "A new method for the model-independent assessment of thickness in three-dimensional images." *Journal of Microscopy*, 185(1), 67–75.

Holford, K. M., Davies, A. W., Pullin, R., and Carter, D. C. (2001). "Damage Location in Steel Bridges by Acoustic Emission." *J. Intel. Mat. Syst. Str.*, 12(8), 567–576.

Iwamoto, M., Ni, Q.-Q., Fujiwara, T., and Kurashiki, K. (1999). "Intralaminar fracture mechanism in unidirectional CFRP composites: Part I: Intralaminar toughness and AE characteristics." *Engineering Fracture Mechanics*, 64(6), 721–745.

Kalafat, S., and Sause, M. G. (2015). "Acoustic emission source localization by artificial neural networks." *Structural Health Monitoring: An International Journal*, 14(6), 633–647.

Kamala, G., Hashemi, J., and Barhorst, A. A. (2001). "Discrete-Wavelet Analysis of Acoustic Emissions During Fatigue Loading of Carbon Fiber Reinforced Composites." *Journal of Reinforced Plastics and Composites*, 20(3), 222–238.

Kaphle, M.,Tan, A., Thambiratnam, D. P., and Chan, T. H. T. (2011). “Study of acoustic emission data analysis tools for structural health monitoring applications.”*Journal of Acoustic Emission*, 29(November), 243–250.

Kaphle, M., Tan, A. C. C., Thambiratnam, D. P., and Chan, T. H. T. (2012a). “Identification of acoustic emission wave modes for accurate source location in plate-like structures.” *Structural Control and Health Monitoring*, 19(2), 187–198.

Kaphle, M., Tan, A., Thambiratnam, D., and Chan, T. (2012b). “Effective Discrimination of Acoustic Emission Source Signals for Structural Health Monitoring.” *Advances in Structural Engineering*, 15(5), 707–716.

Komai, K., Minoshima, K., and Shibutani, T. (1991). “Investigation of the fracture mechanism of carbon/epoxy composites by AE signal analysis.” *JSME International Journal*, 34(1), 381–388.

Kopeliovich, D. (2012). “Substances and Technologies.” *ANTECH, Computer Services Inc.*

Li, H., Huang, Y., Chen, W. L., Ma, M. L., Tao, D. W., and Ou, J. P. (2011). “Estimation and warning of fatigue damage of FRP stay cables based on acoustic emission techniques and fractal theory.” *Computer-Aided Civil and Infrastructure Engineering*, 26(7), 500–512.

Li, W., Ho, S. C. M., Patil, D., and Song, G. (2017). “Acoustic emission monitoring and finite element analysis of debonding in fiber-reinforced polymer rebar reinforced concrete.” *Structural Health Monitoring: An International Journal*, 16(6), 674–681.

Li, W., Kong, Q., Ho, S. C. M., Lim, I., Mo, Y. L., and Song, G. (2016). “Feasibility study of using smart aggregates as embedded acoustic emission sensors for health

monitoring of concrete structures." *Smart Materials and Structures*, 25(11).

Liang, Y., Sun, C., and Ansari, F. (2004). "Acoustic Emission Characterization of Damage in Hybrid Fiber-Reinforced Polymer Rods." *Journal of Composites for Construction*, 8(1), 70–78.

Liang, Y., Sun, C., and Ansari, F. (2011). "Damage Assessment and Ductility Evaluation of Post Tensioned Beams with Hybrid FRP Tendons." *Journal of Composites for Construction*, (June), 274–283.

Mahal, M. S. M., (2015) "Fatigue Behaviour of RC beams Strengthened with CFRP Analytical and Experimental investigations." Doctoral Thesis, Luleå University of Technology, SWEDEN

Maillet, E., Godin, N., R'Mili, M., Reynaud, P., Fantozzi, G., and Lamon, J. (2014). "Real-time evaluation of energy attenuation: A novel approach to acoustic emission analysis for damage monitoring of ceramic matrix composites." *Journal of the European Ceramic Society*, 34(7), 1673–1679.

Mallat, S. G. (2009). *A Wavelet Tour of Signal Processing: The Sparse Way*. Amsterdam; Boston: Elsevier

Mathworks. (2009). "MATLAB Users Guide." Natick, MA.

Matt, H. M., and Di Scalea, F. L. (2007). "Macro-fiber composite piezoelectric rosettes for acoustic source location in complex structures." *Smart Materials and Structures*, 16(4), 1489–1499.

Md Nor, N., Muhamad Bunnori, N., Ibrahim, A., Mohd Saman, H., Shahidan, S., and Mat Saliah, S. N. (2013). "An investigation of an acoustic wave velocity in a reinforced concrete beam from out-of plane and in plane sources." *Modeling and Measurement*

Methods for Acoustic Waves and for Acoustic Microdevices, 171–188.

Melbourne, C., and Tomor, A. K. (2006). "Application of acoustic emission for masonry arch bridges." *Strain*, 42(3), 165–172.

Miller, R. K., and McIntire, P. (1987). *Nondestructive Testing Handbook, vol. 5, Acoustic Emission Testing,"*. *American Society for Nondestructive Testing*, Columbus, Ohio.

Mirmiran, A., and Philip, S. (2000). "Comparison of acoustic emission activity in steel-reinforced and FRP-reinforced concrete beams." *Construction and Building Materials*, 14(6–7), 299–310.

Murakami, Y., and Yuyama, S. (1996). "Acoustic emission evaluation of structural integrity in reinforced concrete beams due to corrosion of reinforcement." *Proc. 13th Inter. AE Symp, Nara Japan*, 217–244.

NDT resource Center. (2014). "Theory - AE Sources: In Acoustic Emission." *Retreived from https://www.nde-ed.org*.

Nguyen, B. N., Tucker, B. J., and Khaleel, M. A. (2005). "A Mechanistic Approach to Matrix Cracking Coupled With Fiber–Matrix Debonding in Short-Fiber Composites." *Journal of Engineering Materials and Technology*, 127(3), 337.

Nunes, J. P., Pouzada, A. S., and Bernardo, C. A. (2002). "The use of a three-point support flexural test to predict the stiffness of anisotropic composite plates in bending." *Polymer Testing*, 21(7), 853.

Ohno, K., and Ohtsu, M. (2010). "Crack classification in concrete based on acoustic emission." *Construction and Building Materials*, 24(12), 2339–2346.

Ohtsu, M. (2008). *Acoustic Emission Testing: Basics for Research - Applications in Civil Engineering*. (C. U. Gross and M. Ohtsu, eds.), Springer, Verlag Berlin Heidelberg.

Ohtsu, M., Isoda, T., and Tomoda, Y. (2007). “Acoustic Emission Techniques Standardized for Concrete Structures.” *Journal of Acoustic Emission*, 25, 21–32.

Ohtsu, M., Uchida, M., Okamoto, T., and Yuyama, S. (2002). “Damage assessment of reinforced concrete beams qualified by acoustic emission.” *ACI Structural Journal*, 99(4), 411–417.

de Oliveira, R., and Marques, A. T. (2008). “Health monitoring of FRP using acoustic emission and artificial neural networks.” *Computers and Structures*, 86(3–5), 367–373.

Ono, K., and Huang, Q. (1994). “Pattern recognition analysis of acoustic emission signals.” *Progress in Acoustic Emission VII. Proc. of the 12th International Acoustic Emission Symposium*, 69–78.

Ozevin, D., Greve, D. W., Oppenheim, I. J., and Pessiki, S. (2004). “Resonant type MEMS transducers excited by two acoustic emission simulation techniques.” *Proceedings of SPIE - The International Society for Optical Engineering*, 5391, 239–249.

Pang, J. W. C., and Bond, I. P. (2005). “A hollow fibre reinforced polymer composite encompassing self-healing and enhanced damage visibility.” *Composites Science and Technology*, 65(11–12), 1791–1799.

Prosser, W. H. (2002). *Nondestructive Evaluation Theory, Techniques, and Applications: Acoustic Emission*. *Mechanical Engineering*, (P. J. Shull, ed.), New York: Marcel Dekker.

Prosser, W. H., Jackson, K. E., Kellas, S., Smith, B. T., Mckeon, J., and Friedman, A. (1995). “Advanced Waveform-Based Acoustic Emission Detection of Matrix Cracking in Composites.” *Materials Evaluation*, 53(9), 1052–1058.

Ramirez-Jimenez, C. R., Papadakis, N., Reynolds, N., Gan, T. H., Purnell, P., and Pharaoh, M. (2004). “Identification of failure modes in glass/polypropylene composites by means of the primary frequency content of the acoustic emission event.” *Composites Science and Technology*, 64(12), 1819–1827.

Remy, E., and Thiel, E. (2002). “Medial axis for chamfer distances: Computing look-up tables and neighbourhoods in 2D or 3D.” *Pattern Recognition Letters*, 23(6), 649–661.

Rizzo, P., and di Scalea, F.L. (2001). “Acoustic emission monitoring of carbon-fiber-reinforced-polymer bridge stay cables in large-scale testing.” *Experimental Mechanics.*, 41(3), 282–290.

Romhány, G., Czigány, T., and Karger-Kocsis, J. (2017). “Failure Assessment and Evaluation of Damage Development and Crack Growth in Polymer Composites Via Localization of Acoustic Emission Events: A Review.” *Polymer Reviews*, 57(3), 397-439.

Rose, J. L., and Nagy, P. B. (2000). “Ultrasonic Waves in Solid Media.” *The Journal of the Acoustical Society of America*, 107(4), 1807–1808.

Rouchier, S., Foray, G., Godin, N., Woloszyn, M., and Roux, J. J. (2013). “Damage monitoring in fibre reinforced mortar by combined digital image correlation and acoustic emission.” *Construction and Building Materials*, 38, 371–380.

Russell, S., and Henneke, E. (1977). "Signature analysis of acoustic emission from graphite/ epoxy composites." *NASA-CR*

De Santis, S., and Tomor, A. K. (2013). “Laboratory and field studies on the use of acoustic emission for masonry bridges.” *NDT & E International*, 55, 64–74.

Sawpan, M. A., Mamun, A. A., Holdsworth, P. G., and Renshaw, P. (2013). “Quasi-static and dynamic mechanical elastic moduli of alkaline aged pultruded fibre reinforced polymer composite rebar.” *Materials and Design*, 46, 277–284.

Schell, J. S. U., Renggli, M., van Lenthe, G. H., M??ller, R., and Ermanni, P. (2006). “Micro-computed tomography determination of glass fibre reinforced polymer meso-structure.” *Composites Science and Technology*, 66(13), 2016–2022.

Schilling, P. J., Karedla, B. R., Tatiparthi, A. K., Verges, M. a., and Herrington, P. D. (2005). “X-ray computed microtomography of internal damage in fiber reinforced polymer matrix composites.” *Composites Science and Technology*, 65(14), 2071–2078.

Scruby, C. B. (1987). “An introduction to acoustic emission.” *Journal of Physics E: Scientific Instruments*, 20(8), 946–953.

Shanmuganathan, S., and Samarasinghe, S. (2016). *Artificial Neural Network Modelling*. *Studies in Computational Intelligence*, Springer International Publishing, Cham.

Shateri, M., Ghaib, M., Svecova, D., and Thomson, D. (2017). “On acoustic emission for damage detection and failure prediction in fiber reinforced polymer rods using pattern recognition analysis.” *Smart Materials and Structures*, 26(6), 1–24.

Shigeishi, M., Colombo, S., Broughton, K. J., Rutledge, H., Batchelor, A. J., and Forde, M. C. (2001). “Acoustic emission to assess and monitor the integrity of bridges.” *Construction and Building Materials*, 15(1), 35–49.

Siegmann, A., and Kander, R. G. (1992). “In-Situ Acoustic Emission Monitoring During Electron Microscopy of a Model Composite System.” *Polymer Composites*, 13(2),108-120.

Sison, M., Duke, J. C., Lozev, M. G., and Clemeña, G. G. (1998). "Analysis of acoustic emissions from a steel bridge hanger." *Research in Nondestructive Evaluation*, 10(3), 123–145.

Soulioti, D., Barkoula, N. M., Paipetis, A., Matikas, T. E., Shiotani, T., and Aggelis, D. G. (2009). "Acoustic emission behavior of steel fibre reinforced concrete under bending." *Construction and Building Materials*, 23(12), 3532–3536.

Stock, S. R. (1999). "X-ray microtomography of materials." *International Materials Reviews*, 44(4), 141–164.

Stock, S. R. (2008). "Recent advances in X-ray microtomography applied to materials." *International Materials Reviews*, 53(3), 129–181.

Strongwell (2018). "The pultrussion process." *Strongwell Corporation*, Retreived from http://www.strongwell.com/about/the-pultrusion-process/

Sudha, J., Sampathkumar, S., and Kumar, R. K. (2011). "Condition monitoring of delamination during drilling of GFRP composites using the acoustic emission technique – a neural network model." *Insight - Non-Destructive Testing and Condition Monitoring*, 53(8), 445–449.

Surgeon, M., and Wevers, M. (1999). "Modal analysis of acoustic emission signals from CFRP laminates." *NDT & E International*, 32(6), 311–322.

Suziki, M., Nakanishi, H., Iwamoto, M., and Jinen, E. (1988). "Application of static fracture mechanisms to fatigue fracture behaviour of class A-SMC composite." *Proc. 4th Japan-US Conferece on composite materials*, 297–306.

Suzuki, T., and Ohtsu, M. (2005). "Practical application of water-leaked pipeline by AE parameter analysis." *3rd US-japan Sym. on Advancing Applications and Capabilities*

in NDEASTM, Hawaii, 202–208.

Unnþórsson, R. (2008). "Acoustic emission monitoring of CFRP laminated composites subjected to multi-axial cyclic loading." *University of Iceland Reykjavik*, PhD Dessertation.

Valentin, D., Bonniau, P., and Bunsell, A. R. (1983). "Failure mechanism discrimination in carbon fibre-reinforced epoxy composites." *Composites*, 14(4), 345–351.

Vallen, D. I. H. (2002). "AE testing fundamentals, equipment, applications." *NDT.net*, Retreived from https://www.ndt.net.

Yang, B. L., Zhuang, X. M., Zhang, T. H., and Yan, X. (2009). "Damage mode identification for the clustering analysis of AE signals in thermoplastic composites." *Journal of Nondestructive Evaluation*, 28(3–4), 163–168.

Yoon, D.-J., Weiss, W. J., and Shah, S. P. (2000). "Assessing damage in corroded reinforced concrete using acoustic emission." *Journal of Engineering Mechanics*, 126(3), 273-283.

Yu, J., Ziehl, P., Caicedo, J., and Matta, F. (2013). "Acoustic Emission Monitoring and Fatigue Prediction of Steel Bridge Components." *Nondestructive Characterization for Composite Materials, Aerospace Engineering, Civil Infrastructure, and Homeland Security*, 8694, 1–10.

Yu, J., Ziehl, P., Zrate, B., and Caicedo, J. (2011). "Prediction of fatigue crack growth in steel bridge components using acoustic emission." *Journal of Constructional Steel Research*, 67(8), 1254–1260.

Yun, H. Do, Choi, W. C., and Seo, S. Y. (2010). "Acoustic emission activities and damage evaluation of reinforced concrete beams strengthened with CFRP sheets." *NDT and*

E International, 43(7), 615–628.

Yuyama, S., Yokoyama, K., Niitani, K., Ohtsu, M., and Uomoto, T. (2007). "Detection and evaluation of failures in high-strength tendon of prestressed concrete bridges by acoustic emission." *Construction and Building Materials*, 21(3), 491–500.

Ziehl, P. H. (2000). "Development of a damage based design criterion for fiber reinforced vessels." *The University of Texas at Austin, PhD Dessertation.*

APPENDIX A

RESULTS OF OTHER FRP SAMPLES USING AE TECHNIQUE

A.1 Introduction

This appendix includes the plots of the other CFRP and GFRP rebar samples that were tested under tensile loading and analyzed in chapter 4. Then, signals classification is briefly presented according to JCMS-III B5706 code. After that, AE features for FRP Rebars are presented in tables.

A.2 Time Domain Analysis

Conventional signal analyses were done in time domain. In the plots caption, the first letter stands for the type of fiber C for carbon and G for glass, the number that is followed stands for the size of the bar, the letter that is followed stands for sample, and the number that is followed stands for the number of the sample.

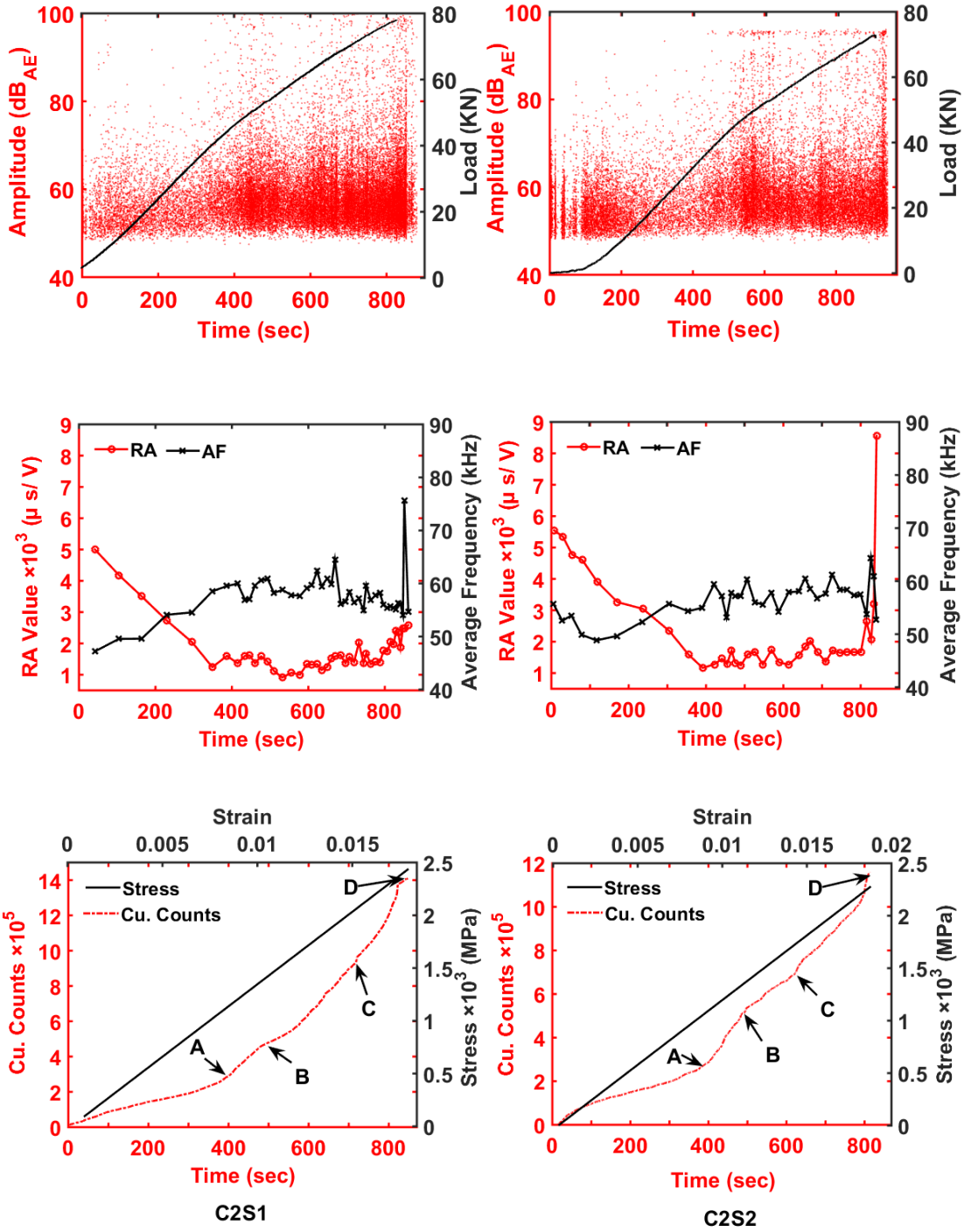

Figure A.1 Amplitude vs. time with load time superimposed, variation of AF and RA values and cumulative counts vs. time with stress-strain superimposed for CFRP size 2

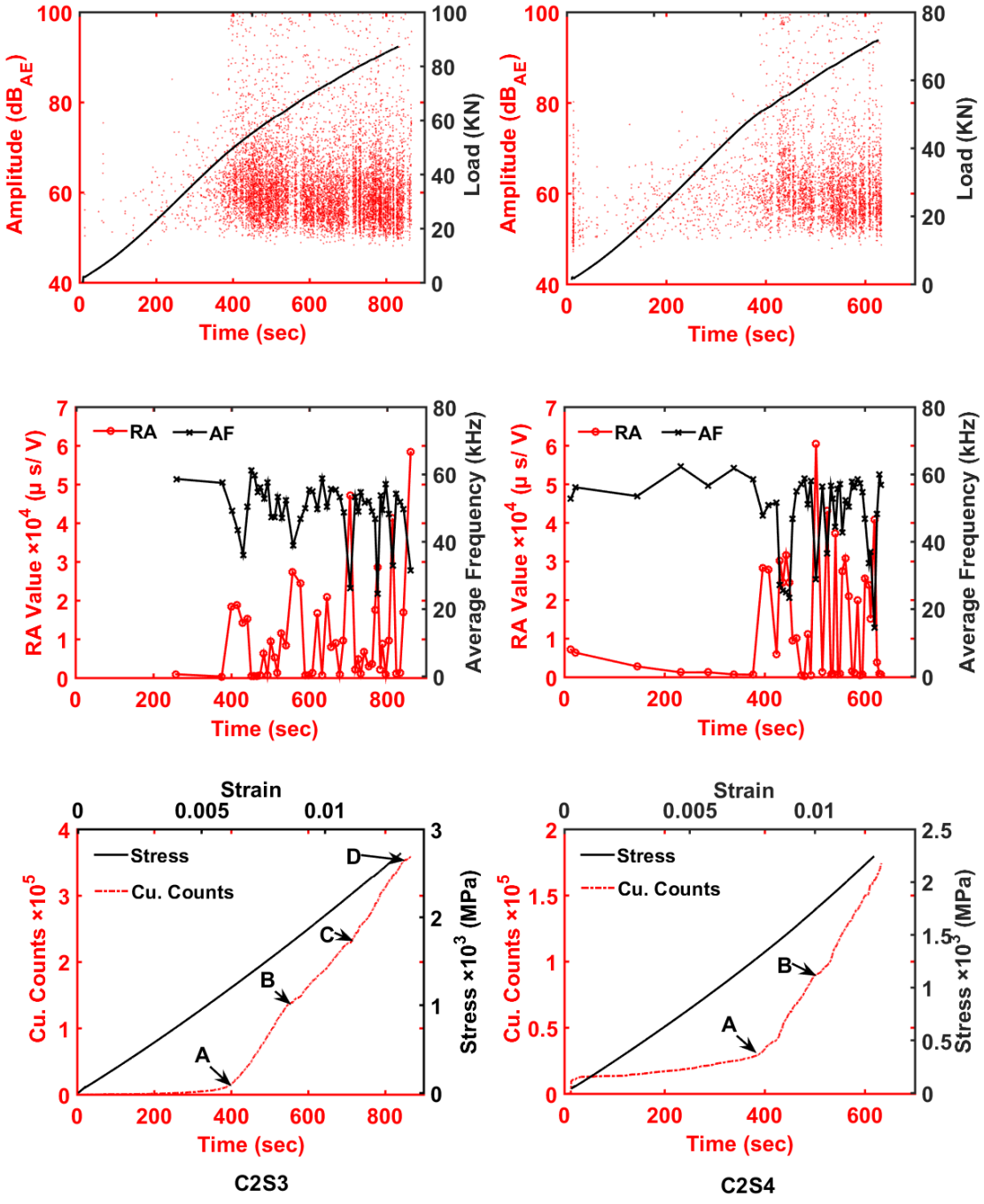

Figure A.2 Amplitude vs. time with load time superimposed, variation of AF and RA values and cumulative counts vs. time with stress-strain superimposed for CFRP size 2. C2S4 was loaded up to 92% predicted ultimate load

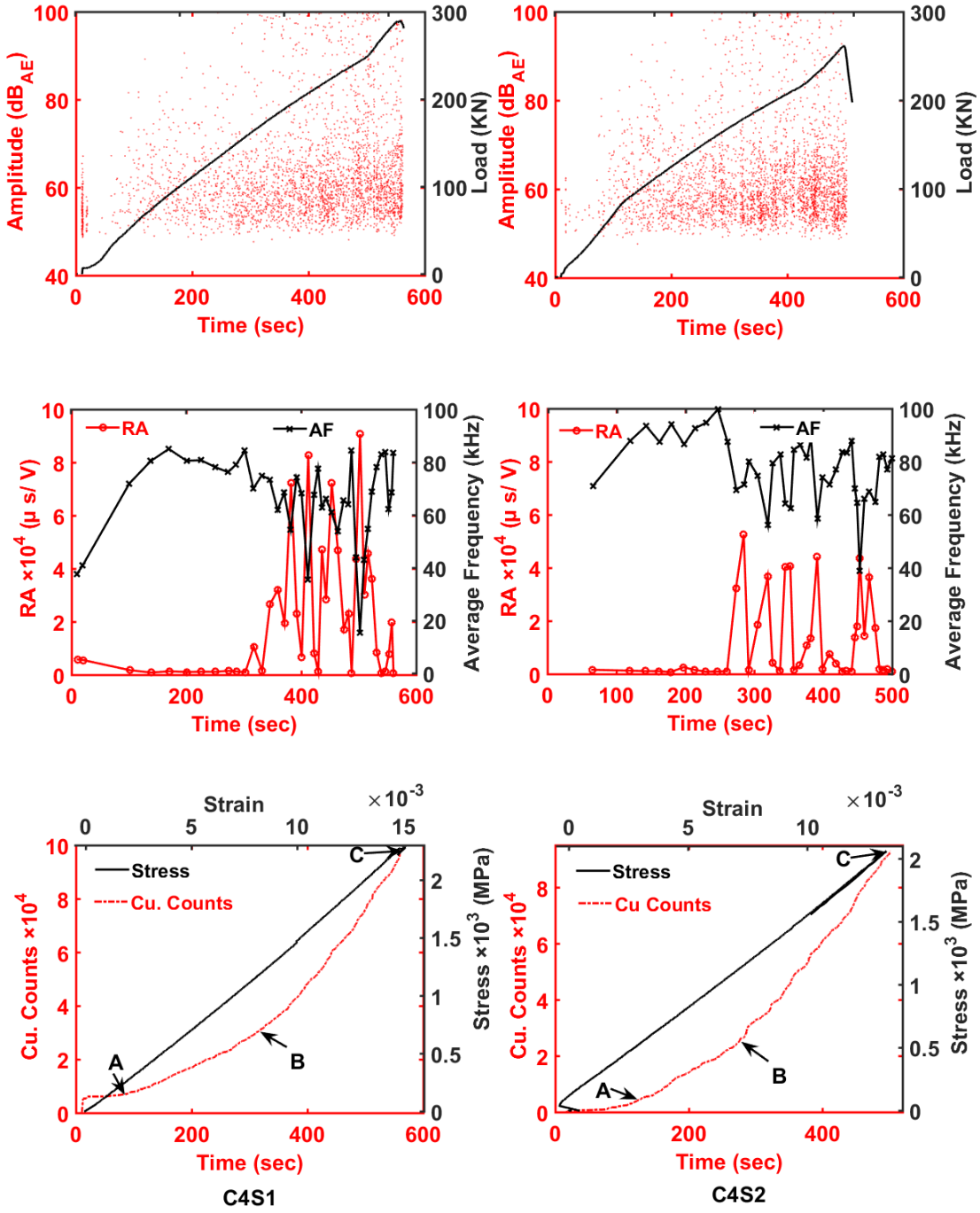

Figure A.3 Amplitude vs. time with load time superimposed, variation of AF and RA values and cumulative counts vs. time with stress-strain superimposed for CFRP size 4. C4S2 was loaded up to 90% predicted ultimate load

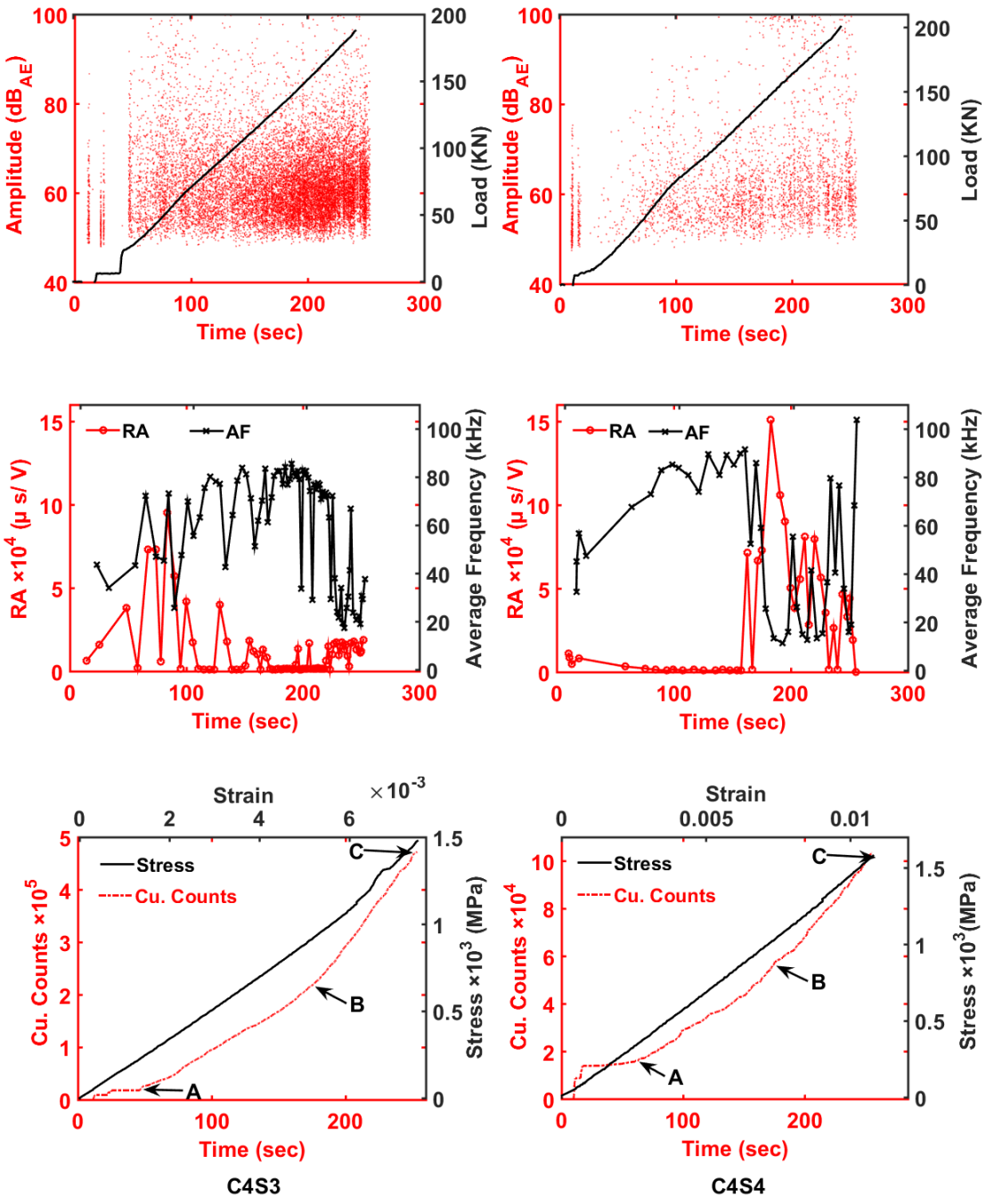

Figure A.4 Amplitude vs. time with load time superimposed, variation of AF and RA values and cumulative counts vs. time with stress-strain superimposed for CFRP size 4. C4S3 and C4S4 were loaded up to 70% and 74% predicted ultimate load respectively

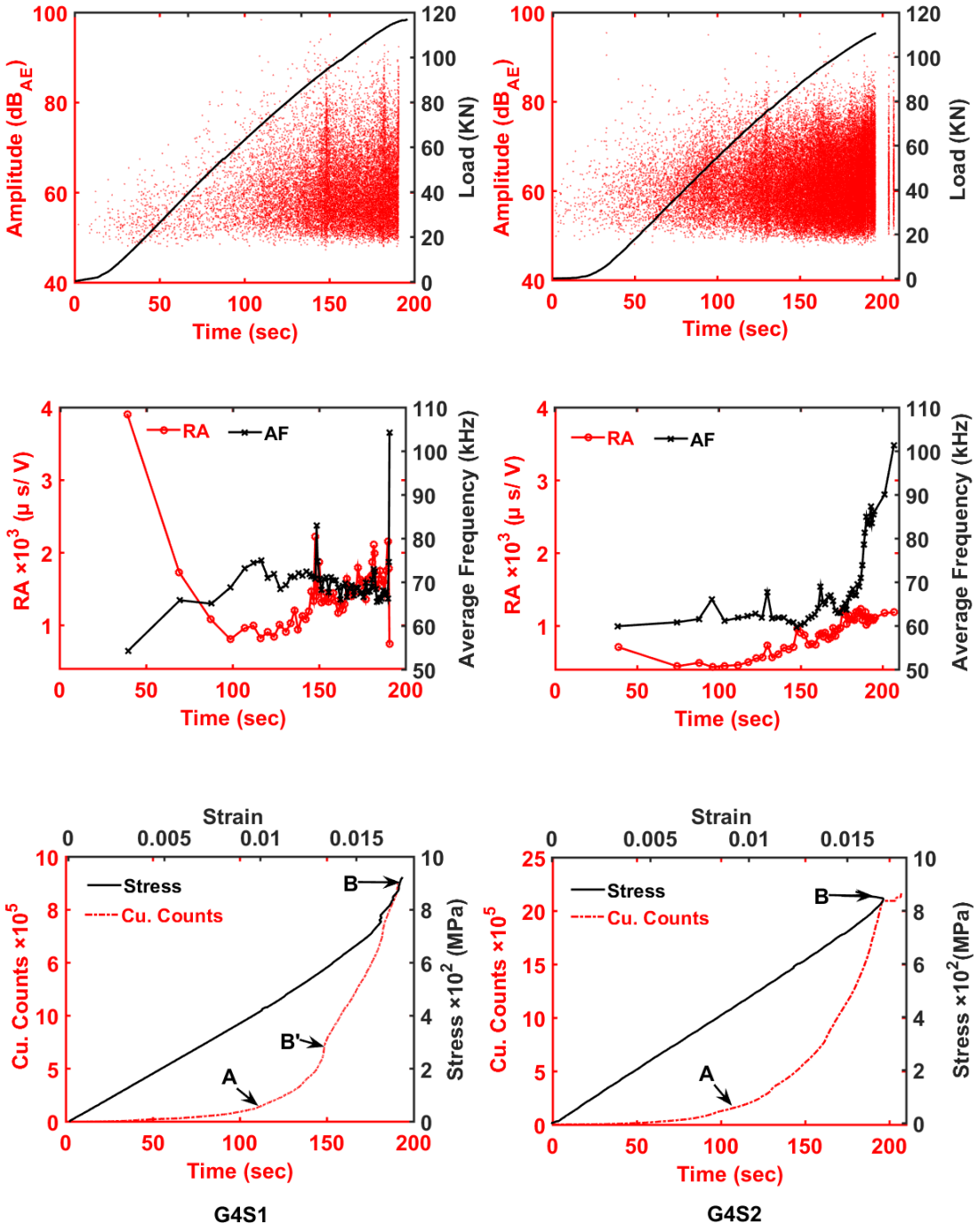

Figure A. 5 Amplitude vs. time with load time superimposed, variation of AF and RA values and cumulative counts vs. time with stress-strain superimposed for GFRP size 4

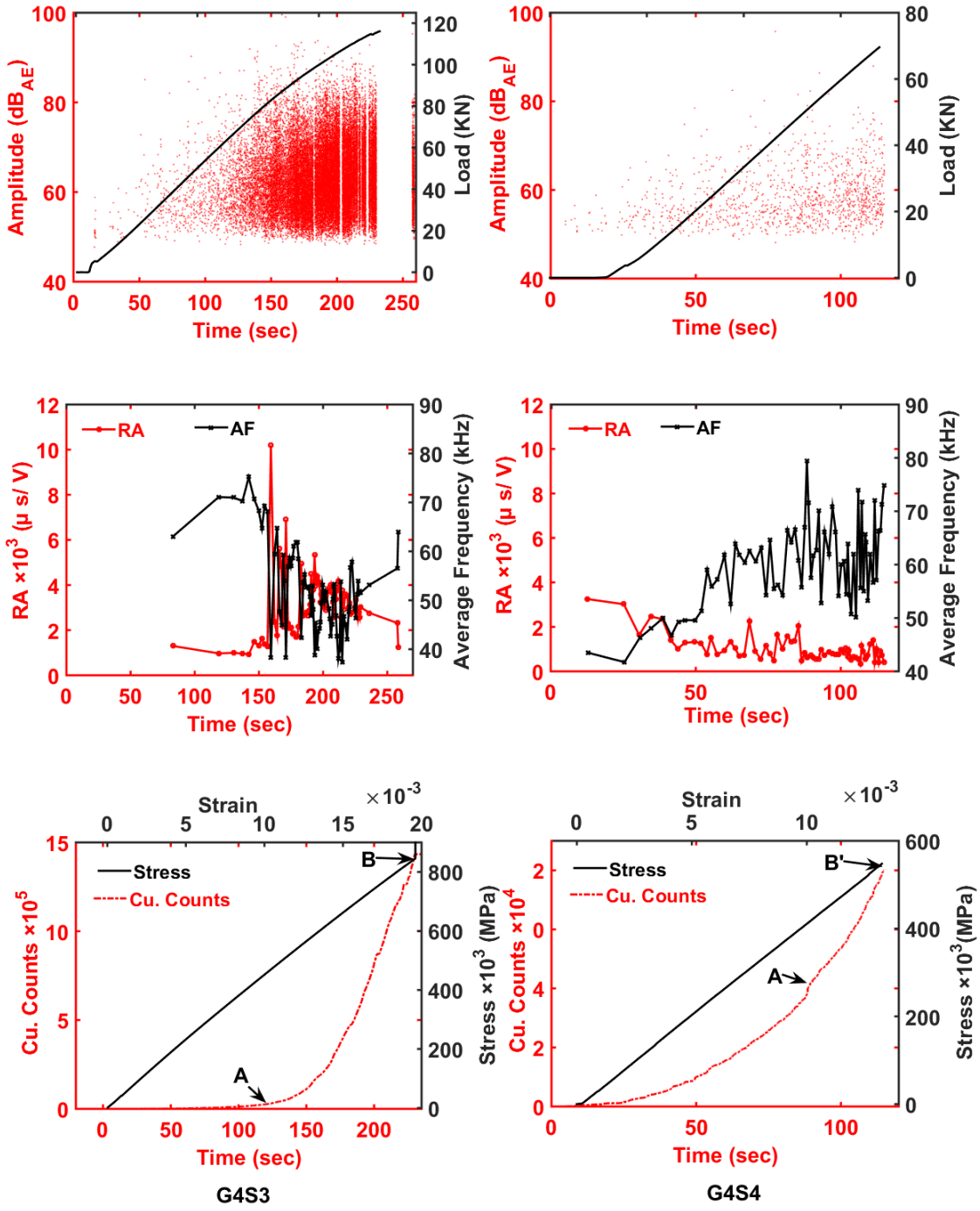

Figure A. 6 Amplitude vs. time with load time superimposed, variation of AF and RA values and cumulative counts vs. time with stress-strain superimposed for GFRP size4. G4S4 was loaded up to 70% predicted ultimate load

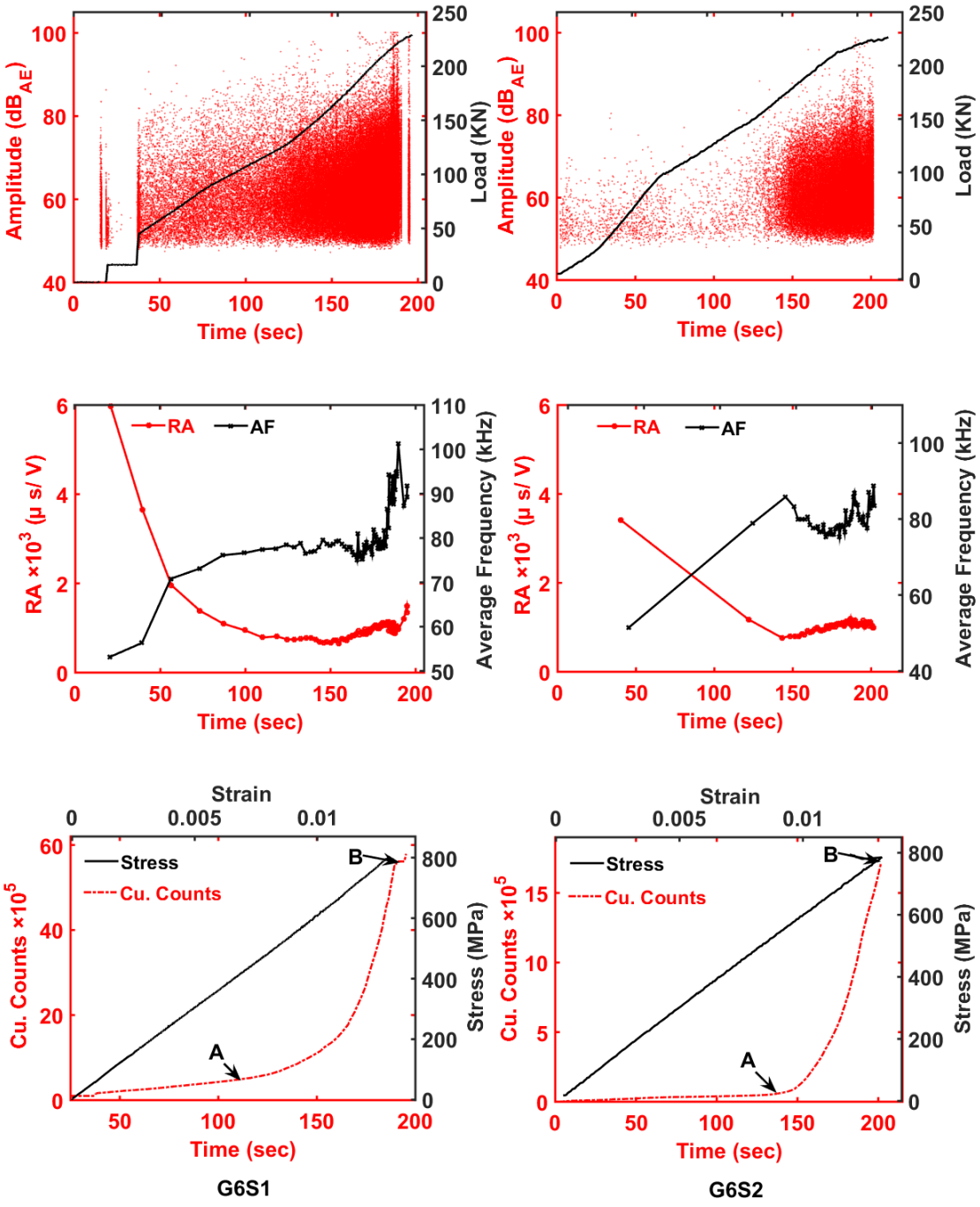

Figure A. 7 Amplitude vs. time with load time superimposed, variation of AF and RA values and cumulative counts vs. time with stress-strain superimposed for GFRP size 6

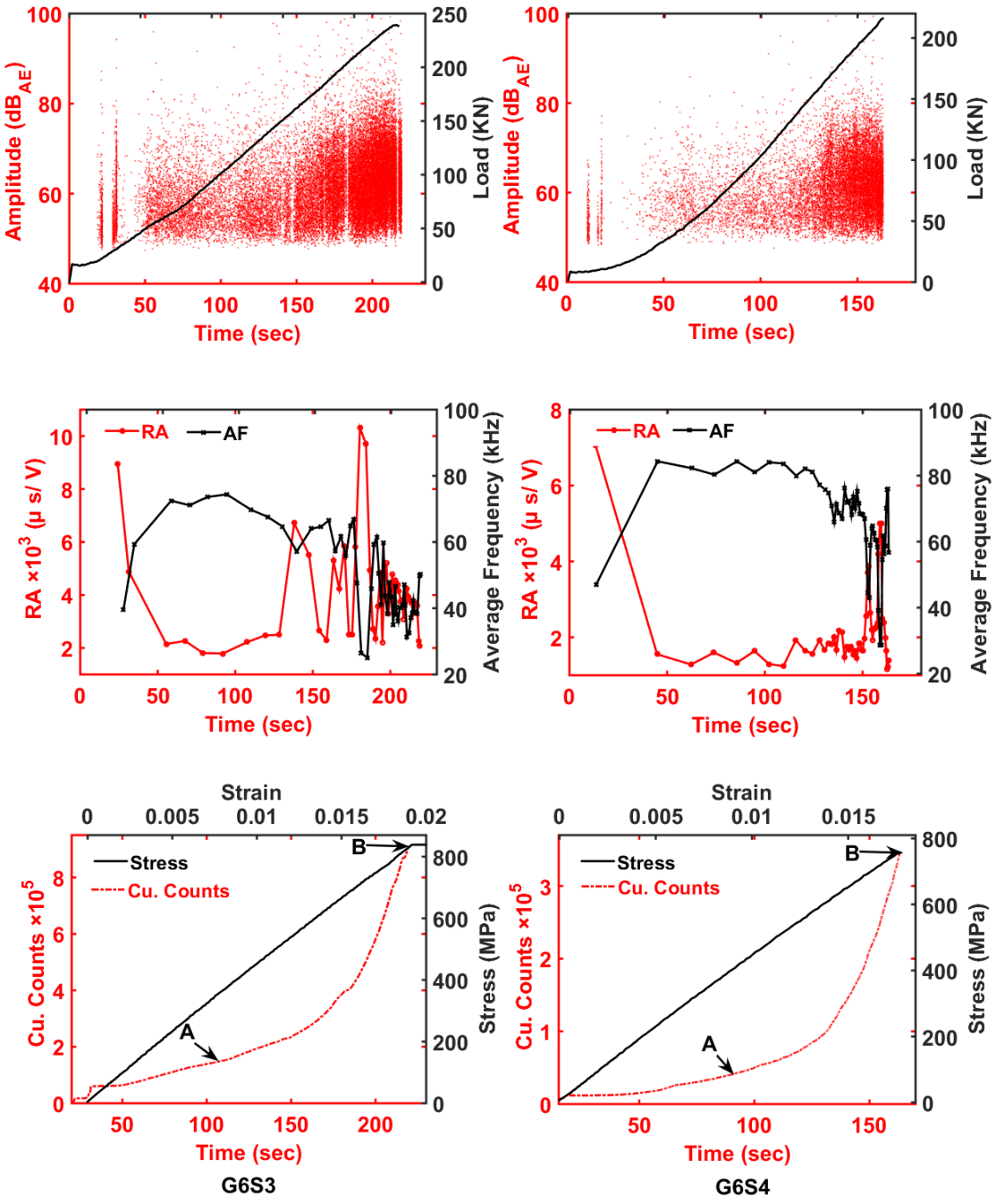

Figure A. 8 Amplitude vs. time with load time superimposed, variation of AF and RA values and cumulative counts vs. time with stress-strain superimposed for GFRP size 6. G6S4 was loaded up to 92% predicted ultimate load

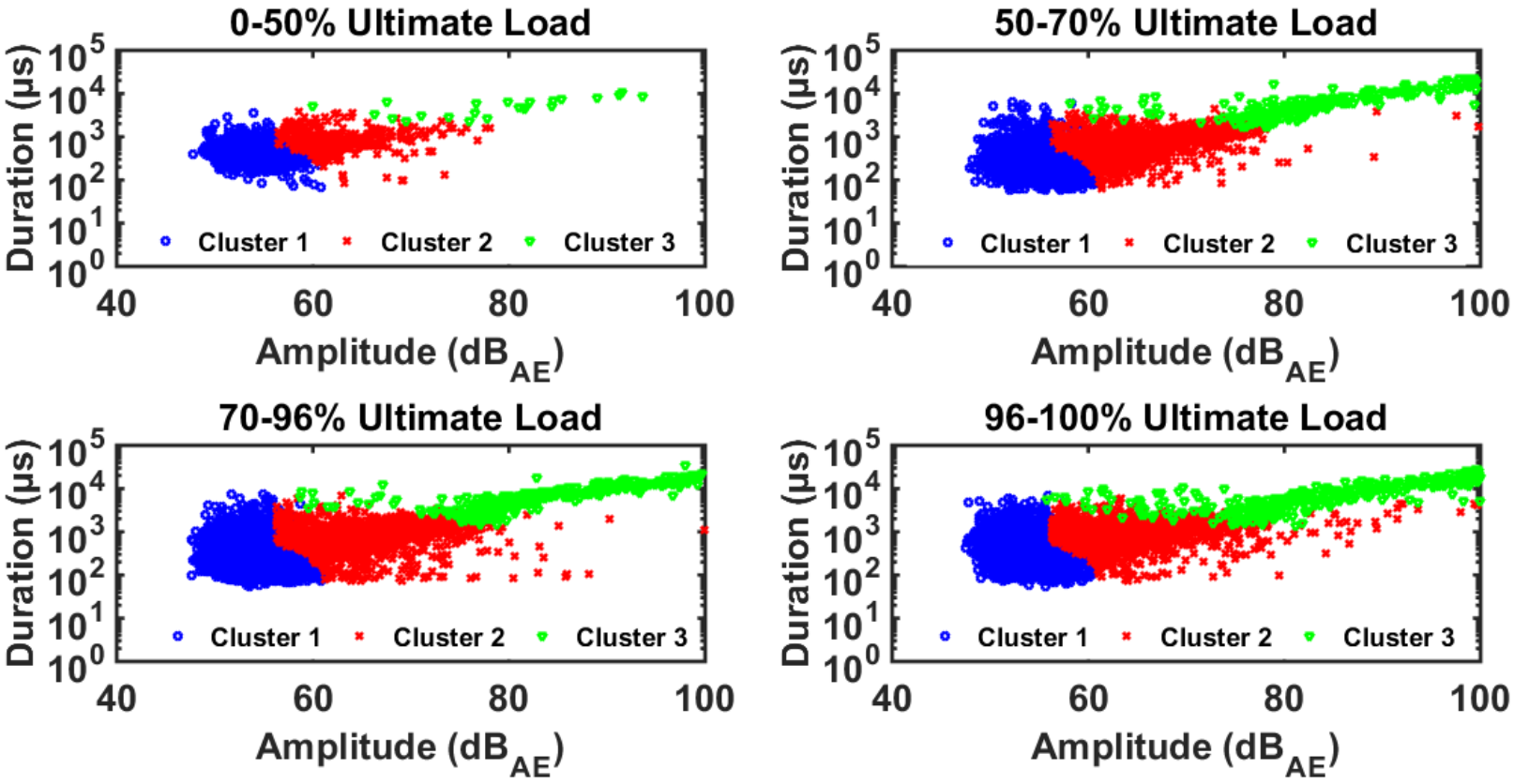

Figure A.9 Duration vs. Amplitude for four stages in CFRP size 2 specimen. Cluster 1: matrix cracking; cluster 2: deboning; cluster 3: fiber breakage

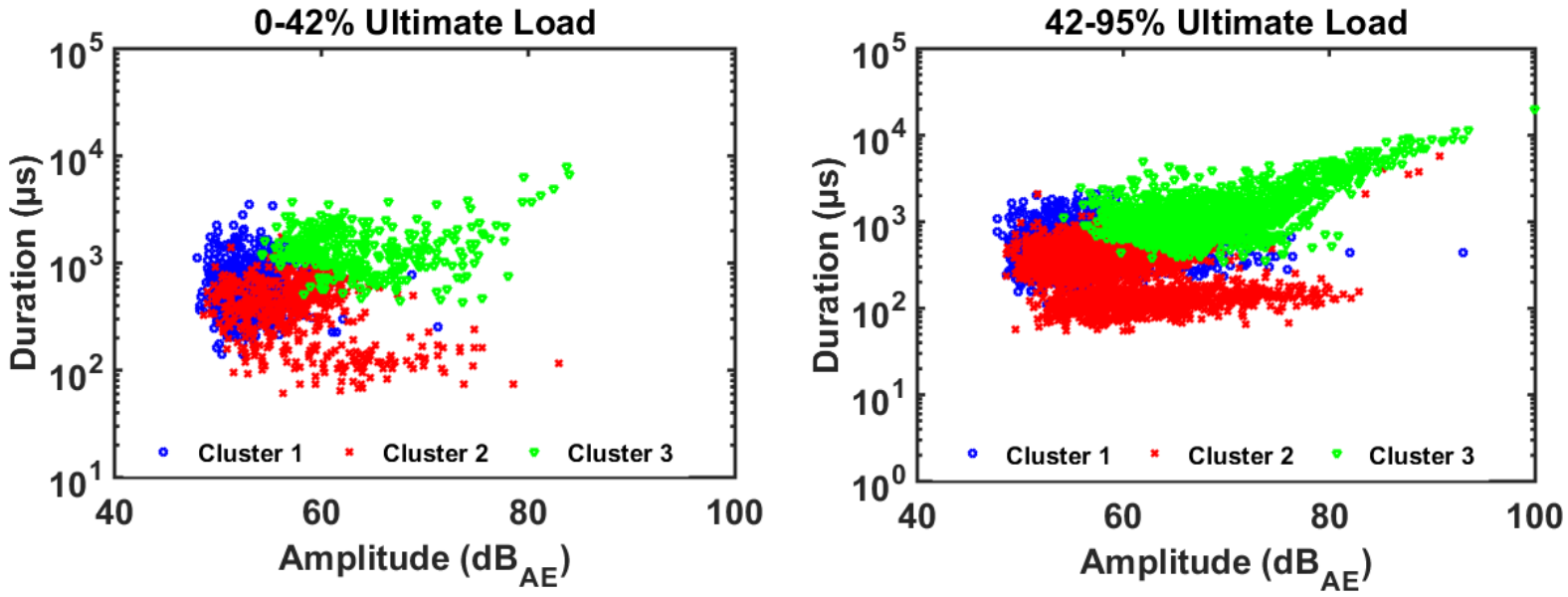

Figure A. 10 Duration vs. Amplitude for two stages in GFRP size 4 specimen. Cluster 1: matrix cracking; cluster 2: deboning; cluster 3: fiber breakage

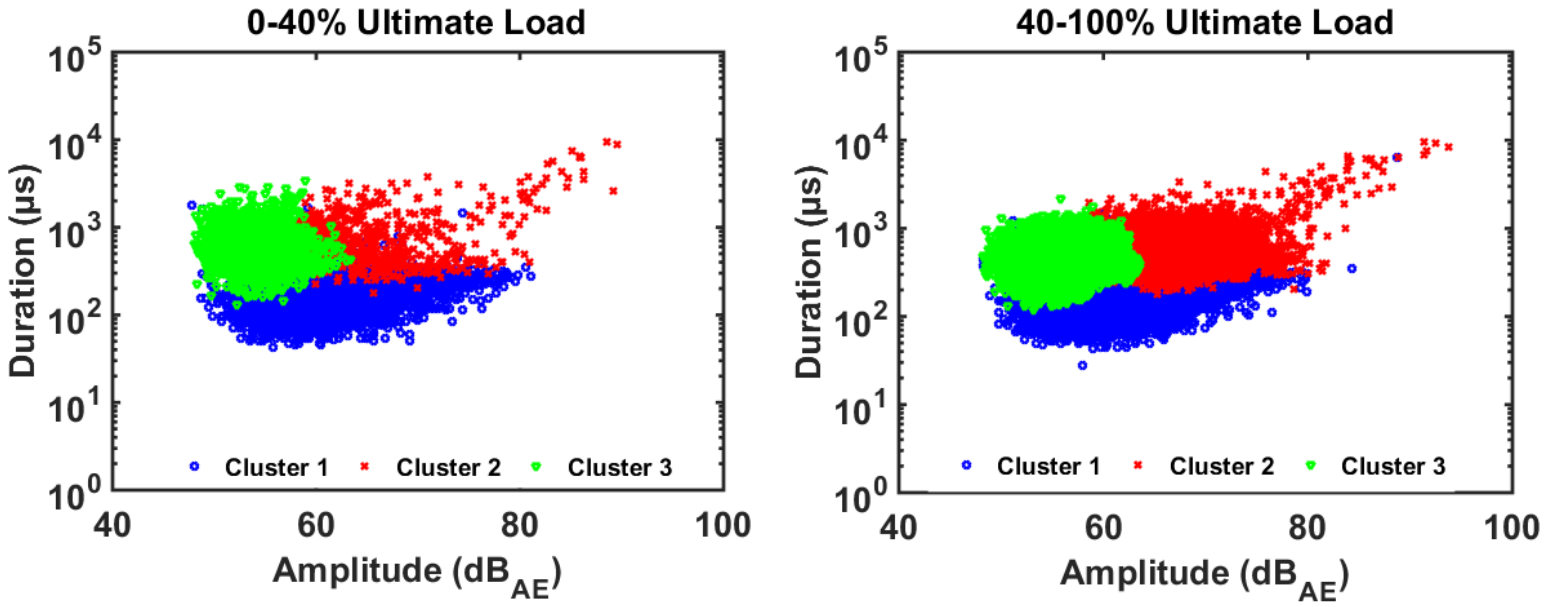

Figure A. 11 Duration vs. Amplitude for two stages in GFRP size 6 specimen. Cluster 1: deboning; cluster 2: matrix cracking; cluster 3: fiber breakage

A.3 Signal Classification

AE signals have been classified in JCMS-III B5706 code into two groups for concrete materials. As indicated in (Aggelis 2011; Ohno and Ohtsu 2010). This classification was concluded from the relationship between the RA vs. AF. Signals that have high RA and low AF values refer to the shear cracks, while the low RA and high AF values refer to the tensile cracks as shown in Figure A. 12 below. Figure A. 12 shows that signals due to tensile (longitudinal) stress appear on the left side of the diagonal in the RA vs. AF plot. The signals indicating damage due to shear stresses appear on the right side of the diagonal of the same plot.

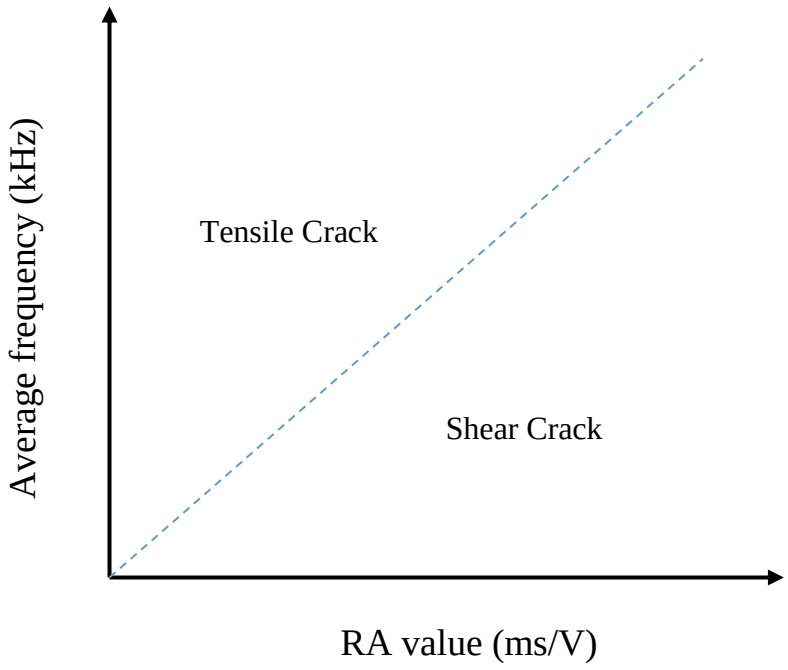

Figure A. 12 RA vs. AF values (reproduced from Ohno and Ohtsu 2010)

For this purpose, the RA vs. AF for CFRP and GFRP bars tested was plotted. As can be seen in Figure A.13, most signals lie to the left side of the diagonal, as that is the primary direction of stresses in these pultruded bars. There are some signals close to the diagonal indicating combination of longitudinal and transverse damage. Figure 4.7 shows SEM images of both CFRP and GFRP bars showing damage primarily in the longitudinal direction. Considering the SEM evidence in Figure 4.7, and the plots of RA vs. AF shown below, the theory presented in the JCMS-III B5706 code is applicable to FRP pultruded bars.

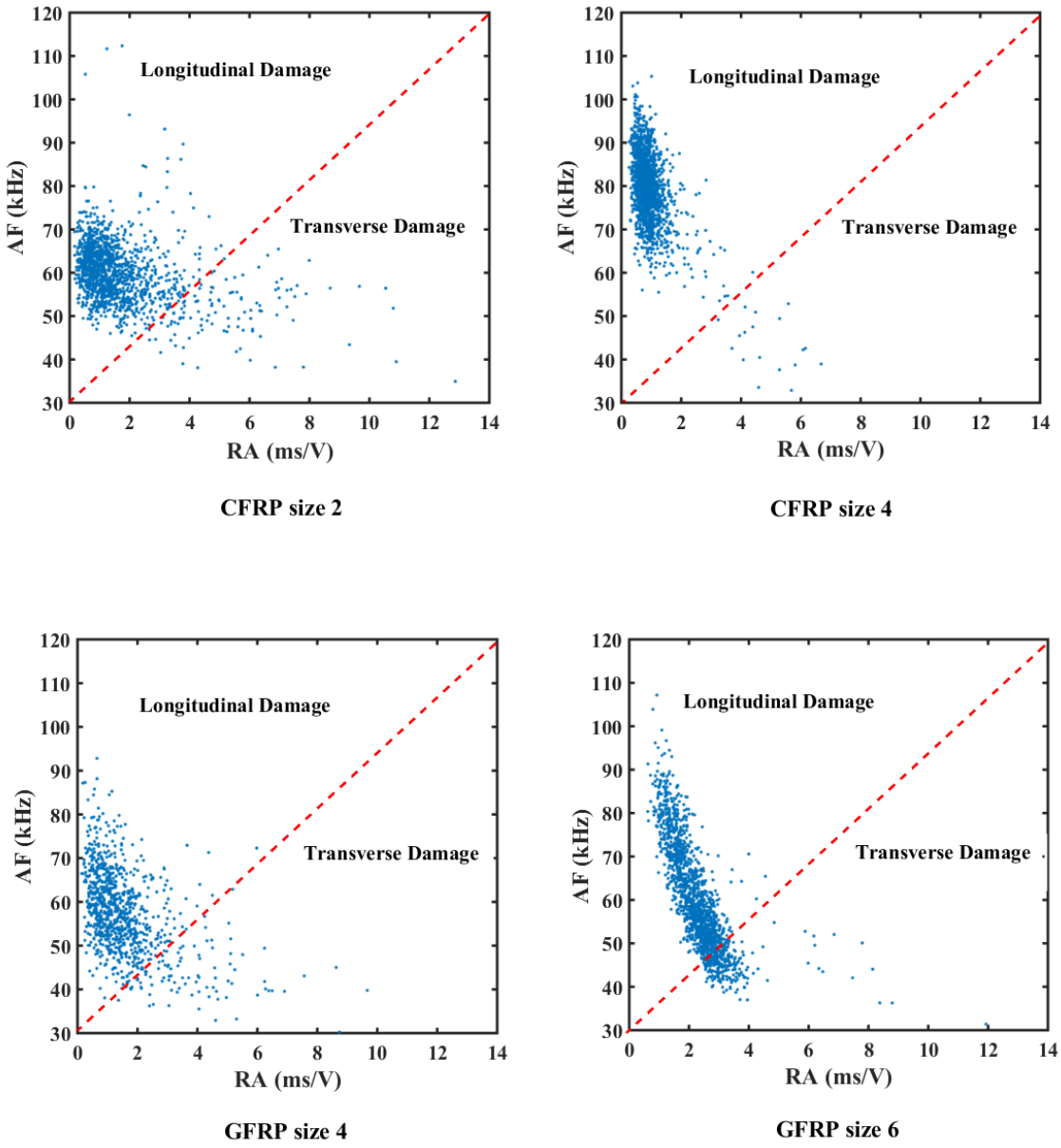

Figure A. 13 RA vs. AF values for CFRP and GFRP rebar samples

A.4 Time - Frequency Domain Analysis

STFT was performed on different AE signal amplitudes and the energy distribution was calculated and shown in Figure 4.6)in chapter 4. Figure A. 14 shows the STFT plot for those AE signals.

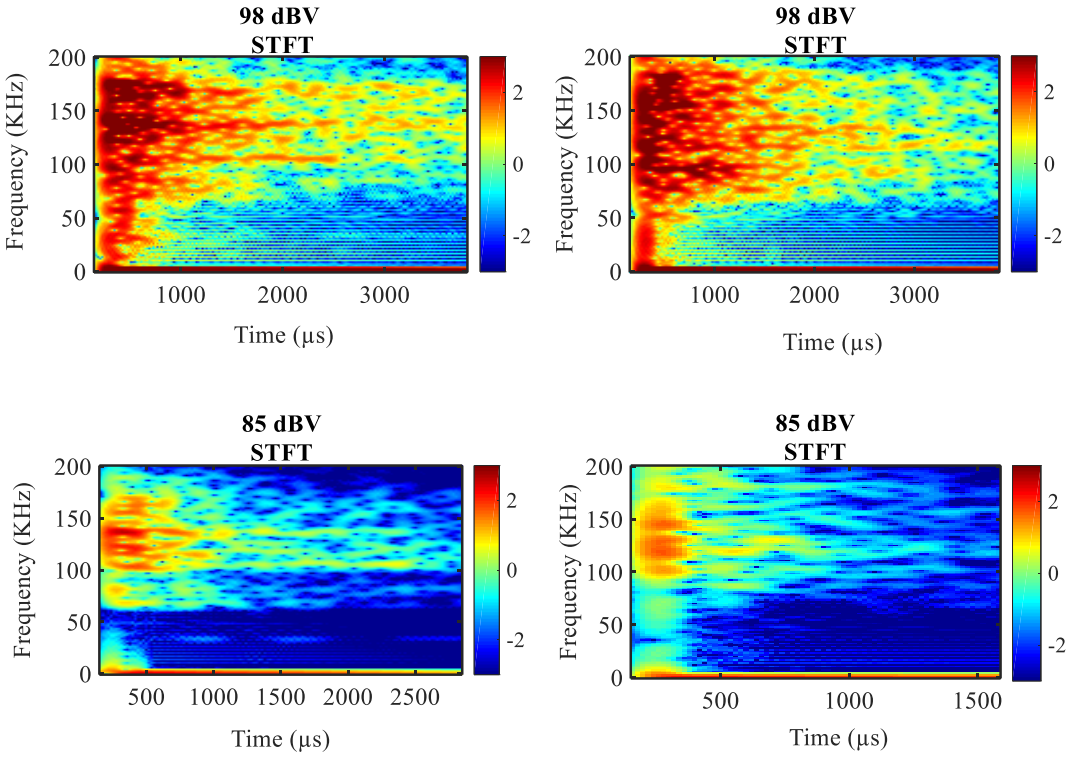

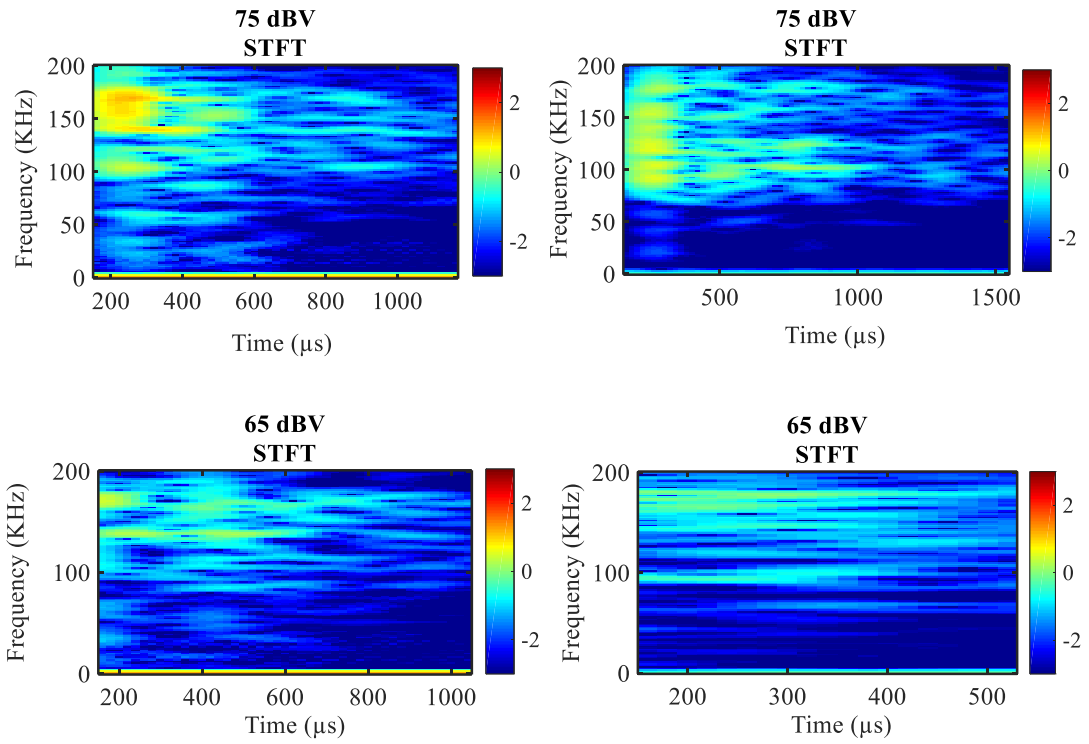

Figure A. 14 STFT for various signal amplitude for CFRP and GFRP bar specimens

A.5 AE Features for FRP Rebars

The number of AE signals within the various amplitude ranges were investigated in CFRP and GFRP specimens. Three stages were determined according to the change of the slope of the cumulative counts. The mean of AE features, such as duration, energy, number of counts, rise time, maximum frequency, average frequency, and RA for each range were calculated and presented in the following tables.

Table A.1 Mean values of AE features for CFRP bar specimen

(a) Stage I

Amplitude Range (dB_{AE})	# Events	Amplitude (dB_{AE})	Duration (µs)	Energy (Joule)	# of Counts / event	Rise Time (µs)	Max. Frequency (kHz)	Average frequency (kHz)	RA (µs/V)
95 – 100	0								
90 - 95	0								
85 - 90	1	88.93	7840.00	155.19	131	25.00	169	16.71	8.94
80 - 85	1	81.62	4310.00	18.43	173	20.00	169	40.14	16.59
75 - 80	5	77.24	2684.50	18.45	313	146.50	158	118.42	186.35
70 - 75	7	72.4	195.36	3.68	186	118.93	154	93.18	334.09
65 - 70	41	67.04	1293.96	1.13	105	93.48	150	86.09	420.20
< 65	598	55.77	684.67	0.12	33	118.31	147	49.18	2386.10

Table A.2 Mean values of AE features for CFRP bar specimen

(b) Stage II

Amplitude Range (dB_{AE})	# Events	Amplitude (dB_{AE})	Duration (µs)	Energy (Joule)	# of Counts / event	Rise Time (µs)	Max. Frequency (kHz)	Average frequency (kHz)	RA (µs/V)
95 – 100	35	98.05	15189.07	5082.78	267	135.00	149	16.41	16.19
90 - 95	20	92.42	11554.88	680.15	264	56.88	158	22.46	13.58
85 - 90	30	87.58	7434.50	188.42	178	94.92	155	25.13	36.68
80 - 85	54	82.49	5128.24	35.52	179	91.67	155	58.78	69.85
75 - 80	93	77.33	2809.97	8.54	233	122.47	159	93.01	184.53
70 - 75	187	72.13	1223.14	2.10	103	77.16	158	89.27	190.45
65 - 70	519	67.1	850.91	0.67	64	63.27	157	80.16	286.21
< 65	6953	57.25	425.08	0.09	23	72.20	155	58.61	1198.73

Table A.3 Mean values of AE features for CFRP bar specimen

(c) Stage III

Amplitude Range (dB_{AE})	# Events	Amplitude (dB_{AE})	Duration (µs)	Energy (Joule)	# of Counts	Rise Time (µs)	Max. Frequency (kHz)	Average frequency (kHz)	RA (µs/V)
95 – 100	114	97.9	16160.86	5281.66	360	193.83	151	21.38	23.97
90 - 95	85	92.26	11166.47	752.19	291	148.21	150	24.57	37.63
85 - 90	1	87.49	8039.73	211.16	251	127.80	152	34.80	55.72
80 - 85	159	82.23	5631.22	51.64	314	136.07	153	63.26	104.51
75 - 80	253	77.48	2765.95	10.32	252	131.87	154	97.50	183.82
70 - 75	482	72.3	1487.75	3.06	125	102.91	155	91.51	251.72
65 - 70	1144	67.14	1078.91	0.93	84	101.91	155	83.69	460.41
< 65		56.11	500.46	0.10	26	113.83	155	57.14	2136.55

Table A.4 Mean values of AE features for GFRP bar specimen

(a) Stage I

Amplitude Range (dB_{AE})	# Events	Amplitude (dB_{AE})	Duration (µs)	Energy (Joule)	# of Counts / event	Rise Time (µs)	Max. Frequency (kHz)	Average frequency (kHz)	RA (µs/V)
95 – 100	0								
90 - 95	0								
85 - 90	0								
80 - 85	1	82.46	4872.50	44.17	148	125.00	100	30.37	94.19
75 - 80	2	75.36	665.00	7.67	83	168.75	155	130.72	294.34
70 - 75	14	72.14	1189.82	3.78	120	146.43	124	115.29	375.90
65 - 70	24	67.49	1263.75	1.36	103	101.15	119	91.76	441.39
< 65	727	54.68	851.16	0.14	36	197.73	117	43.80	4120.12

Table A.5 Mean values of AE features for CFRP bar specimen

(a) Stage II

Amplitude Range (dB_{AE})	# Events	Amplitude (dB_{AE})	Duration (µs)	Energy (Joule)	# of Counts / event	Rise Time (µs)	Max. Frequency (kHz)	Average frequency (kHz)	RA (µs/V)
95 – 100	0								
90 - 95	0								
85 - 90	0								
80 - 85	5	82.43	4524.00	48.37	187	23.50	128	55.35	16.42
75 - 80	12	77.17	2098.33	7.94	163	47.29	153	93.11	67.41
70 - 75	34	72.63	1026.47	2.26	87	75.66	143	94.78	195.97
65 - 70	56	67.37	784.42	0.75	60	48.53	135	84.64	202.29
< 65	701	56.61	577.64	0.11	26	91.08	125	49.14	1683.78

Table A.6 Mean values of AE features for CFRP bar specimen

(b) stage III

Amplitude Range (dB_{AE})	# Events	Amplitude (dB_{AE})	Duration (µs)	Energy (Joule)	# of Counts / event	Rise Time (µs)	Max. Frequency (kHz)	Average frequency (kHz)	RA (µs/V)
95 – 100	1	99.91	20247.50	9726.53	244	222.50	153	12.05	22.47
90 - 95	8	92.06	7917.81	376.02	104	79.68	148	15.39	19.10
85 - 90	26	87.18	6514.52	87.56	124	50.77	145	18.65	24.70
80 - 85	71	81.99	3659.30	15.91	182	84.75	145	56.89	67.69
75 - 80	186	77.02	1644.80	3.99	133	94.77	150	95.00	138.81
70 - 75	427	72.2	1005.32	1.50	77	75.56	147	86.03	192.04
65 - 70	976	67.11	798.87	0.56	56	75.41	147	77.51	332.77
< 65	6343	57.4	522.64	0.11	25	98.15	139	52.98	1597.22

APPENDIX B

μCT AND SEM CROSS AND LONGITUDINAL SECTIONS SHOWING THE GROWTH OF VOIDS AND THE POSSIBLE DIFFERENT DAMAGE MECHANISMS

B.1 Introduction

This appendix includes some images for CFRP and GFRP rebar samples using μCT and SEM observations that were analyzed in chapter 5. The affect of increasing the trapped voids during the pultrusion process was briefly stated using two CFRP size 4 rebar samples that have different percentages of void volume. Next, cross and longitudinal sections of untested and tested GFRP size 4 were included showing the different possible damage mechanisms in the sample before failure.

B.2 Voids Effects

Two 5 cm pieces were taken from untested CFRP size 4 rebar samples and investigated using μCT scan to determine the percentage of the voids. The two rebars were tested under tension until failure, and then another 5 cm pieces were taken from the center of the tested samples for further μCT scan. The percentage of the voids volume was calculated for 2000 slices (1.8 mm) from the samples. Table B.1 shows that the sample that has higher percentage of the void volume at the untested stage failed at an ultimate load less than the

sample that has lower percentage of the void volume at the untested stage. The longitudinal sections of these samples are shown in Figure B.1.

Table B.1 Void volume percentage and their affection on the ultimate load for CFRP sample rebars

	% Void Volume		
	Untested Sample	**Tested Sample**	**Ultimate Load kN**
CFRP Size 4 Sample #1	1.09	2.45	290
CFRP Size 4 Sample #2	1.59	2.99	245

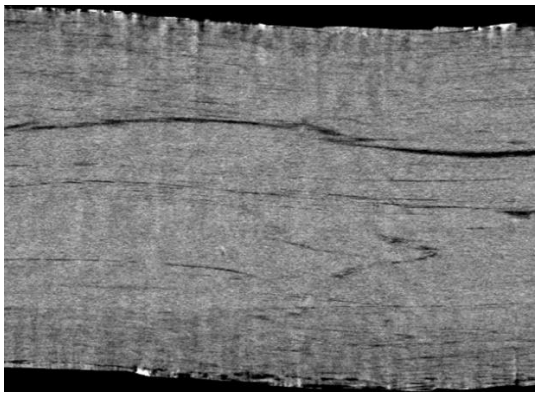

CFRP size 4 sample #1 at failure

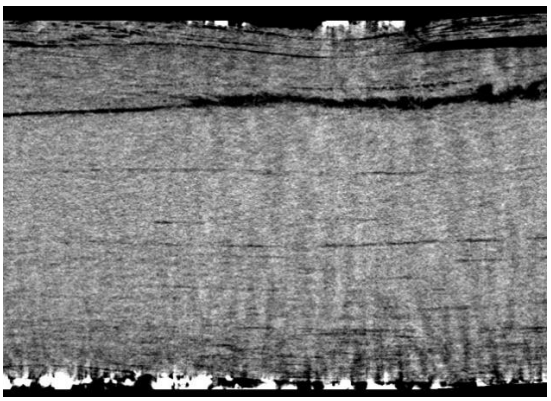

CFRP size 4 sample #2 at failure

Figure B.1 Longitudinal sections for the two CFRP size 4 tested samples

B.3 SEM Observation

Microscopic inspection of polished and cleaned GFRP samples were performed in both cross and longitudinal sections. Figure B.2 shows the untested GFRP sample was very porous. The area of voids was calculated using both µCT and SEM analyses and shown in Table 5.3 in chapter 5.

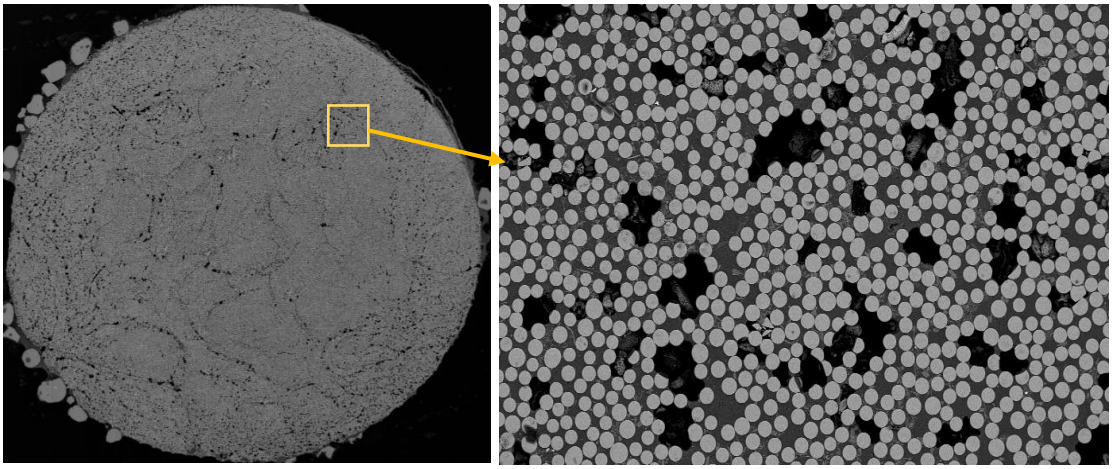

Cross section for the whole sample Zoom in of a small area

Figure B.2 Cross sections of an untested GFRP size 4 sample

Figure B.3 shows a cross section of a tested GFRP size 4 sample up to 95% of the predicted ultimate load. It can be noticed from the figure that the matrix cracking occurred at the edge of a void, and also the two primary voids were enlarged and linked together as the load increased.

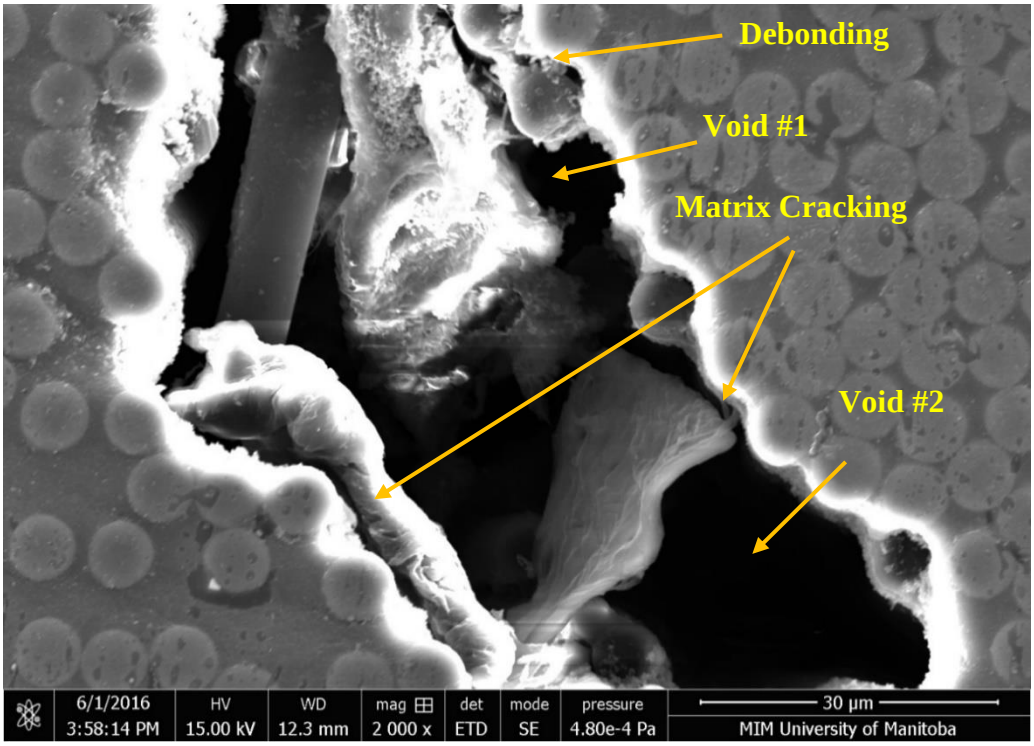

Figure B.3 Cross section of a tested GFRP size 4 sample up to 95% of the predicted ultimate load

Figure B.4 shows a longitudinal section of the same tested GFRP size 4 sample up to 95% of the predicted ultimate load. The figure shows the fiber fracture.

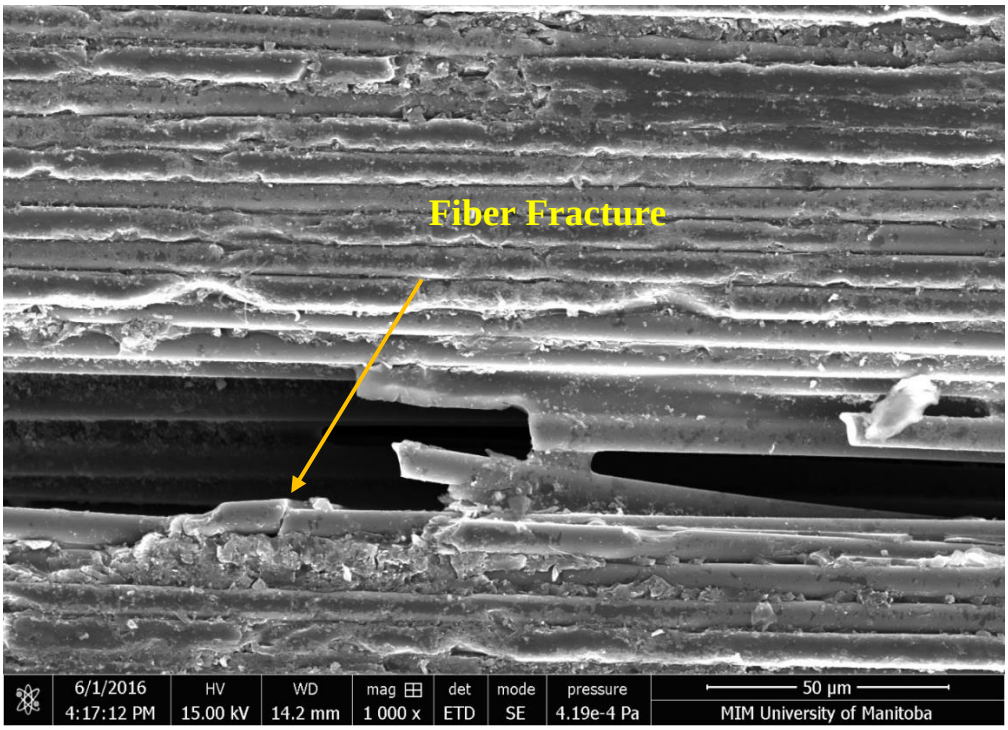

Figure B.4 Longitudinal section of a tested GFRP size 4 sample up to 95% of the predicted ultimate load showing the fiber fracture

Figure B.5 shows another longitudinal section of the same tested GFRP size 4 sample up to 95% of the predicted ultimate load. The figure shows clearly the fiber pullout after fracturing.

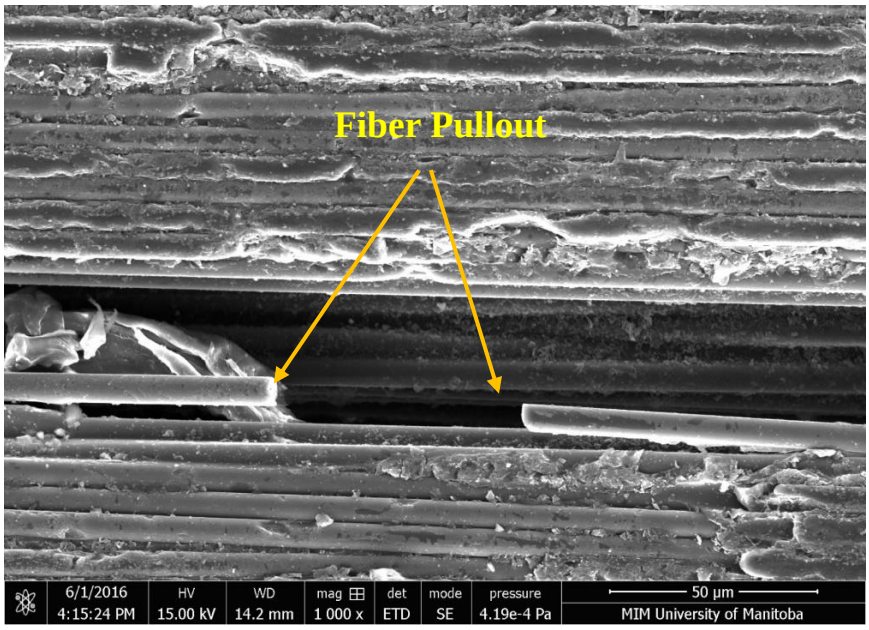

Figure B.5 Longitudinal section of a tested GFRP size 4 sample up to 95% of the predicted ultimate load showing the fiber pullout